Development of a Spatially Incoherent Laser Source

Entwicklung einer räumlich inkohärenten Laserquelle

Wissenschaftliche Arbeit zur Erlangung des Grades
M. Sc. im Studiengang Physik der kondensierten Materie
an der Fakultät für Physik der Technischen Universität München.

Betreut von	Prof. Dr. Michael Knap Prof. Dr. Immanuel Bloch Dr. Christian Groß
Eingereicht von	David Wei
Eingereicht am	13. Februar 2019

Abstract

Projected optical dipole potentials for ultracold atoms suffer from coherent speckle noise, significantly degrading the potential shaping quality. In this thesis, the generation of incoherent light and its use to suppress coherent artefacts in the light field is demonstrated. Passing a coherent laser beam through a rotating optical diffuser or modulating the angular beam incidence onto the diffuser using an acousto-optic deflector are both shown to produce quasi-monochromatic light fields with controllably reduced spatial coherence. An alternative approach involves conversion of temporal to spatial incoherence, where modal dispersion in a square-core multimode optical step-index fibre efficiently induces dephasing. This results in temporally fast decorrelating, spatially incoherent, flat-top light complying with the requirements of off-resonant dipole traps with high trap frequencies. To characterize the light source, a lateral shifting Michelson interferometer has been constructed in order to measure the spatiotemporal coherence function. Finally, femtosecond lasers have been identified as a suitable spectrally broad light source with low temporal intensity noise.

Contents

1 Introduction

Strongly interacting quantum many-body systems arise in a variety of fields, including condensed-matter physics, quantum chemistry and high-energy physics [1]. Their understanding is hindered by the complexity that grows exponentially with system size, rendering their full description classically intractable. Quantum simulators pose a solution by mapping the original many-body problem onto an equivalent problem implemented in another well-controlled quantum system [2].

Beginning with the first realization of a Bose-Einstein condensate [3, 4], ultracold atoms have developed into an excellent simulation platform with optically tunable trapping geometries [5, 6]. Artificial crystals have been realized using optical lattices, leading to the observation of the superfluid-to-Mott insulating phase transition [7] as the first simulated strongly correlated system. These systems have since allowed the study of i.a. non-equilibrium dynamics [8] or topological matter [9]. Tunable contact interactions have been added using Feshbach resonances [10], and long-range interactions are also studied [11, 12].

The development of quantum-gas microscopes for both bosons [13, 14] and fermions [15, 16, 17, 18] has enabled single-atom resolved fluorescence imaging, providing the detection of local observables required for correlation studies. Subsequently, the implementation of spatial light modulators has permitted arbitrary initial state engineering [19], allowing the observation of spin dynamics [20, 21] and thermalization experiments [22, 23].

Optical tweezers constitute an alternative simulation tool [24], where atomic positions can be arbitrarily arranged, providing flexibility in trap geometry [25], but the atoms themselves are fixed in place. Both flexible trap arrangement and atomic tunneling can be in principle retained by projecting arbitrary potentials using the spatial light modulator in a quantum-gas microscope.

Coherent Disorder in Projected Potentials

However, due to the coherent nature of the commonly used light sources, wavefront distortions, e.g. induced by scatterers in the optical path, can lead to undesired random

interference artefacts ("speckle" [26]), significantly degrading the projected image and altering the physics to be studied [27]. Particularly, note that such static speckle patterns have been used to study localization of cold atoms [28]. While in interference pattern [29] or Fourier mask [13] generated potentials coherence is an intrinsic requirement, the use of spatially incoherent light sources for real-space imaging is expected to greatly enhance performance [30].

Note that since speckle noise is a very universal wave phenomenon, emergent from wavelength-sized scatterers, it is present in a variety of fields, not only in optical full-field imaging (e.g. laser projection [31], holography [32], optical coherence tomography [33]) but also, most notably, in ultrasound imaging [34] and synthetic-aperture radar imaging [35].

Incoherent Light Generation

The use of coherent lasers in imaging is mainly justified by the high light intensities achievable. With this requirement, multiple approaches to generating light with reduced coherence properties have been developed.

Direct Spatial Coherence Reduction

One approach for speckle reduction, where the use of a chosen coherent light source can be continued, involves actively reducing the spatial coherence [36]. For this, a spatially dependent phase changing, transmitting optical element is used to control the wavefront. This purposefully introduces coherent noise in a diffraction plane, but temporally modulating the wavefront allows averaging of different realizations of speckle fields, resulting in spatial coherence reduction.

The modulation can be realized by mechanically moving (e.g. rotating [37], vibrating [38] or shifting [39]) a bulk optical diffuser (with random or engineered [40] diffractive surface structure), where the rotating random diffuser approach is tested in sec. 3.4 and has found commercial use in laser projectors [41]. Another possibility is to modulate the incidence angle on a diffuser, where the angle can be introduced by e.g. piezoelectrically actuated mirrors [42] or acousto-optic deflectors (AODs) (sec. 3.5).

Speckle also arises when coherent light passes through multimode optical fibres [43], where the particular realization of the pattern is determined by the fibre mode structure. Mechanically vibrating the fibre [44] or modulating the fibre coupling [45] thus gives rise to speckle averaging.

Temporal Incoherence Conversion

Alternatively, one can use the temporal incoherence of spectrally broad light sources to reduce spatial coherence, which is accomplished by inducing spatially varying propagation delays onto the initial light beam. When the differential delays are larger than the coherence times, they mutually dephase and become incoherent.

The time delays can be realized using bulk optics, e.g. echelons [46] or tilted etalons with a transmissivity gradient [30]. An alternative to such thick structures are optical fibres, where distinct propagation modes travel with different speeds. For this, e.g. a multi-core fibre where the cores have varying lengths [47] or multimode fibres with a single large core [48] (ch. 4) can be used. Similarly, amplified spontaneous emission (ASE) fibre amplifiers with large cores have been shown to produce light with reduced spatial coherence [49].

Low Spatial Coherence Light Sources

Finally, lasers with complex cavities and feedback mechanisms can be built, which intrinsically have low spatial coherence [50].

One approach uses vertical-cavity surface-emitting laser (VCSEL) arrays combining multiple independently lasing (i.e. mutually incoherent) coherent light sources in one light field [51]. Spatial multimode output also results from highly transversally multimode cavities, realized e.g. as degenerate lasers [52], where an imaging system is placed within the resonator. Speckle reduction is also achieved for random lasers [53], where lasing occurs in highly disordered media.

Outline

Chapter 2 gives an introduction into how the coherence properties of light fields can lead to spatial and temporal noise, and how this affects optical dipole trapping of cold atoms. In chapter 3 diffuser-based spatial coherence reduction techniques are discussed. In particular, speckle pattern averaging is implemented using a rotating diffuser and using an acousto-optically modulated angle of incidence. Chapter 4 demonstrates spatial coherence reduction in multimode optical fibres based on modal dispersion induced dephasing of broadband light sources. In chapter 5 the decoherence results are summarized and compared.

2 Theory of Coherence and Dipole Traps

In this chapter the generation of arbitrary potentials for ultracold atoms and the influence of coherent noise is described. Sec. 2.1 provides an introduction to Fourier optics and coherence theory, and sec. 2.2 shows the mechanisms of optical dipole traps.

2.1 Coherence Theory

In order to describe the effects of optical coherence on imaging, properties of partially coherent light fields are derived.

First, scalar diffraction theory (sec. 2.1.1) is introduced explaining the propagation of fully coherent light. Then correlation functions (sec. 2.1.2) used to quantify coherence are discussed, followed by the diffraction properties of partially coherent fields (sec. 2.1.3). Finally, the coherence properties are related to coherent noise reduction in imaging systems (sec. 2.1.4).

2.1.1 Scalar Diffraction Theory

An electromagnetic field $\mathbf{E}(\mathbf{r},t)$ at spatial position $\mathbf{r}=(x,y,z)$ and time t in a source-free, linearly responding, isotropic, non-magnetic, stationary medium with refractive index $n(\mathbf{r},\omega)$ and temporal angular frequency ω evolves according to the homogeneous wave equation [54]

$$\nabla_r^2\mathbf{E}(\mathbf{r})+2\nabla_r(\mathbf{E}(\mathbf{r},t)\cdot\nabla_r\ln n(\mathbf{r},\omega))-\frac{n^2(\mathbf{r},\omega)}{c^2}\partial_t^2\mathbf{E}(\mathbf{r},t)=0, \tag{2.1}$$

with the local speed of light in the medium $c/n(\mathbf{r},\omega)$. In homogeneous media, $n(\mathbf{r},\omega)=n(\omega)$ (or in a weak waveguide, sec. 4.1), the central term vanishes and all spatial dimensions obey the same wave equation, thus allowing consideration of only one component of $\mathbf{E}\to E_i\equiv E$ for any spatial dimension i. For a polarized wave the intensity is given by $I(\mathbf{r},t)=c\,n(\omega)\varepsilon_0|E(\mathbf{r},t)|^2$. For convenience, the scalar value $A\propto E$ absorbs the prefactors to obey $|A|^2=I$.

A time-domain Fourier transform decouples the frequencies ω (implicitly assumed by $n(\omega)$) and yields the Helmholtz equation

$$\nabla_r^2 A(\mathbf{r},\omega) + k^2(\omega) A(\mathbf{r},\omega) = 0, \tag{2.2}$$

with wavenumber $k(\omega) = k_0(\omega)n(\omega)$ and vacuum wavenumber $k_0(\omega) = \omega/c$. As a consequence of linearity, the total field is thus a superposition of independent monochromatic fields.

Diffraction Integral

Considering a light field $A(\tilde{\boldsymbol{\rho}}, \tilde{z})$ where the field distribution in a transversal plane $(\tilde{\boldsymbol{\rho}}, \tilde{z}) = (\tilde{x}, \tilde{y}, \tilde{z})$ is known, the problem of diffraction is to deduce the field in a plane at arbitrary positions z, where z is the optical axis. The Rayleigh-Sommerfeld diffraction formula in the approximation $z - \tilde{z} \gg \lambda$ [54], with wavelength λ, formalizing the Huygens-Fresnel principle of spherical wave superposition, gives the solution as

$$A(\boldsymbol{\rho}, z, \omega) = \frac{k(\omega)(z-\tilde{z})}{2\pi i} \int A(\tilde{\boldsymbol{\rho}}, \tilde{z}, \omega) \frac{e^{ik(\omega)\Delta r}}{\Delta r^2} d^2\tilde{\rho}, \tag{2.3}$$

with difference vector $\Delta\mathbf{r} = (\boldsymbol{\rho} - \tilde{\boldsymbol{\rho}}, z - \tilde{z})$. In particular, it can be written as a superposition integral with an impulse response function h,

$$A(\boldsymbol{\rho}, z, \omega) = \int h_{z-\tilde{z}}(\boldsymbol{\rho}, \tilde{\boldsymbol{\rho}}, \omega) A(\tilde{\boldsymbol{\rho}}, z_0, \omega). \tag{2.4}$$

Propagation through a system can then be modelled by evaluating the diffraction integral between optical elements and changing the wavefront according to the effect of the element.

Paraxial Propagation

If the propagating field has low divergence, $|\boldsymbol{\rho} - \tilde{\boldsymbol{\rho}}| \ll |z - z_0|$, the paraxial approximation can be applied, which involves expanding the positional difference (from the previous section) as $\Delta r/\Delta z \approx 1 + (|\Delta\boldsymbol{\rho}|/\Delta z)^2/2 + \mathcal{O}((|\Delta\boldsymbol{\rho}|/\Delta z)^4)$.

The quadratic wavefront approximation, known as Fresnel approximation, (dropping the independent frequency ω dependence) thus leads to a propagation function of

$$h_{\Delta z}(\boldsymbol{\rho}_2, \boldsymbol{\rho}_1) = \frac{k e^{ik\Delta z}}{2\pi i z} \exp\left(\frac{ik}{2z}(\boldsymbol{\rho}_2 - \boldsymbol{\rho}_1)^2\right), \tag{2.5}$$

whereas for the constant wavefront (far-field, Fraunhofer) approximation one obtains the Fourier transform kernel

$$h_{\Delta z}(\boldsymbol{\rho}_2, \boldsymbol{\rho}_1) = \frac{k e^{ik\Delta z}}{2\pi i z} \exp\left(\frac{ik}{2z}\boldsymbol{\rho}_2^2\right) \exp\left(-\frac{ik}{z}\boldsymbol{\rho}_1 \cdot \boldsymbol{\rho}_2\right). \tag{2.6}$$

It can be shown that in Fresnel approximation a thin lens converts the light field in its front focal plane into its Fraunhofer diffraction pattern in its rear focal plane [54]. Two lenses with focal lengths $f_{1,2}$ in such a configuration Fourier transform the incident field twice and thus constitute a 4f-imaging system with magnification $M = f_2/f_1$. In an ideal, diffraction-limited imaging system the magnification-normalized propagation function then becomes shift-invariant,

$$h(\boldsymbol{\rho}_2, \boldsymbol{\rho}_1) = h(\boldsymbol{\rho}_2/M - \boldsymbol{\rho}_1), \tag{2.7}$$

and the diffraction integral becomes a convolution integral whose Fourier transform defines the amplitude transfer function.

Gaussian Beam

The Fresnel-approximated Helmholtz equation does not only have the paraxial spherical waves as solutions but also a set of Gaussian beams. Typical laser beams are well-approximated by the lowest order mode of the set ("Gaussian beam"), which is given by

$$A(\boldsymbol{\rho}, z) = A_0 \frac{w_0}{w(z)} e^{-ik\rho^2/2R(z)} e^{-\rho^2/w^2(z)}, \tag{2.8}$$

where $w(z) = w_0\sqrt{1 + (z/z_R)^2}$ is the beam width, with waist w_0 and Rayleigh range $z_R = kw_0^2/2$, and $R(z) = z + z_R^2/z$ is the wavefront curvature radius (neglecting the purely longitudinally dependent Gouy phase).

2.1.2 Correlation Functions

The previous section fully describes the behaviour of deterministic light fields. However, when random processes are involved, due to the light field itself or because of changes of the optical system, only statistical predictions can be made.

Generally, a correlation function describes the expectation value of a product of random variables (i.e. their mutual similarity), where it is called autocorrelation if the factors describe the same variables, and cross-correlation if they denote different vari-

ables. In optical coherence theory, one is interested in the correlation properties of a light field $A(\mathbf{r},t)$ and can generally define an n-th order correlation function as

$$\Gamma_A^{(n)}(\{\mathbf{r}_i\},\{\mathbf{r}_i'\},\{t_i\},\{t_i'\}) = \mathrm{E}\left[\prod_{i=1}^{n} A^*(\mathbf{r}_i,t_i)A(\mathbf{r}_i',t_i')\right], \tag{2.9}$$

where $\mathrm{E}[X]$ denotes the expectation value of X over its statistical ensemble. First-order correlation functions are of particular importance as they give lowest order insight into the fluctuations of a quantity of interest and are suitable to describe noise characteristics. The first-order correlations of the field $A(\mathbf{r},t)$ and of its intensity $I(\mathbf{r},t) = |A(\mathbf{r},t)|^2$ are denoted as

$$\begin{aligned}\Gamma_A(\mathbf{r}_1,\mathbf{r}_2,t_1,t_2) &\equiv \Gamma_A^{(1)}(\mathbf{r}_1,\mathbf{r}_2,t_1,t_2) \text{ and}\\ \Gamma_I(\mathbf{r}_1,\mathbf{r}_2,t_1,t_2) &\equiv \Gamma_I^{(1)}(\mathbf{r}_1,\mathbf{r}_2,t_1,t_2) = \Gamma_A^{(2)}(\mathbf{r}_1,\mathbf{r}_2,\mathbf{r}_1,\mathbf{r}_2,t_1,t_2,t_1,t_2).\end{aligned}$$

Since any observable field is a deterministic function, one typically evaluates the time-average of the correlation function

$$\Gamma_A(\mathbf{r}_1,\mathbf{r}_2,\tau) = \mathrm{E}\left[\langle A^*(\mathbf{r}_1,t)A(\mathbf{r}_2,t+\tau)\rangle_t\right], \tag{2.10}$$

where $\langle X(t)\rangle_t = \lim_{T\to\infty}\int_{-T/2}^{T/2} X(t)dt/T$ and Γ_A is called the mutual coherence function. In the case of a random signal the observable deterministic function can be thought of as one (probable) realization from the ensemble, thus the statistical average is kept. The combination of both averages is denoted as $\langle X(t)\rangle = \mathrm{E}[\langle X(t)\rangle_t]$.

The first-order coherence function is defined as the normalized correlation function and is given by

$$\gamma_A(\mathbf{r}_1,\mathbf{r}_2,\tau) = \frac{\Gamma_A(\mathbf{r}_1,\mathbf{r}_2,\tau)}{\sqrt{\Gamma_A(\mathbf{r}_1,\mathbf{r}_1,0)\Gamma_A(\mathbf{r}_2,\mathbf{r}_2,0)}} \tag{2.11}$$

such that the equal-space-time coherence is unity. The modulus of the coherence function, $|\gamma_A(\mathbf{r}_1,\mathbf{r}_2,\tau)|$, is called the degree of coherence. Note that the equal-space-time first-order correlation is the mean intensity, $\Gamma_A(\mathbf{r},\mathbf{r},0) = \langle I_A(\mathbf{r},t)\rangle$.

If one is only interested in the spatial or temporal length scale up to where correlations appear, one can define the coherence length as [55]

$$s_c = \int_{-\infty}^{\infty} |\gamma_A(s)|^2 ds, \tag{2.12}$$

where $s = \tau$ for the coherence time and $s = |\mathbf{r}|$ for the spatial coherence length. Here,

the implied coherence function is $\gamma_A(s) \equiv \gamma_A(\mathbf{s}_0, \mathbf{s}_0 + s\mathbf{e}_{\delta s})$ at a position $\mathbf{s}_0$ measuring the coherence length along a direction $\mathbf{e}_{\delta s}$. For an exponential distribution $e^{-|s|/\sigma}$, this definition yields a coherence length of $s_c = \sigma$, and for a Gaussian distribution $e^{-s^2/2\sigma^2}$ it is $s_c = \sigma\sqrt{\pi}$. Similarly, one can define a coherence area $\mathcal{A}_c = \int |\gamma_A(\mathbf{s})|^2 d^2s$ and a coherence volume $\mathcal{V}_c = \int |\gamma_A(\mathbf{s})|^2 d^3s$.

First-Order Temporal Correlations

The magnitude of coherent noise (interference patterns) in longitudinal direction is described by the temporal first-order correlation function given by the equal-space generic first-order function and, dropping the spatial dependence, is written as

$$\Gamma_A(\tau) = \langle A^*(t)A(t+\tau)\rangle \xrightarrow{\mathcal{F}_\tau} |\mathcal{A}(\omega)|^2 = S_A(\omega), \tag{2.13}$$

where $\mathcal{F}_t$ denotes the asymmetric Fourier transform operator defined as $\mathcal{F}_t\{f(t)\}(\omega) = \int f(t)e^{-i\omega t}dt$. If the field $A(t)$ is deterministic, its Fourier transform $\mathcal{A}(\omega)$ exists and, using the convolution theorem, the Fourier transform relation is proven. If $A(t)$ is a wide-sense stationary random process, different frequency components become uncorrelated and the Wiener-Khinchin theorem [56] can be applied, stating the relation. $S_A(\omega)$ is called the power spectral density of the field ("optical spectrum") and describes the chromatic composition of a light field. Note that normalization by the intensity $\langle I_A(t)\rangle = \int S_A(\omega)d\omega/2\pi$ yields the normalized form in both time and spectral domain, $\gamma_A(\tau) \xrightarrow{\mathcal{F}_\tau} s_A(\omega)$. Also note that for real-valued signals $A(t)$, using the convention of a two-sided power spectral density, it is symmetric in frequency $S_A(-\omega) = S_A(\omega)$.

If a deterministic and a random field have the same spectral composition, the difference between them lies in the phase relation of the Fourier components. While in the deterministic case each frequency has one associated phase, the stochastic nature of the random field requires a phase ensemble averaging, thus the Fourier transform $\mathcal{A}(\omega)$ does not necessarily exist. If a stochastic $\mathcal{A}(\omega)$ is given, it is defined through $S_A(\omega)$ and called the amplitude spectral density.

Using the Wiener-Khinchin theorem (2.13), a definition of the spectral bandwidth can be given as [55]

$$\Delta\nu = \frac{\Delta\omega}{2\pi} = \frac{1}{\int s_A^2(\omega)d\omega}, \tag{2.14}$$

which, using Parseval's theorem and the definition for the coherence length (2.12), is shown to obey the reciprocal relation $\Delta\nu\tau_c = 1$.

Second-Order Temporal Correlations

Temporal fluctuations in intensity can be described with the second-order temporal correlation function

$$\Gamma_I(\tau) = \langle I(t)I(t+\tau)\rangle = \langle A^*(t)A(t)A^*(t+\tau)A(t+\tau)\rangle \xrightarrow{\mathcal{F}_\tau} S_I(\omega), \tag{2.15}$$

where the Wiener-Khinchin theorem is again applied and $S_I(\omega)$ is the intensity power spectral density ("noise spectrum").

If $A(t)$ is a deterministic field (e.g. single-mode laser), insertion of its Fourier transform $\mathcal{A}(\omega)$ yields the relation $S_I(\omega) = |\langle \mathcal{A}^*(\tilde{\omega})\mathcal{A}(\tilde{\omega}+\omega)\rangle|^2$. Thus temporal intensity noise can be interpreted as correlations in the frequency domain. Particularly, this describes mixing of coherent signals such as mode beating.

If $A(t)$ is a random field obeying zero-mean Gaussian statistics ("chaotic light", e.g. thermal sources), the moment theorem [55] yields the Siegert equation

$$\Gamma_I(\tau) = \Gamma_A^2(0) + |\Gamma_A(\tau)|^2, \tag{2.16}$$

relating noise in intensity to first-order (field) coherence properties. Particularly, the carrier-normalized temporal relative intensity noise (RIN) $s_I(\omega)$ can be related to the first-order coherence function $\gamma_A(\tau)$ by $s_I(\omega) = \int |\gamma_A(\tau)|^2 e^{-i\omega\tau} d\tau$, which is inverse to and decays in the order of the optical bandwidth.

Spatial Correlations

Instead of considering temporal correlations, one can analogously study the spatial correlation properties of the field $A(\mathbf{r},t)$ and define the spatial second-order correlation function as

$$\Gamma_A(\mathbf{r}_1,\mathbf{r}_2) = \langle A^*(\mathbf{r}_1,t)A(\mathbf{r}_2,t)\rangle, \tag{2.17}$$

which describes the visibility of a spatial interference pattern (or transversal coherent noise). Note that temporal effects can be included using the cross-spectral density W [55], with $\Gamma_A(\mathbf{r}_1,\mathbf{r}_2) = \int W(\mathbf{r}_1,\mathbf{r}_2,\omega)d\omega$ since different frequencies behave independently (2.2).

Similarly to temporally random fields with vanishing temporal coherence, there also exist spatially random fields where spatial coherence decays. In analogy to temporally statistically stationary fields, one is often interested in Schell model sources, for which

the spatial coherence function depends only on its positional difference,

$$\gamma_A(\mathbf{r}_1, \mathbf{r}_2) \equiv \gamma_A(\mathbf{r}_2 - \mathbf{r}_1). \tag{2.18}$$

Note that fields with Gaussian coherence function and Gaussian intensity envelope are called Gaussian Schell models [57].

Since the formal definitions of coherence always apply infinite time averaging, no statement is made about the rate of convergence to this residual coherence value. Consider a spatially incoherent light source. For an infinitesimal amount of time the wavefront of the field does not change and is thus spatially coherent. In order to become spatially incoherent, the relative phases across the observation plane must change, which happens on the time scale of the coherence time. Therefore, the light field is effectively only spatially incoherent when the observation dynamics happen on time scales which are much longer than the coherence time. If the evolution of the field can be described as a Gaussian random process, the Siegert relation (2.16) can be used to show that the residual coherence of two mutually incoherent fields decays with integration time scale $T \gg \tau_c$ as

$$|\gamma_A| = \sqrt{\frac{\tau_c}{T}}, \tag{2.19}$$

with coherence time τ_c [58]. The coherence value $|\gamma_{A,\mathrm{res}}| \equiv |\gamma_A(\Delta s \to \infty, T \to \infty)|$ will be referred to as "residual coherence", where Δs denotes spatial distance.

The "level of incoherence" of a field is determined by the number of its intrinsic degrees of freedom ("effective number of mutually incoherent modes") M, which can be defined as the ratio of the beam area to the coherence area, $M = \mathcal{A}_I/\mathcal{A}_c$. Let $i(\boldsymbol{\rho}) = I(\boldsymbol{\rho})/\int I(\boldsymbol{\rho})d^2\rho$ denote the normalized intensity envelope, then the coherence area (2.12) can be generalized as $\mathcal{A}_c = \iint i(\boldsymbol{\rho}_1)i(\boldsymbol{\rho}_2)|\gamma_A(\boldsymbol{\rho}_1, \boldsymbol{\rho}_2)|^2 d^2\rho_1 d^2\rho_2$. Defining the beam area analogously, $\mathcal{A}_I = \int i(\boldsymbol{\rho})d^2\rho$, the number of incoherent modes thus yields [59]

$$\frac{1}{M} = \frac{\iint |\Gamma_A(\boldsymbol{\rho}_1, \boldsymbol{\rho}_2)|^2 d^2\rho_1 d^2\rho_2}{\left(\int I_A(\boldsymbol{\rho})d^2\rho\right)^2} \approx \frac{\mathcal{A}_c}{P_A^2}\int I_A^2(\boldsymbol{\rho})d^2\rho, \tag{2.20}$$

where $P_A = \int I_A(\boldsymbol{\rho})d^2\rho$ is the power of the light field, and the approximation is valid for Schell model sources in the incoherent limit. Note that for non-uniform illumination, the integration area is reduced to a region of interest, with a cutoff typically set at the FWHM of the intensity (fig. 2.1). For a Gaussian intensity profile $e^{-\rho^2/2W^2}$, this results in $M = \pi W^2/3\mathcal{A}_c$.

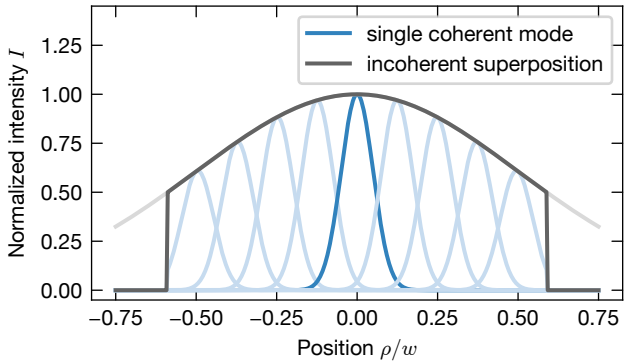

Figure 2.1: **Number of mutually uncorrelated areas.**
The light grey graph shows the Gaussian intensity envelope of an incoherent field with waist w while the blue graphs show the coherence areas generating the beam. In the illustrated (1D) case, the number of mutually incoherent modes is thus $M = 9$ for a full width at half maximum (FWHM) cutoff (dark grey).

2.1.3 Propagation of Correlations

When studying the coherence properties of a light field, rather than at the position of light generation, the properties at a distant plane after propagation through an optical system is typically of interest.

Consider an initial, quasi-monochromatic transversal field $a(\tilde{\boldsymbol{\rho}})$ propagating with function $h_z(\boldsymbol{\rho}, \tilde{\boldsymbol{\rho}})$ (sec. 2.1.1) to a target plane $A(\boldsymbol{\rho})$. Suppose that the propagation function h_z is deterministic (i.e. a known optical system), then one can write Γ_A as the propagated result of the initial correlation function Γ_a,

$$\Gamma_A(\boldsymbol{\rho}_1, \boldsymbol{\rho}_2) = \iint h_z^*(\boldsymbol{\rho}_1, \tilde{\boldsymbol{\rho}}_1) h_z(\boldsymbol{\rho}_2, \tilde{\boldsymbol{\rho}}_2) \Gamma_a(\tilde{\boldsymbol{\rho}}_1, \tilde{\boldsymbol{\rho}}_2) d^2\tilde{\rho}_1 d^2\tilde{\rho}_2. \tag{2.21}$$

Propagation of Schell Model Sources

If a spatially incoherent light field is produced by multiple randomly distributed, independent emitters, their emission statistics are stationary and the light source can be assumed to be a Schell model source. Then it is convenient to express the correlation function in relative, $\Delta\boldsymbol{\rho}$, and mean coordinates, $\boldsymbol{\rho}$, i.e. $\boldsymbol{\rho}_{1,2} = \boldsymbol{\rho} \pm \Delta\boldsymbol{\rho}/2$.

Consider the field propagating to a Fraunhofer diffraction plane (2.6). In the incoherent limit, the coherence function falls off much faster than the intensity envelope, hence $\sqrt{I_a(\boldsymbol{\rho}_1) I_a(\boldsymbol{\rho}_2)}\gamma_a(\Delta\boldsymbol{\rho}) \approx I_a(\boldsymbol{\rho})\gamma_a(\Delta\boldsymbol{\rho})$. Then the correlation integrals factorize such that

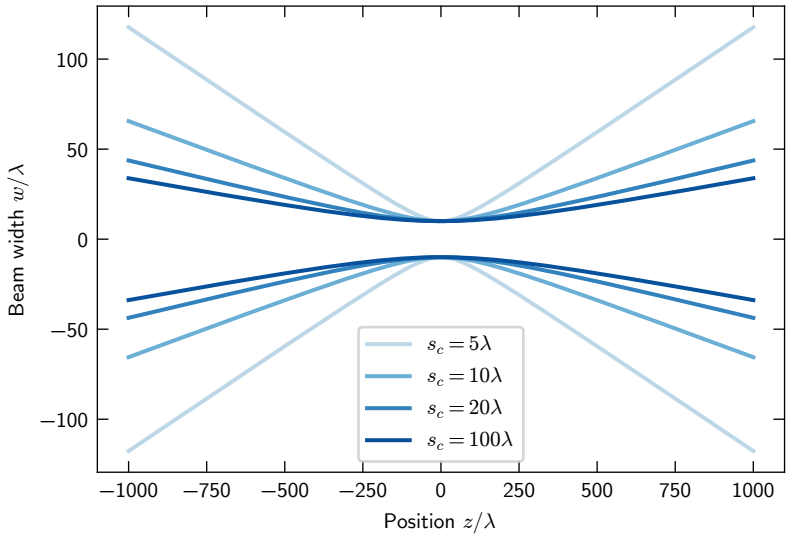

Figure 2.2: **Beam divergence dependence on spatial coherence.** For the same beam waist $w_0 = 10\lambda$ (with wavelength λ), spatially incoherent beams (coherence length $s_c \to 0$) exhibit a much larger divergence w/z than coherent beams ($s_c \to \infty$). Finite numerical aperture (NA) apertures set a bound to divergence, which limits the possible degree of incoherence within an optical system.

one obtains the generalized van Cittert-Zernike theorem [58]

$$\gamma_A(\Delta\boldsymbol{\rho})I_A(\boldsymbol{\rho}) = \left(\frac{k}{2\pi z}\right)^2 \int I_a(\tilde{\boldsymbol{\rho}})e^{-\frac{ik}{z}\tilde{\boldsymbol{\rho}}\cdot\Delta\boldsymbol{\rho}}d^2\tilde{\rho} \int \gamma_a(\Delta\tilde{\boldsymbol{\rho}})e^{-\frac{ik}{z}\Delta\tilde{\boldsymbol{\rho}}\cdot\boldsymbol{\rho}}d^2\Delta\tilde{\rho}. \tag{2.22}$$

Looking at the dependences of the integrals, one observes that the coherence function in the diffraction plane is the Fourier transform of the intensity envelope in the initial plane and vice versa. This can be understood by picturing each coherence area as an individual Gaussian beam. If the coherence area (i.e. waist) of γ_a is small, the divergence becomes large, explaining the broader envelope of intensity I_A. The more coherence areas (i.e. individual beams) exist (which is proportional to the width of the intensity envelope I_a) for a fixed divergence, the finer the diffraction (i.e. interference) pattern γ_A becomes. Since the coherence areas (i.e. beams) are mutually incoherent, γ_A decays quickly, as expected for the coherence function of an incoherent field.

This Fourier transform relation implies that a reciprocity relation ("M-squared value") analogous to (2.14) between source size and divergence is given that remains invariant throughout propagation. For real, finite-sized optical systems, its maximal number is

thus limited by the element with the smallest value for the product of field size in a focus and NA. If the field is too incoherent, it will be clipped, reducing the light power efficiency. Fig. 2.2 shows the divergence of a Gaussian Schell model beam, whose evolving beam width is given by [57]

$$w^2(z) = w_0^2 \left(1 + \left(\frac{2z}{kw_0}\right)^2 \left(\frac{1}{w_0^2} + \frac{\pi}{s_c^2}\right)\right), \tag{2.23}$$

where w_0 denotes the intensity width of a Gaussian beam, s_c the spatial coherence length and k the wavenumber.

Imaging Resolution

For an imaging system, the propagation integral, which maps an input field $a(\tilde{\boldsymbol{\rho}})$ to an output field $A(\boldsymbol{\rho})$, is given by the convolution $A(\boldsymbol{\rho}) = \int h(\boldsymbol{\rho} - \tilde{\boldsymbol{\rho}}) a(\tilde{\boldsymbol{\rho}}) d^2\rho$ (2.7), where w.l.o.g. the magnification is assumed to be unity, $M = 1$. Thus, expressing this statement in Fourier space reduces the relation to a product,

$$\mathcal{A}(\boldsymbol{\nu}) = \mathcal{H}(\boldsymbol{\nu})\alpha(\boldsymbol{\nu}), \tag{2.24}$$

where $\boldsymbol{\nu}$ is the spatial frequency, $\mathcal{H}(\boldsymbol{\nu}) = \mathcal{F}_\rho\{h(\boldsymbol{\rho})\}(\boldsymbol{\nu})$ the amplitude transfer function and $\mathcal{A}, \alpha$ the Fourier transforms of the fields A, a. Fourier transforming the correlation propagation function (2.21), $\mathcal{G}_A(\boldsymbol{\nu}_1, \boldsymbol{\nu}_2) = \mathcal{F}_{\rho_1,\rho_2}\{\Gamma_A(\boldsymbol{\rho}_1, \boldsymbol{\rho}_2)\}(\boldsymbol{\nu}_1, \boldsymbol{\nu}_2)$, thus yields the intensity spectrum

$$\mathcal{I}_A(\boldsymbol{\nu}) = \mathcal{F}_\rho\{I_A(\boldsymbol{\rho})\}(\boldsymbol{\nu}) = \int \mathcal{H}^*(\tilde{\boldsymbol{\nu}})\mathcal{H}(\tilde{\boldsymbol{\nu}} - \boldsymbol{\nu})\mathcal{G}_a(\tilde{\boldsymbol{\nu}}, \tilde{\boldsymbol{\nu}} - \boldsymbol{\nu}) d^2\tilde{\nu}. \tag{2.25}$$

As a transfer function, $\mathcal{H}(\boldsymbol{\nu})$ determines the imaging resolution of a certain spatial frequency $\boldsymbol{\nu}$, where $\mathcal{H}(\boldsymbol{\nu}) = 1$ means a perfect reproduction in the image plane.

In the coherent limit $\mathcal{G}_a(\boldsymbol{\nu}_1, \boldsymbol{\nu}_2) = \alpha^*(\boldsymbol{\nu}_1)\alpha(\boldsymbol{\nu}_2)$, one thus obtains a spatial intensity spectrum of $\mathcal{I}_A(\boldsymbol{\nu}) = \int \mathcal{H}^*(\tilde{\boldsymbol{\nu}})\alpha^*(\tilde{\boldsymbol{\nu}})\mathcal{H}(\tilde{\boldsymbol{\nu}} - \boldsymbol{\nu})\alpha(\tilde{\boldsymbol{\nu}} - \boldsymbol{\nu}) d^2\tilde{\nu}$, whereas the incoherent limit $\mathcal{G}_a(\boldsymbol{\nu}_1, \boldsymbol{\nu}_2) = \mathcal{I}_a(\boldsymbol{\nu}_1 - \boldsymbol{\nu}_2)$ yields $\mathcal{I}_A(\boldsymbol{\nu}) = \mathcal{I}_a(\boldsymbol{\nu}) \int \mathcal{H}^*(\tilde{\boldsymbol{\nu}})\mathcal{H}(\tilde{\boldsymbol{\nu}} - \boldsymbol{\nu}) d^2\tilde{\nu}$.

These relations can be most easily understood when considering a quadratic pupil, which is equivalent to a rectangular transfer function $\mathcal{H}(\boldsymbol{\nu}) = \prod_{i=\{x,y\}} \Theta(\nu_0 - |\nu_i|)$, with spatial cutoff frequency ν_0 and heaviside function Θ. In the coherent case, all frequencies up to ν_0 are perfectly reproduced, resulting in a high contrast, accurate image for large scale structures. In the incoherent case, one has to consider the convolution

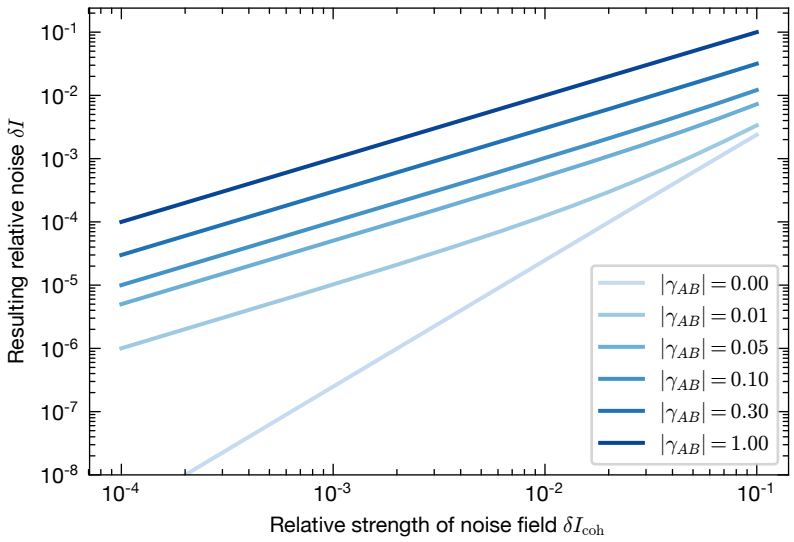

Figure 2.3: **Relative noise level dependence on degree of coherence.** The log-log plot compares the relative noise for fully coherent superpositions δI_{coh} with the relative noise for partial coherence δI at different degrees of coherence $|\gamma_{AB}|$ (2.27). For sufficiently small fluctuations, noise levels decrease proportional to the degree of coherence.

of the amplitude transfer function, i.e. a triangular function $\int \mathcal{H}^*(\tilde{\boldsymbol{\nu}})\mathcal{H}(\tilde{\boldsymbol{\nu}} - \boldsymbol{\nu})d^2\tilde{\nu} = \prod_{i=\{x,y\}}(1 - |\nu_x|/2\nu_0)\Theta(2\nu_0 - |\nu_i)$. The sub-unity values for finite spatial frequencies indicate a reduction in image contrast, but the larger achievable spatial frequencies (up to $2\nu_0$) enable higher resolution. In summary, incoherent imaging leads to higher resolved but more blurred images and reduces ringing artefacts.

2.1.4 Reduction of Coherent Noise

The goal of an imaging system is to propagate a given intensity distribution from an object plane to an image plane, where a scaled, diffraction limited copy of this intensity distribution is produced. In real systems, imperfections always lead to deviations in the light field.

Consider a target intensity distribution $I_A(\boldsymbol{\rho})$ and a noise field $B(\boldsymbol{\rho}, t)$. The resultant intensity is then given by the noise-averaged, coherent field superposition

$$I_{A+B}(\boldsymbol{\rho}) = I_A(\boldsymbol{\rho}) + \langle I_B(\boldsymbol{\rho}, t)\rangle_t + 2\sqrt{I_A(\boldsymbol{\rho})\,\langle I_B(\boldsymbol{\rho}, t)\rangle}\,\mathrm{Re}[\gamma_{AB}(\boldsymbol{\rho}, t)], \tag{2.26}$$

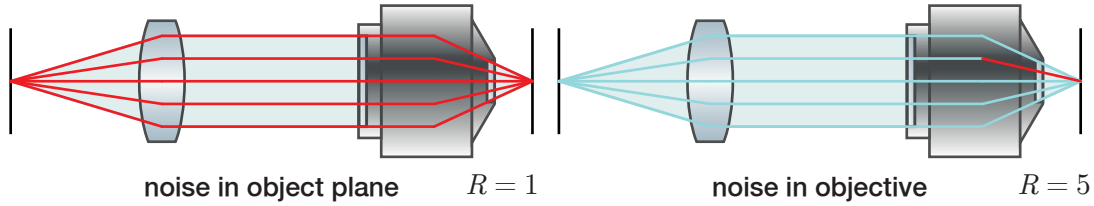

Figure 2.4: **Wave redundancy for noise in different planes.**
The illustration shows five mutually incoherent (blue) rays propagating through an imaging system. If a noise source (generating red rays) is located in the object/an intermediate image plane (left), the same coherence area is imaged onto the image plane, so the wave redundancy is $R = 1$ and spatial incoherence does not suppress noise. In the typical case of noise in the objective plane (right), a point in the image plane is illuminated by multiple rays, here $R = 5$, such that coherent noise is suppressed.

where the interference induced noise magnitude is proportional to the modulus of the cross-correlation $|\Gamma_{AB}|$ (the last term). Assuming that the noise source cannot be removed or avoided, the incoherent intensity addition gives the lower noise bound. Writing the noise terms relative to the target intensity, $\delta I = I_{A+B}/I_A - 1$, gives the relation plotted in fig. 2.3,

$$\delta I(|\gamma_{AB}|) = \delta I_{\mathrm{coh}} - 2(1 - |\gamma_{AB}|)(\sqrt{1 + \delta I_{\mathrm{coh}}} - 1) \approx |\gamma_{AB}|\delta I_{\mathrm{coh}}, \tag{2.27}$$

where $\delta I_{\mathrm{coh}} = \delta I(|\gamma_{AB}| = 1)$ is the relative noise at full coherence.

Estimation of the actual noise reduction is difficult as it does not only depend on the noise properties and position, but also on the illuminating light field (which for an arbitrary image can vary strongly). To provide a qualitative picture, imagine the image formation process as the superposition of different modes (fig. 2.4). One can formally define the wave redundancy [60] given by

$$R(\boldsymbol{\rho}) = \sum_{n \in \mathcal{N}(\boldsymbol{\rho})} \frac{|a_n|^2}{\max_k |a_k|^2}, \tag{2.28}$$

where a_n denotes the weight of mutually incoherent modes and the summation goes over $\mathcal{N}(\boldsymbol{\rho})$, which are the modes constituting the field at an observation point $\boldsymbol{\rho}$. $R(\boldsymbol{\rho}) \to 1$ means that all the light at $\boldsymbol{\rho}$ in the image plane comes from a single mode of the noise plane, whereas $R(\boldsymbol{\rho}) \to \infty$ means that the noise source only contributes an infinitesimal amount. Thus the effective coherence is expected to be limited by $|\gamma_{AB}| \to |\gamma_{AB}| + 1/R$.

First, consider planar reflections (e.g. at plane-parallel windows) such that the noise field is given by the time-delayed superposition of the target field $B(t) = \sum_n \eta_n A(t-\tau_n)$, where η_n is the relative strength of the n-th reflection. Then the wave redundancy yields $R = 1/\sum_n \eta_n$ and the interference term is thus given by $\delta I \approx I_A \sum_n \eta_n \gamma_A(\tau_n)$ such that coherence times smaller than the reflection delays can significantly reduce noise.

Second, consider scatterers in an arbitrary plane of the image path, as illustrated in fig. 2.4. If the noise source is located in a Fourier plane, every image point is illuminated by all modes, such that the wave redundancy is maximal, $R \to \infty$. Since typically the scatterer is located at the objective, this case is often fulfilled and eq. (2.27) can be used to estimate the noise reduction. However, if the scatterer is located in the object or an intermediate image plane, the wave redundancy is minimal for a perfect imaging system, $R = 1$. For a finite point spread function, the noise is correspondingly slightly reduced.

2.2 Optical Dipole Traps

In this section optical dipole traps for neutral atoms are introduced and the influence of partial coherence on spatial inhomogeneities and system heating is discussed.

2.2.1 Atomic Light Shifts

When considering the interaction between a light field $\mathbf{E}(\mathbf{r}, t)$ and an atom in state $|i\rangle$, the realization that electronic dynamics happen on much faster time scales than nuclear dynamics allows for an adiabatically approximated approach, separating the dynamics of the "internal" electronic part from the nuclear centre-of-mass part. As typical extents of atoms are in the subnanometre regime, i.e. much smaller than optical wavelengths at hundreds of nanometres, the electric dipole approximation can be applied and the field can be treated as locally homogeneous. If only one valence electron is involved, the electronic Hamiltonian reduces to a hydrogen-like problem in a spatially homogeneous field $\mathbf{E}(t)$. The electronic field-free eigenenergy difference between states $|j\rangle$ and $|i\rangle$ will be denoted as $\hbar\omega_{ji} = E_j - E_i$.

If only single-photon effects are taken into account, different photonic frequencies ω and polarizations $\boldsymbol{\epsilon}_p$ can be considered independently, resulting in the Hamiltonian

$$\hat{H}'(\omega, p) = e\hat{\mathbf{r}} \cdot \boldsymbol{\mathcal{E}}_p(\omega) = \sum_{i,j} \hbar d_{ji}(p) \mathcal{E}_p(\omega) \, |j\rangle \langle i| \,, \tag{2.29}$$

where $\mathcal{E}_p(\omega)$ is the respective Fourier component of the field $\mathbf{E}(t)$, $d_{ji}(p) = \langle j| e\hat{\mathbf{r}} \cdot \boldsymbol{\epsilon}_p |i\rangle$ is the dipole matrix element and the Rabi frequency $\Omega_{ji}(\omega, p) = d_{ji}(p)\mathcal{E}_p(\omega)$ can be defined. For small coupling with respect to detuning, $\Delta_{ji}(\omega) = \omega - \omega_{ji} \gg \Omega_{ji}(\omega, p)$, second-order perturbation theory yields an eigenenergy shift for the state $|i\rangle$ of [61]

$$\Delta E_{ji}(\omega, p) = \frac{s_p(\omega)}{2\pi} \frac{\hbar |d_{ji}(p)|^2}{\Delta_{ji}(\omega)} 2\varepsilon_0 c I, \tag{2.30}$$

where $S_p(\omega) = I s_p(\omega) \propto |\mathcal{E}_p(\omega)|^2$ denotes the (two-sided) optical power spectral density (2.13) and I is the total light intensity. Note that using the Wigner-Eckart theorem, the dipole matrix element $d_{ji}(p)$ can be factorized into the spherically symmetric reduced matrix element $\|d_{ji}\|$ and a branching factor $c_{ji}(p)$ [62].

The total light shift is obtained by summing the contribution from each frequency, polarization and coupling state, $\Delta E_i = \int d\omega \sum_p \sum_{j \neq i} \Delta E_{ji}(\omega, p)$. For the typical case, where $|i\rangle$ is a ground state, the detuning $\Delta(\omega)$ is large compared to the energy splitting ω_0 between relevant excited states $|j\rangle$ and the light polarization is spectrally independent $s_p(\omega) = s_p s(\omega)$, the light shift can be reduced to

$$\Delta E_i = \frac{3\pi c^2}{2\omega_0^3} \int \frac{d\omega}{2\pi} s(\omega) \frac{\alpha_i \Gamma}{\Delta(\omega)} I, \tag{2.31}$$

where $\Gamma = \omega_0^3 \|d_0\|^2 / 3\pi\varepsilon_0 \hbar c^3$ denotes the spontaneous decay rate and the factor $\alpha_i = \sum_p \sum_{j \neq i} s_p |c_{ji}(p)|^2$ accounts for selection rules. Note that apart from α_i, this result recovers the classical dipole potential, where the light field interacts with an induced atomic dipole.

Since the dynamics of the whole atom depends only parametrically on the electronic state, its total energy varies according to the light intensity. Spatially varying intensity distributions $I(\mathbf{r})$ thus allow the creation of arbitrary, internal state $|i\rangle$ dependent potential landscapes $U_i(\mathbf{r}) = \Delta E_i(\mathbf{r}) \propto I(\mathbf{r})$.

2.2.2 Heating of Trapped Atomic Systems

Since one is typically interested in atoms in well-defined quantum states, heating processes are undesirable, as they induce uncontrolled state changes. Electronic (internal) state changes pose a problem since trapping potentials, detection mechanisms and observable physics are often state-selective. When studying itinerant physics, it is also important to avoid motional state changes induced by fluctuating potentials.

Photon Scattering

One such process is spontaneous photon scattering, which can be seen as coherent photon absorption $\mathbf{k}_1$ and reemission $\mathbf{k}_2$, with which a momentum transfer is associated, depositing an energy of $E_{\mathrm{sc}}(\mathbf{k}_1, \mathbf{k}_2) = \hbar^2(\mathbf{k}_2 - \mathbf{k}_1)^2/2m$, where m is the mass of the atom. Assuming the energy splittings within ground states to be small compared to the light frequency and demanding energy conservation up to E_{sc} implies quasi-elastic scattering $\omega_1 \approx \omega_2$. Neglecting polarization and anisotropy effects, the heating rate for state $|i\rangle$ is thus given by [61]

$$P_{\mathrm{sc},i} = \frac{\hbar^2 c^2}{m} \int \frac{d\omega}{2\pi} s(\omega)\omega^2 \Gamma_{\mathrm{sc},i}(\omega), \tag{2.32}$$

where $\Gamma_{\mathrm{sc},i}(\omega)$ denotes the photon scattering rate.

Again only considering single-photon effects, scattering can be modelled within a homogeneously broadened two-level system. In the large detuning limit the steady-state solution of the optical Bloch equation then yields

$$\Gamma_{\mathrm{sc},i}(\omega) = \frac{3\pi c^2}{2\hbar\omega_0^3} \left(\frac{\Gamma}{\Delta(\omega)} \right)^2 I, \tag{2.33}$$

with the spontaneous emission rate Γ. Since the scattering rate decreases faster with detuning than the light shift, $\Delta E_i/\Gamma_{\mathrm{sc},i} \propto 1/\Delta$, far off-resonant light is typically used for dipole traps.

Parametric Heating

Apart from photon scattering, the motional state of an atom can also be directly changed by classical fluctuations of the optical dipole potential (i.e. the light intensity). For analysis, the potential $V(\mathbf{r}, t) = V_0(\mathbf{r}) + V_\epsilon \epsilon(\mathbf{r}, t)$ is decomposed into a static target potential $V_0(\mathbf{r})$ and a spatiotemporal noise term $\epsilon_r(\mathbf{r}) \equiv \langle \epsilon(\mathbf{r}, t) \rangle$.

First, the case of a spatially coherent field is considered, such that perfect correlations across the field exist and the dependence on the position factorizes, $\epsilon(\mathbf{r}, t) = \epsilon_r(\mathbf{r})\epsilon_t(t)$. The noise effects can be described in terms of transition rates between motional states of the atoms within first-order time-dependent perturbation theory and are given by

$$\Gamma_{mn} = \frac{1}{\hbar^2} |\langle m| V_\epsilon \epsilon_r(\mathbf{r}) |n\rangle|^2 S_{\epsilon_t}(\omega_{mn}), \tag{2.34}$$

where $\hbar\omega_{mn}$ is the energy difference between the corresponding states and $S_{\epsilon_t}(\omega)$ is the relative temporal intensity power spectral density (2.15). It is thus evident that resonant

noise has to be minimized to avoid driving these transitions. If one is interested in dynamics in the temporal regime τ where the $|m\rangle \leftrightarrow |n\rangle$ transitions are temporally resolved, $\omega_{mn} \lesssim 1/\tau$, fluctuations in this frequency regime can lead to random adiabatic state changes. Therefore temporal noise is only acceptable for fluctuation frequencies much larger than any relevant transition frequency.

Second, if the field is incoherent, one can distinguish between fluctuations which are mutually independent between different coherence areas and global fluctuations influencing all coherence areas simultaneously. Since the light field is required to appear spatially incoherent for the atomic system (2.19), it can be assumed that fluctuations at the time scales of the prior are much faster and therefore insignificant. Taking into account only the global fluctuations, the temporal fluctuation statistics are position independent, allowing $\epsilon(\mathbf{r}, t) = \epsilon_r(\mathbf{r})\epsilon_t(t)$ to again be factorized, yielding the above result.

Note that the energy deposited in the system is directly given by the transition energy $E_h = \hbar\omega_{mn}$.

As an example consider a harmonic trap potential $V_0(x) = m\omega_0^2 x^2/2$ with trap frequency ω_0. Assuming that the trap potential itself is globally fluctuating $\epsilon_r(x) \propto V(x)$, one obtains a transition rate of $\Gamma_{mn} \propto |\langle m| \hat{x}^2 |n\rangle|^2 S_{\varepsilon_t}(\omega_{mn}) \propto \delta_{n+2,n} S_{\varepsilon_t}(2\omega_0)$ and, since the energy levels are equidistantly spaced, exponential heating [63].

2.2.3 Influence of Spatial Noise

In order to determine the effect of static spatial noise in optical potentials, consider the a setting in which atoms are trapped in a two-dimensional (2D) square lattice $V(\boldsymbol{\rho}) = V_0(\sin^2(k_{\text{lat}}x) + \sin^2(k_{\text{lat}}y))$ with lattice wavenumber k_{lat}. For bosons, a contact interaction and a tight binding approximation for the Wannier functions $\langle \boldsymbol{\rho}|i\rangle = w_i(\boldsymbol{\rho}) = w(x - x_i)\, w(y - y_i)$ yields the Bose-Hubbard model [64]

$$\hat{H} = -J \sum_{\langle i,j \rangle} \hat{a}_i^\dagger \hat{a}_j + \frac{U}{2} \sum_i \hat{n}_i(\hat{n}_i - 1) + \sum_i (\epsilon_i - \mu)\hat{n}_i, \tag{2.35}$$

where $\hat{a}_i^\dagger$ ($\hat{a}_i$) denotes the particle creation (annihilation) operator at lattice site i, $\hat{n}_i = \hat{a}_i^\dagger \hat{a}_i$ is its number operator and μ is the chemical potential. The kinetic energy term J describes hopping between adjacent lattice sites, U the contact interaction and ϵ_i the

local on-site energy. These parameters are given by

$$
\begin{aligned}
J &= \langle j| \hat{H}_0 |i\rangle \approx 2E_r\sqrt{v_0}e^{-2\sqrt{v_0}}, \\
U &= \frac{4\pi\hbar a_s}{m}\int |w_i(\boldsymbol{\rho})|^4 d^2\rho \approx 4a_s E_r\sqrt{v_0}, \\
\epsilon_i &= \langle i| \hat{V} |i\rangle \approx E_r\sqrt{v_0},
\end{aligned}
$$

where $\hat{H}_0 = \hat{p}^2/2m + \hat{V}$ is the atomic Hamiltonian, $v_0 = V_0/E_r$ is the normalized potential magnitude, m is the atomic mass, a_s is the normalized scattering length and $E_r = \hbar^2 k_{\mathrm{lat}}^2/2m$ is the recoil energy. The approximations are obtained for harmonic expansion of the potential and are valid in the Lamb-Dicke regime, i.e. $V_0 \gg E_r$. Since scattering lengths are short and the exponential term small, the on-site energy is the largest term $\epsilon_i \gg U, J$.

First, consider the case in which the lattice potential is projected and the trap frequencies vary at certain sites, i.e. a proportional scaling factor is introduced such that locally $V(\boldsymbol{\rho}) \to (1+\delta)V(\boldsymbol{\rho})$. Since the absolute value ϵ_i is by far the largest compared to the other parameters, fluctuations δ can easily lead to on-site energy changes larger than U, J, significantly impacting dynamics. The on-site energy thus scales as $\epsilon_i \to \epsilon_i\sqrt{\delta}$.

However, projected potentials are typically diffraction limited and cannot realize tightly spaced lattice sites. A more probable type of speckle noise is a potential variation which can be assumed to be constant over one lattice site. In this case a local offset is introduced, $V(\boldsymbol{\rho}) \to V(\boldsymbol{\rho}) + V_0\,\delta$, and the on-site energy scales as $\epsilon_i \to \epsilon_i + V(\boldsymbol{\rho}_i)\,\delta$.

Following eq. (2.27) the use of light with reduced spatial coherence $|\gamma_A|$ proportionally reduces fluctuations $\delta \to |\gamma_A|\,\delta$. Therefore noise is reduced by a factor of $\sqrt{|\gamma_A|}$ or $|\gamma_A|$, respectively.

3 Diffuser-Controlled Decoherence

Since coherent light sources provide the advantage of high control and intensity, it is desirable to continue to use these sources and change their coherence properties. As spatial coherence means that a light beam is mutually phase stable in a given propagation plane, coherence can be reduced by dynamically shaping the wavefront where the phase-modulation pattern is chosen in such a way that the mean phase change vanishes.

In sec. 3.1 the properties of diffusers and modulation-controlled decoherence effects are derived. Sec. 3.2 describes the experimental setup used to obtain the results for static speckle characterization (sec. 3.3) and coherence reduction due to a rotating diffuser (sec. 3.4) and acousto-optic beam deflection (sec. 3.5).

Diffuser-Based Wavefront Modulation

When spatially and temporally coherent, polarized light illuminates an object structured on the scale of the wavelength ("diffuser"), the light is scattered at the microscopic diffractive elements that locally distort the wavefront. Considering a large number of such illuminated grains, the observed light field is a coherent superposition of the scattered light, thus producing an interference pattern. As the diffracting structures ("scatterers", "grains") of diffusers are random surface height fluctuations, the interference pattern is also random and is called a speckle pattern (individual patches of similar intensity are called "speckles").

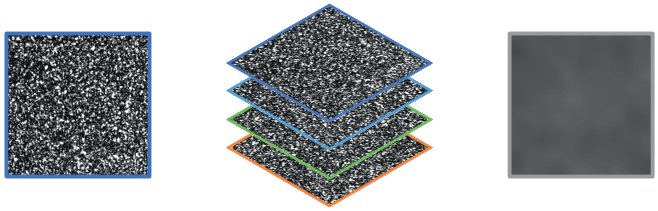

Figure 3.1: **Temporal averaging of uncorrelated speckle patterns.** Integrating a series (middle) of uncorrelated speckle patterns (left) over time averages out the mean intensity (right). As the averaging process between two distant points are uncorrelated, the resulting field is spatially incoherent.

When the diffuser structure changes in time, the speckle pattern also changes and temporal integration leads to a blurring of the observed field (fig. 3.1). As the statistics of the diffracted field reflects the statistics of the diffuser structure, globally uncorrelated modulation patterns produce the desired spatially incoherent light source. Assuming a fixed spot illuminating the diffuser, the required phase modulation can be obtained by moving the diffuser relative to the spot (e.g. moving the diffuser) or by varying the illumination conditions (e.g. the angle of incidence).

3.1 Theory

In this section the statistical properties of speckles are derived for both the static and the dynamically modulated case.

A diffuser is a transparent plane plate whose surface is roughened on the light exiting side, thus its bulk approximately does not change the incident wavefront and its only effect is a position-dependent phase delay due to varying surface heights of the optically dense diffuser material. Assuming these phase delays to be stochastic, this results in a random phase screen, where propagation obeys Fresnel diffraction (2.5). In order to analyse speckles to deduce information on the second-order coherence properties of the resulting light field, knowledge about one-point (first-order statistics in sec. 3.1.1) and two-point (second-order statistics in secs. 3.1.2 and 3.1.3) correlation functions is necessary.

3.1.1 Speckle Noise Statistics

Consider a spatiotemporally coherent light beam incident on a random phase screen and uniformly illuminating a large number of scatterers. In the far field near the optical axis, the spatial dependence can be dropped for first-order statistics as all scatterers contribute to the field. The resulting complex scattering field $\tilde{A}$ is thus given by a coherent superposition of the diffraction fields $\tilde{a}_n$ created by each emitter (i.e. scatterer) and yields $\tilde{A} = \sum_n \tilde{a}_n = Ae^{i\theta}$, where (A, θ) denotes its polar decomposition.

Since the scatterers are uniformly illuminated, and considering the emitters as independent identically distributed complex random variables $a_n e^{i\theta_n}$, the problem becomes a random walk in amplitude space and the central limit theorem (CLT) can be applied for the real and imaginary parts, yielding Gaussian distributions with standard deviation σ_A. Transforming this probability distribution into polar representation gives rise to the

Rayleigh distribution

$$p_{A,\theta}(A,\theta) = \frac{A}{2\pi\sigma_A^2} e^{-A^2/2\sigma_A^2}, \tag{3.1}$$

where $p_{A,\theta}$ denotes the joint probability density function of A and θ. Replacing the amplitude by intensity $I = A^2$ and performing the trivial phase integral over θ gives an exponential probability density function for the intensity,

$$p_I(I) = \frac{1}{2\sigma_A^2} e^{-I/2\sigma_A^2} = \frac{1}{\mathrm{E}[I]} e^{-I/\mathrm{E}[I]}, \tag{3.2}$$

where the statistical moments $\mathrm{E}[I^q] = q!\,\mathrm{E}[I]^q$ are substituted and $\mathrm{E}[X]$ indicates the ensemble average of X. In particular, note that the relative root mean square (RMS) intensity deviation, called speckle contrast in this context, is given by

$$C = \frac{\Delta I}{\mathrm{E}[I]} = 1, \tag{3.3}$$

with variance $\Delta I^2 = \mathrm{E}[I^2] - \mathrm{E}[I]^2$, thus indicating a large range of possible intensity values typical for interference patterns.

Since all points around the centre of the observation plane are assumed to be statistically identically illuminated but uncorrelated, the spatial distribution of intensities reflects the first-order statistics, resulting in a light field with large intensity fluctuations, i.e. the speckle pattern. Patterns with unity contrast, i.e. fulfilling eq. (3.3), are called fully developed speckles.

An analysis for finite numbers N of coherent superpositions yields a speckle contrast of $C = \sqrt{1 - 1/N}$ [58]. Considering this behaviour as an estimate of the convergence to the above probability distribution and noting that diffractive grain sizes are commonly well below ten times the beam size, the exponential behaviour can be seen as practically always valid.

Intensity Superposition

When temporally modulating the phase screen, different uncorrelated speckle patterns are sequentially realized. If the modulation is faster than the observation response, the intensity is temporally integrated such that an incoherent (intensity) superposition of fields is measured.

Independent speckle patterns arise when the scattering emitters, being random variables, individually change their particular realization. The degrees of freedom to achieve this include illumination of uncorrelated scattering areas, polarization and wavelength

diversity or the shape of the illuminating wavefront. Incoherent superpositions can thus be induced by sequentially changing above parameters.

Considering the intensity superposition of N independent, fully developed speckle patterns $I = \sum_{n=1}^{N} I_n$ with the same mean intensity $\langle I_n \rangle$, it can be shown [58] that the probability distribution of the intensity is given by a gamma density function

$$p_I(I) = \frac{N^N I^{N-1}}{\Gamma(N)\mathrm{E}[I]^N} e^{-IN/\mathrm{E}[I]} \xrightarrow{N\to\infty} \frac{1}{\sqrt{2\pi}\Delta I} e^{-(I-\mathrm{E}[I])^2/2\Delta I^2} \tag{3.4}$$

which, due to the CLT, quickly converges to a Gaussian. The distribution has mean intensity $\mathrm{E}[I] = N\langle I_n \rangle$ and variance $\Delta I^2 = N\langle I_n \rangle^2$, which gives the contrast

$$C = \frac{1}{\sqrt{N}} \tag{3.5}$$

and thus has a scaling with N expected for statistically independent sums. It turns out that for monochromatic fields the contrast is a measure for the residual spatial coherence $|\gamma_{A,\mathrm{res}}| \approx C$ (sec. 3.1.3).

The above probability distribution is reasoned for superpositions of discrete speckle patterns. For continuous superpositions, where correlations decrease smoothly, a speckle decorrelation time can be defined, such that after discretisation the gamma density function remains valid [58].

3.1.2 Static Correlations

In order to provide a spatially dependent description of the field, the two-point correlation function of the diffracted spatial field profile $A(\boldsymbol{\rho}, z)$ is evaluated, where $\boldsymbol{\rho} = (x, y)$ is the transversal and z is the longitudinal coordinate. Given the correlation properties of the field immediately after the random phase screen $a(\boldsymbol{\rho})$, the correlation propagation formalism (sec. 2.1.3) is used to obtain the correlations in the observation plane. Note that this section treats static (ensemble-averaged) correlations $\tilde{\Gamma}_A$ and not temporally averaged correlation functions Γ_A, i.e. $\tilde{\Gamma}_A(\boldsymbol{\rho}_1, \boldsymbol{\rho}_2) = \mathrm{E}[A^*(\boldsymbol{\rho}_1, t)A(\boldsymbol{\rho}_2, t)]$ is implied.

Field Correlations

For a coherent incident light field $a_{\mathrm{in}}(\boldsymbol{\rho})$, the correlation function can be written as a product of the deterministic field and a random phase delay ϕ due to the diffuser, $\tilde{\Gamma}_a(\boldsymbol{\rho}_1, \boldsymbol{\rho}_2) = a^*_{\mathrm{in}}(\boldsymbol{\rho}_1)a_{\mathrm{in}}(\boldsymbol{\rho}_2)\mu_{\phi,\phi}(\boldsymbol{\rho}_1, \boldsymbol{\rho}_2)$, where $\mu_{\phi,\phi}(\boldsymbol{\rho}_1, \boldsymbol{\rho}_2) = \left\langle e^{i(\phi(\boldsymbol{\rho}_2)-\phi(\boldsymbol{\rho}_1))} \right\rangle$ is the (probability theoretical) joint characteristic function of ϕ. Note that since in this model

the phase delay results from surface height fluctuations, it has a chromatic dependence $\phi(\boldsymbol{\rho}) = k_0 n h(\boldsymbol{\rho})$, with vacuum wavenumber k_0, refractive index of the diffuser material n and its local surface height $h(\boldsymbol{\rho})$ along the optical axis.

In order to evaluate the characteristic function, assume that the phase delays are Gaussian distributed, with width σ_ϕ, and spatially wide-sense stationary, i.e. the correlation of the phase delays can be written as $\tilde{\Gamma}_\phi(\Delta\boldsymbol{\rho}) = \sigma_\phi^2 \tilde{\gamma}_\phi(\Delta\boldsymbol{\rho})$, with correlation coefficient $\tilde{\gamma}$ and difference coordinate $\Delta\boldsymbol{\rho} = \boldsymbol{\rho}_2 - \boldsymbol{\rho}_1$. Then the characteristic function becomes [58]

$$\mu_\phi(\Delta\boldsymbol{\rho}) = e^{-\sigma_\phi^2(1-\gamma_\phi(\Delta\boldsymbol{\rho}))}. \tag{3.6}$$

If the incident field is a plane wave, resulting phase fluctuations are purely introduced by the diffuser such that its (normalized) correlation function follows the characteristic function, $\tilde{\gamma}_a \to \mu_\phi$. If the wavefront is curved, propagation does not change on average, but scattering introduces an angular spread which increases divergence.

As the spatial dependence of μ_ϕ is only given by its phase delay correlations, the density of individual scattering grains on the diffuser determine the shape around the coherence maximum. At large separations, when the phase delay correlations have decayed, the field correlations exhibit an asymptotic normalized correlation value of $\mu_{\phi,\mathrm{res}} = e^{-\sigma_\phi^2}$, so residual correlations are determined by how evenly the phase delays are distributed. As the phase delays are proportional to the local diffuser surface height, the depth of the grains determine the fraction of scattered light. Note that since the phase is periodic, increasing σ_ϕ corresponds to an increasingly uniform distribution.

Intensity Correlations

Since recorded speckle patterns are intensity images, it is of interest to relate the intensity correlation function to the field coherence. As the fields $a_i = a(\boldsymbol{\rho}_i)$ are circular complex Gaussian random variables, Reed's theorem [65] $\langle a_1^* a_2^* a_1 a_2 \rangle = \langle a_1^* a_1 \rangle \langle a_2^* a_2 \rangle + \langle a_1^* a_2 \rangle \langle a_1 a_2^* \rangle$ is applicable such that the intensity correlation becomes

$$\tilde{\Gamma}_I(\boldsymbol{\rho}_1, \boldsymbol{\rho}_2) = I(\boldsymbol{\rho}_1) I(\boldsymbol{\rho}_2)(1 + |\tilde{\gamma}_A(\boldsymbol{\rho}_1, \boldsymbol{\rho}_2)|^2), \tag{3.7}$$

in analogy to the Siegert relation (2.16) for chaotic light in the temporal domain.

Gaussian Schell Model for Speckle Field

Typically, the diffuser phase delay is assumed to have a Gaussian spatial correlation with width r_c [58], giving the characteristic function $\mu_\phi(\Delta\rho) = \exp\Big(-\sigma_\phi^2(1 - e^{-\Delta\rho^2/r_c^2})\Big)$. For

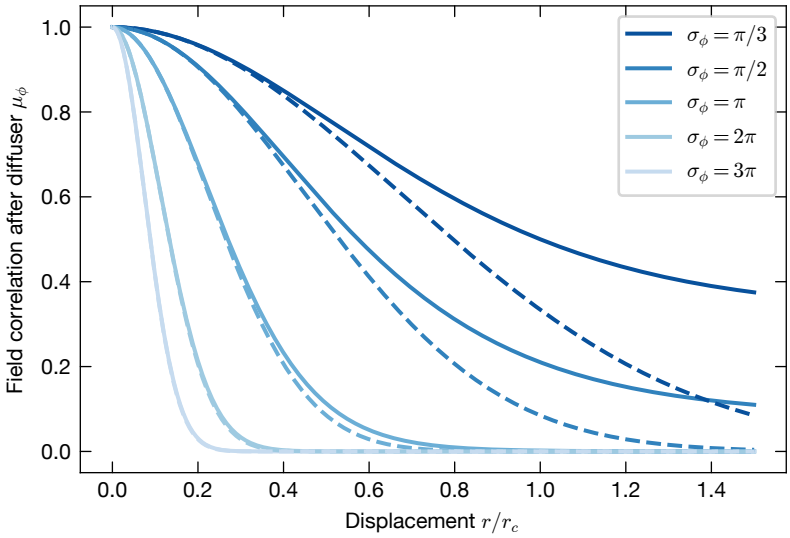

Figure 3.2: **Field correlations immediately after a Gaussian diffuser.** The characteristic function μ_ϕ of a diffuser with Gaussian first-order (surface roughness distribution width σ_ϕ) and second-order statistics (correlation length r_c) describes the field correlations γ_a immediately after the diffuser for planar wavefront incidence. The dashed lines show the Gaussian approximation to the exact solid lines. The short-range approximation fits well, but the asymptotic residual coherence is not captured.

sufficient phase randomization, $\sigma_\phi \gtrsim \pi$ (i.e. most incident light is scattered, fig. 3.2), it can be approximated as Gaussian with width $\tilde{\rho}_c = r_c/\sqrt{2}\sigma_\phi$ [66]. For illumination with a centred, monochromatic, Gaussian beam with waist w, the resulting light field thus constitutes a Gaussian Schell model (2.18). Using the generalized van Cittert-Zernike theorem (2.22), the correlation function in a Fraunhofer diffraction plane then becomes

$$\tilde{\Gamma}_A(\rho, \Delta\rho) = \frac{1}{2}\left(\frac{r_c w}{\sigma_\phi}\right)^2 I_0 e^{-\rho^2/2W^2(z)} e^{-\Delta\rho^2/2\rho_c^2(z)}, \tag{3.8}$$

where the first exponential term corresponds to the scattered intensity envelope and the last term is the normalized correlation function. The respective Gaussian widths are given by

$$\rho_c(z) = \frac{2z}{kw} \text{ and } W(z) = \frac{z}{k\tilde{\rho}_c}. \tag{3.9}$$

Here ρ_c denotes the Gaussian width of the field, thus (3.7) the Gaussian width of the intensity ("speckle size") is $x_c = \rho_c/\sqrt{2}$ and the coherence length, as defined in eq. (2.12), yields $s_c = x_c\sqrt{2\pi}$.

The number of mutually uncorrelated areas (2.20) for a cutoff at the FWHM of the intensity, $W\sqrt{2\ln 2}$, is given by

$$M(z) = \frac{\pi}{3}\frac{W^2(z)}{\mathcal{A}_c(z)} = \frac{1}{6\pi}\frac{W^2(z)}{x_c^2(z)} = \frac{\pi}{3}\frac{(w/\sqrt{2})^2}{(2\pi\tilde{\rho}_c)^2} = M_0, \tag{3.10}$$

where M_0 is the number of uncorrelated areas immediately after the diffuser. Thus, although the speckle size $x_c(z)$ scales upon propagation, the speckle number remains constant.

If the requirement of a deep random phase screen is not fulfilled, $\sigma_\phi \lesssim \pi$, a significant part of the light power is coherently transmitted and gives rise to an intensity spot much smaller than the diffracted width W.

3.1.3 Dynamic Correlations

As the diffuser is used to reduce the coherence of a given light source, the spatial and temporal coherence functions are calculated for the experimentally used modulation schemes. Monochromatic Gaussian beam illumination is assumed as incident light field.

Moving Diffuser

Consider a static beam illuminating a diffuser which moves transversally along the path $\mathbf{d}(t)$. As the effect of the diffuser is a random phase delay, the only modification required of the static correlation function is to introduce a parametric time dependence of the position $\boldsymbol{\rho} \to \boldsymbol{\rho} + \mathbf{d}(t)$. Thus using the static diffraction result (3.8) and averaging over time gives the spatiotemporal coherence function [66]

$$\gamma_A(\Delta\boldsymbol{\rho}, \tau) = \langle \tilde{\gamma}_A(\Delta\boldsymbol{\rho} + \mathbf{d}(t+\tau) - \mathbf{d}(t)) \rangle_t \,. \tag{3.11}$$

Assuming a linear motion $\mathbf{d}(t) = \mathbf{v}t$ with periodicity $\mathbf{d}(t) = \mathbf{d}(t+T)$, one obtains $\gamma_A(\Delta\rho, \tau) = e^{-(\Delta\rho^2 + (v\tau)^2)/2\rho_c^2}$. Thus the coherence time is given by the time required to move the diffuser out of its correlation area and the spatial coherence length is given by the speckle size. The residual coherence is limited on the diffuser side by its residual phase delay correlations $e^{-\sigma_\phi^2}$ and on the modulation side by the number of sampled uncorrelated areas $M = vT/s_c$ (2.19) determined by the periodicity T, thus $|\gamma_{A,\mathrm{res}}| = C \gtrsim 1/\sqrt{M} + e^{-\sigma_\phi^2}$.

Note that a Fresnel correlation propagation analysis allows the estimation of the near-field decorrelation time, which is obtained by replacing the speckle size x_c with the illumination beam size w [66].

Angled Incidence

Consider a Gaussian illuminating light field $a_{\mathrm{in}}(\boldsymbol{\rho})$ which temporally varies its angle of incidence, i.e. it introduces a linear phase gradient $a(\boldsymbol{\rho}, t) = e^{i(k_0 \sin(\boldsymbol{\theta}(t))\cdot\boldsymbol{\rho} + \phi(\boldsymbol{\rho})\cos\theta(t)} a_{\mathrm{in}}(\boldsymbol{\rho})$, where $\boldsymbol{\theta} = (\theta_x, \theta_y)$ is the angle from the optical axis (the sine function is interpreted vectorally) and the cosine term is added since the phase delay depends on the wavevector in propagation direction (sec. 3.1.2). Similarly as before, a static correlation function for the parameter $\boldsymbol{\theta}$ is constructed which, in the uncorrelated limit $r_c \to 0$, yields [58]

$$\tilde{\gamma}_A(\Delta\boldsymbol{\rho}, t_1, t_2) = e^{-\sigma_\phi^2(\cos\theta(t_1) - \cos\theta(t_2))} e^{-(kw/2)^2(\Delta\boldsymbol{\rho}/z + \sin\boldsymbol{\theta}(t_2) - \sin\boldsymbol{\theta}(t_1))^2/2}, \tag{3.12}$$

where the characteristic function describes a chromatic decorrelation due to to a shortened wavevector along the optical axis (the same effect is achieved by normal incidence with shorter wavelength). The spatially dependent exponential describes a translation of the whole speckle pattern in $\mathbf{e}_\theta$ direction. Note that due to its k dependence, a wavelength change additionally produces a similar but scaled speckle pattern.

For small angles $\theta \ll 1$ the characteristic function term is negligible and the sine

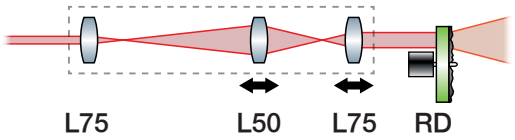

Figure 3.3: **Rotating diffuser setup.**
A variable magnification telescope prepares a collimated beam incident on a rotating diffuser (RD).

functions can be linearised $\sin\boldsymbol{\theta} \approx \boldsymbol{\theta}$. Then the duality between $\Delta\boldsymbol{\theta}$ and $\Delta\boldsymbol{\rho}/z$ becomes apparent. For uniform linear angular modulation $\boldsymbol{\theta}(t) = \boldsymbol{\Omega} t$ with modulation angular frequency Ω, one thus obtains the same result as for the moving diffuser, $\gamma_A(\Delta\rho, \tau) = e^{-(\Delta\rho^2+(\Omega\tau z)^2)/2\rho_c^2}$, where the residual coherence is limited by the phase delay distribution and sampled correlation areas $M = \Omega T z/s_c$, with modulation period T.

3.2 Setup

In this section the diffuser setups used to generate spatially incoherent light and speckle analysis methods are described.

The random diffusers studied here are of surface scattering type [58] and include ground-glass diffusers (DGs) and holographic diffusers (DHs). The random surface height fluctuations of DGs result from sand-blasting the non-polished side of a glass plate and are specified by the particle size (grit). The surface reliefs on DHs are produced by holographically recording a speckle pattern which is used to form the surface structure. They consist of polycarbonate and are directly specified by their FWHM divergence.

3.2.1 Rotating Diffuser

The spatially decorrelating moving diffuser is implemented as a rotating diffuser with the setup shown in fig. 3.3. For this, a hole is water-jet cut into the centre of a 50 mm diameter Thorlabs N-BK7 220 grit (DG220) diffuser and the diffuser is mounted onto a high rotational speed brushless motor.

The diffuser is illuminated by the 780 nm Toptica DL pro (NBL780) external cavity diode laser (ECDL), where the beam hits the diffuser near its edge, thus the effective diffuser motion is nearly linear with a speed of $v = 2\pi f R$, with rotation frequency f and radial beam position R. In order to vary the correlation lengths, the beam is first

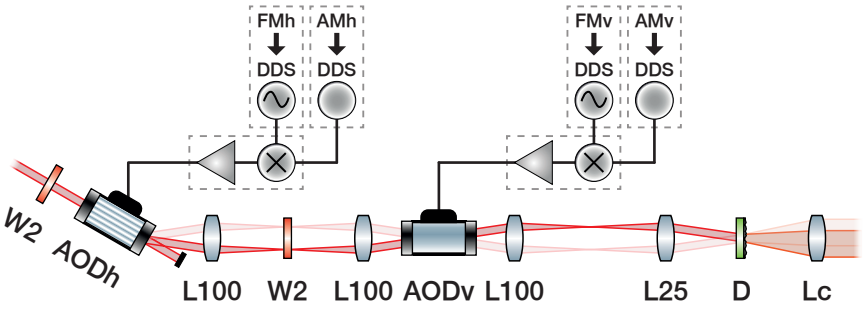

Figure 3.4: **Acousto-optic deflector setup.**
An incoming linearly polarized monochromatic beam is rotated into horizontal polarization by a half-waveplate (W2) to match the input polarization of a horizontally deflecting AOD (AODh). The Bragg diffracted beam is imaged into a vertically oriented AOD (AODv) with a 4f-imaging system where another half-waveplate (W2) again allows matching of the polarization. The vertically diffracted beam (not drawn) is imaged onto the diffuser (D) with another 4f-imaging system. The scattered light is collected by the final lens (Lc). To drive each AOD, a DDS generated, frequency modulated (FM) signal is mixed with an amplitude modulated (AM) envelope signal and is power amplified. FM leads to a varied Bragg diffraction angle (light red beam).

expanded by a telescope. A collimated incidence is used to keep the scattering angles low and fulfil the planar wavefront approximation.

3.2.2 Beam Deflection

Decorrelation by diversity of angular incidence is achieved with the setup shown in fig. 3.4. An AOD is used as angular modulator to the incoming 420 nm Toptica TA-SHG (NBL420) laser beam, and collimated illumination of the same spatial spot is realized using a 4f-imaging system. The diffusers used in this part are the holographic diffusers Edmund Optics 80° FWHM divergence (DH80) and Edmund Optics 15° FWHM divergence (DH15). Note that the figure shows two AODs and imaging systems to allow modulation in both spatial dimensions.

AODs rely on Bragg reflection at a travelling acoustic wave to deflect an incident laser beam by $\theta = 2\theta_B$ where the first-order Bragg angle is given by [67]

$$\sin\theta_B \approx \theta_B = \frac{\lambda}{2\Lambda_a} = \frac{\lambda}{2v_a} f, \tag{3.13}$$

with optical wavelength λ, acoustic wavelength Λ_a and acoustic frequency f. Modulation of the frequency thus allows scanning of the deflection angle. In contrast to acousto-optic modulators (AOMs) using longitudinal waves, AODs use more slowly propagating transversal shear modes in birefringent crystals [68] where the anisotropic acousto-optic interaction requires a specific linear polarization of the input light. Since acoustic waves have a finite velocity, modulation frequencies are limited by the acoustic propagation time necessary to pass the optical beam, i.e. $\tau_a(w) = w/v_a$ for a Gaussian beam with waist w.

In order to achieve fast and arbitrary frequency modulation (FM) signals, a direct digital synthesis (DDS) board [69] is used which can digitally generate the FM signal. The acoustic power dependence of the AOD diffraction efficiency is used to compensate for its deflection angle dependence. For this, a feed-forward scheme is implemented, in which another (synchronized) DDS produces an amplitude modulation (AM) envelope signal which is mixed with the FM signal.

The AOD model used is a Crystal Technology AODF 4120-3 using the shear mode of a TeO_2 crystal with acoustic velocity $v_a = 650\,\mathrm{m/s}$ at centre frequency $f_c = 120\,\mathrm{MHz}$ with nominal bandwidth $f_{\mathrm{BW}} = 50\,\mathrm{MHz}$ and aperture $D = 3\,\mathrm{mm}$. Using eq. (3.13) and taking the demagnification $M = 1/4$ of the imaging system into account, the deflection rate is $\theta/\Delta f = \lambda/v_a = 1.2\,\mathrm{mrad/MHz}$. Note that the decorrelation performance is independent of the demagnification since the increased angular incidence is cancelled by the reduced beam size. Still demagnification is chosen as the light collection efficiency depends on the product of beam width and divergence (sec. 2.1.3), and the scattering based divergence is larger than the modulation angles.

The 400 MHz bandwidth Analog Devices AD9910 DDS in a home-built reference implementation is used to generate the AM and FM signals, which are mixed and amplified by a home-built driver. Note that the reference implementation includes a high-pass filter at the output which is removed for the AM output as the modulation frequency is much smaller than the radio frequency (RF) carrier frequency.

3.2.3 Image Analysis

As the degree of coherence is directly related to the normalized intensity covariance (3.7), spatial coherence properties can be measured by recording different speckle intensity images on camera and performing image processing steps to deduce the quantities of interest. The speckle patterns are recorded with the AlliedVision Manta G-145B NIR charge-coupled device (CCD) camera.

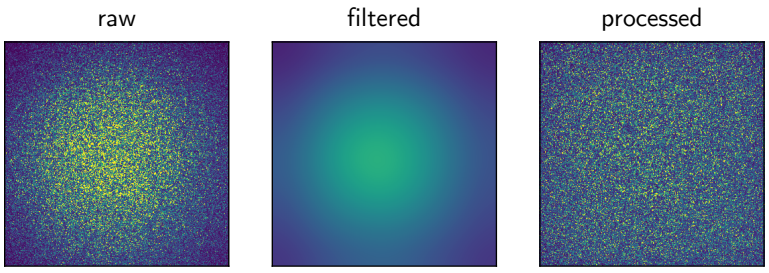

Figure 3.5: **Speckle pattern image processing.**
The directly recorded (raw) speckle pattern often has a non-uniform intensity envelope which can be estimated by applying a Gaussian filter. Normalizing the raw image with the filtered image yields the processed speckle pattern suitable for statistical speckle analysis.

In order to avoid speckle blurring due to finite-sized pixel areas, measurement distances are appropriately chosen to resolve a typical speckle by at least a 3x3 pixel array. Then the speckle contrast (sec. 3.1.1) deviation can be estimated to be already below 1 % [58].

Residual Coherence Estimation

Residual coherence properties can be obtained by their relation to speckle contrast (3.5) and involve measuring the first-order speckle statistics, namely the probability density distributions of intensity. Despite first-order statistics being technically defined for different realizations of speckle fields at a fixed observation position, the self-averaging property of speckles allows the measurement of the spatial intensity distribution of a single speckle pattern instead.

Imaging the whole speckle pattern creates the problem that the mean intensity is not uniform, such that the intensity distribution is superposed by the intensity envelope. To compensate this effect (fig. 3.5), each image is centred around its centroid and symmetrically resized. Imaging a large number of speckles ensures that speckle fluctuations appear in a much higher spatial frequency regime than the intensity envelope, thus a Gaussian filter with a smoothing radius much larger than the typical speckle size can be applied to suppress low frequency variations. The resulting image ("processed speckle pattern") is obtained by normalizing the raw image by the filtered image, from which the statistics can be taken.

For speckle contrast analysis, the mean and variance is directly determined from the raw data. A comparison value arises from least-squares fitting the gamma distribution (3.4) onto the probability density function. Then the effective number of incoherent

superpositions of fully developed speckle patterns can be extracted, which yields the contrast value.

Spatial Coherence Estimation

Since the (squared) modulus of the spatial coherence function is given by the static speckle intensity autocovariance function (3.7), it can be constructed from a single static speckle image. As the illuminating light spot has a Gaussian shape, the spatial coherence function is also expected to be Gaussian. Thus a 2D least-squares Gaussian fit with offset is performed on the processed speckle patterns, which yields the Gaussian intensity correlation length x_c (3.9).

Temporal Coherence Estimation

Temporal coherence can be estimated both statically and dynamically. As diffuser-based decorrelation mechanisms temporally modulate a speckle-defining parameter (e.g. diffuser displacement, sec. 3.1.3), a cross-correlation analysis with respect to this parameter can be performed, i.e. for varying parameters (or equivalently at different time steps) images of speckle patterns are recorded, and the correlation function between these processed speckle patterns is calculated. In the case of the moving diffuser, the diffuser is placed on a micrometre stage to capture speckle patterns at different lateral displacements. In the case of angled incidence, the patterns are measured for different fixed AOD RF frequencies.

To avoid the computationally expensive three-dimensional (3D) (two image and one parameter dimensions) correlation calculations, the images are sliced along the modulation axis and multiple slices with a spacing larger than the speckle size are selected. Each of these 2D slices is autocorrelated, then the results are averaged and fitted with a 2D tilted Gaussian.

Dynamically, the coherence time can be estimated by the decay of the speckle contrast (3.5), as it is determined by the number of uncorrelated parameter (or time) steps. For the rotating diffuser, this is achieved by varying the camera exposure time, and for the angled incidence, the angular modulation range is adjusted.

3.3 Static Speckles

In this section the static correlations of speckle patterns are measured, which determine coherence lengths and the intrinsic residual correlations of the diffuser.

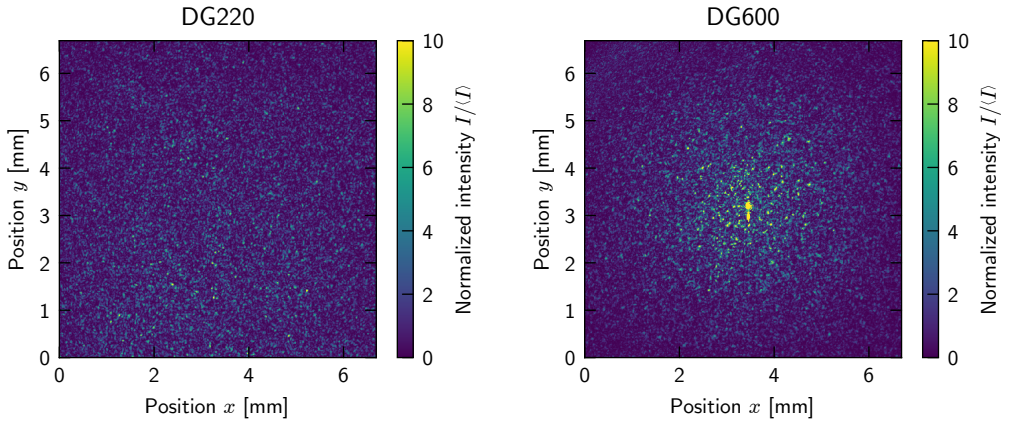

Figure 3.6: **Speckle patterns generated by ground-glass diffusers.**
Both images are recorded for the same illumination condition in the Fourier plane of a collection lens. While the diffuser ground by 220 grit particles (DG220) shows proper diffusion behaviour, a large power fraction is coherently transmitted through the 600 grit diffuser (DG600), rendering it unsuitable for coherence reduction.

Diffuser Types

Fig. 3.6 shows the speckle patterns of two ground-glass diffusers with different grain statistics at identical illumination conditions. The speckle sizes are similar, but whereas the coarser diffuser produces a homogeneous speckle pattern, the finer one retains a coherent, undiffracted beam. As argued in sec. 3.1.2, this results from a too smooth surface height (first-order) distribution, insufficiently randomizing the phase, making it unsuitable for coherence reduction. This can be attributed to the fabrication process where smaller sand grains fail to carve deep structures into the glass, despite surface height (second-order) correlations likely to be shorter than those of the coarser diffuser.

It is thus beneficial to use a holographic diffuser instead, as first-order fluctuations can be tuned independently from the second-order fluctuations, which allows for smaller scattering angles while still ensuring little residual correlations. This issue is in principle also solved by Lambertian opaque glass diffusers. However, due to volume scattering (multi-scattering within diffuser), its transmittance is low, resulting in power efficiencies of typically $\eta_{\text{opaque}} \sim 30\,\%$.

In contrast, the efficiencies of both the holographic DH15 diffuser $\eta_{\text{DH15}} \sim 95\,\%$ and the ground-glass DG220 diffuser $\eta_{\text{DG220}} \sim 75\,\%$ are measured to be significantly higher. The FWHM divergence of the DG220 is given by $\theta_{\text{DG220}} \sim 16°$.

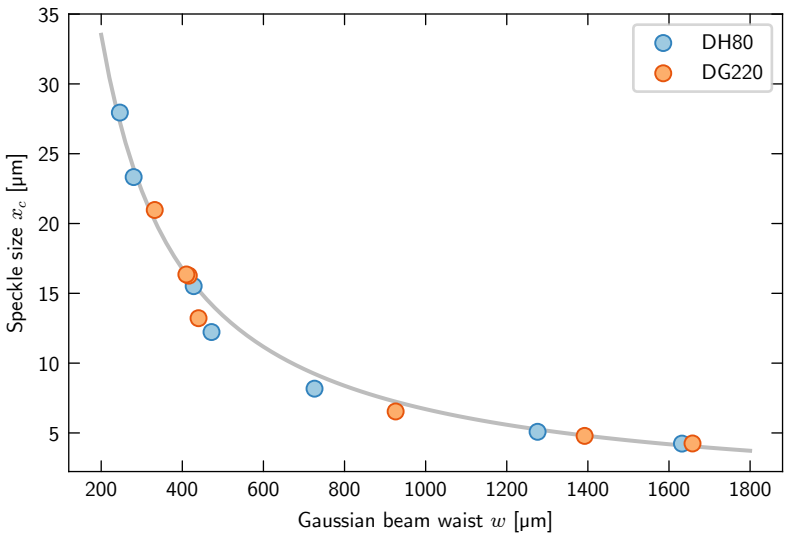

Figure 3.7: **Speckle size dependence on beam size.**
The speckle size x_c (3.9) depends inversely on the illuminating beam width w. In accordance with the van Cittert-Zernike theorem (3.8) plotted in grey, sufficiently random diffusers show the same correlation behaviour in Fourier plane (measured at a distance of $z = 30\,\text{mm}$ for the wavelength $\lambda = 780\,\text{nm}$), as verified by a 220 grit ground-glass diffuser (DG220) and a 80° FWHM divergence holographic diffuser (DH80).

Speckle Size Dependence On Illumination Area

In order to evaluate the speckle size dependence on the illumination area, the speckle size is measured for different incident beam sizes on various diffuser plates and plotted in fig. 3.7.

The speckle patterns are recorded in the Fourier plane of a $f = 30\,\text{mm}$ lens with a numerical aperture chosen not to cut off the Gaussian intensity envelope. This ensures high collection efficiency and speckle sizes should only depend on illumination conditions and not on any imaging optics. Applying eq. (3.6) agrees well with the data. Since the correlation length determines the coherence length when modulating the diffuser to obtain incoherent light, this indicates that the illumination area provides control over the required spatial coherence length.

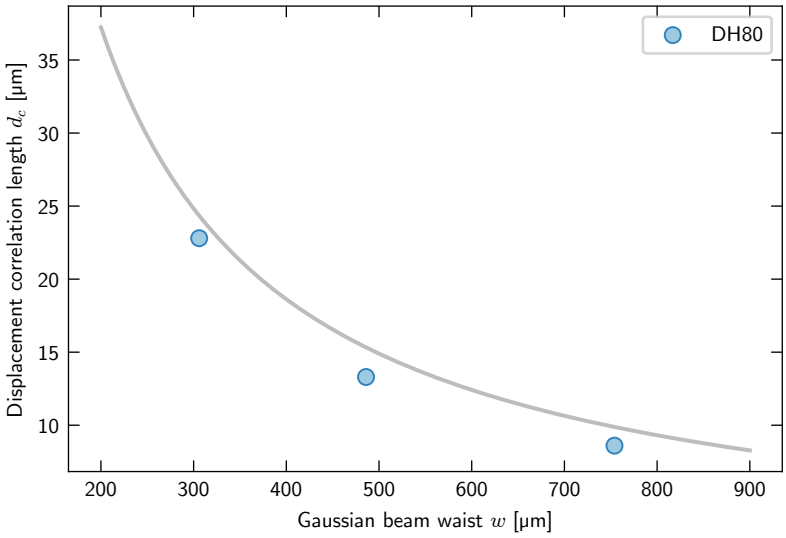

Figure 3.8: **Displacement correlation length dependence on beam width.** The Gaussian displacement correlation length d_c (proportional to coherence time) falls off inversely with illuminating beam width w, similar as the spatial speckle correlation function, indicating a translational shift of the speckle pattern as main decorrelation mechanism. The data is measured for the 80° FWHM divergence holographic diffuser (DH80) at a distance of $z = 30\,\mathrm{mm}$ from the diffuser without lens.

3.4 Modulation by Diffuser Rotation

The first implementation of coherence reduction uses a rotating diffuser (sec. 3.2.1) to integrate a series of speckle patterns. The coherence properties of the resulting light field is described in this section.

Temporal Coherence

In order to obtain the short-term decorrelation characteristics, i.e. the coherence time, a static speckle pattern cross-correlation analysis (sec. 3.2.3) is performed, with the horizontal (transversal) displacement of the DH80 diffuser as parameter. By fitting a Gaussian along this displacement correlation function, one obtains a correlation length d_c which can be associated with a correlation time $t_c = d_c/v$ for linear motion.

Fig. 3.8 thus effectively shows the decrease of the temporal coherence length and agrees with the expected curve. Deviations are likely introduced by finite displacement precision resulting in limited resolution and thus an uncertain Gaussian fit. Since the

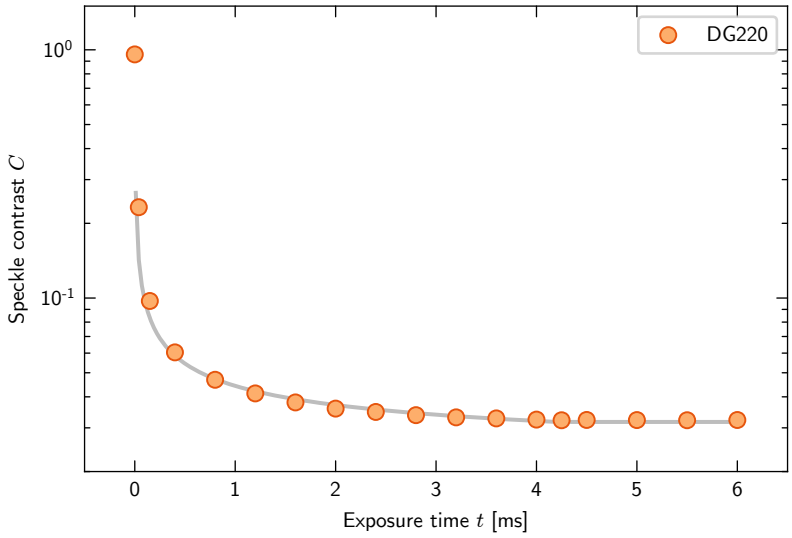

Figure 3.9: **Residual coherence convergence of rotating diffuser.** The logarithmic plot shows the speckle contrast (i.e. the residual coherence) decrease when averaging over increasing numbers of uncorrelated speckle patterns. The data is obtained for a 220 grit ground-glass diffuser (DG220) rotating with a period of $T = 4.2\,\mathrm{ms}$ where the contrast decrease ceases. The speckle size is measured as $x_c = 18\,\mu\mathrm{m}$, recorded at a distance of $z = 55\,\mathrm{mm}$.

displacement correlation length behaves identically as the spatial correlation length, particularly having a z-position dependent scaling (3.9), decorrelation performance varies upon the position of the diffraction plane.

Residual Coherence

The capabilities of the rotating diffuser approach to reduce residual coherence are tested with a motor rotation period of $T = 4.2\,\mathrm{ms}$ and an outer radial position of the illuminating spot at $R = 20\,\mathrm{mm}$ maximizing the diffuser velocity $v = 2\pi R/T \sim 30\,\mathrm{m/s}$. To estimate the expected decorrelation time t_c, the static speckle size is measured as $x_c = 18\,\mu\mathrm{m} \sim vt_c$. The observation distance of $z = 55\,\mathrm{mm}$ from the diffuser is deduced from static measurements using the linear relation between distance and speckle size. The number of mutually uncorrelated modes (2.20) is thus $M \sim 84^2$.

Fig. 3.9 shows an initially fully developed speckle contrast which decreases for longer exposure times since more uncorrelated areas are averaged, limited due to the rotational periodicity to $C_{\mathrm{min}} \sim 0.033$ giving a coherence time of $\tau_c \sim 4.3\,\mu\mathrm{s}$. The data agrees with

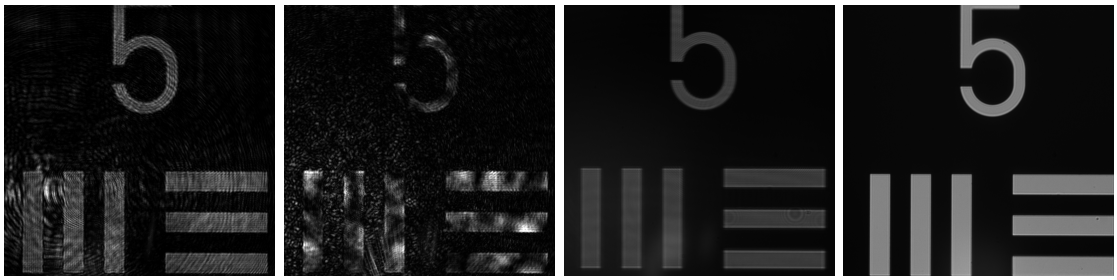

Figure 3.10: **USAF resolution target imaged with different light sources.** The images with a bar line width of 15 µm are recorded under illumination with a narrowband laser, a static speckle pattern, rotating diffuser light and an light-emitting diode (LED) (left to right). The coherent noise generated by the dirty imaging optics is clearly reduced when using the rotating diffuser light in comparison to the coherent laser.

the model, where the decrease rate is obtained from above estimation and a constant offset $C_0 = 0.02$ is fitted to account for coherent transmission through the diffuser.

Intensity Noise

Since the temporal coherence function is determined by the spatial correlation function of the random speckle field (sec. 3.1.3), the Siegert relation (2.16) can be used to derive its intrinsic intensity noise spectrum yielding a theoretical RIN of $s_I(\omega) = \sqrt{2\pi} x_c e^{-x_c^2\omega^2/2v^2}/v$. In the low frequency limit using the parameters from the previous section this results in $s_I \sim -60\,\mathrm{dBc/Hz}$, thus performing much worse compared to free-running lasers.

Global (total beam width) intensity noise measurements show that the fast spinning motor furthermore introduces strong vibrations due to an unbalanced diffuser plate (off-axis mounting hole with excessive tolerances) leading to diffuser plate tilting. This modulates the light intensity in the rotation frequency regime at a magnitude of up to $-15\,\mathrm{dBc/Hz}$, thus requiring multi-period averaging.

Imaging

In order to qualitatively demonstrate coherent noise reduction of spatially incoherent light, images of a resolution test target are recorded with different focused light sources through a dirty microscope objective (fig. 3.10). The target is back-illuminated by a coherent laser, a static speckle pattern, a rotating diffuser and a LED, serving as optimal, incoherent reference. Whereas the coherent laser produces fine interference rings that

lead into the dark area, the incoherent LED does not produce any coherent artefacts. The same is valid for the light produced by the rotating diffuser where the large scale interferences are blurred and thus do not contribute to noise. The remaining stripes originate from the finite illumination contrast and are a consequence of the diffuser motion.

Conclusion

Rotating diffusers present a method to generate partially coherent, pseudo-thermal light with tunable coherence properties. Precision-manufactured diffuser-motor combinations could in principle also overcome currently present vibration issues.

However, decorrelation times are limited by the rotation speed of the (already fast-spinning) motor. Considering that, when increasing the rotation frequency by an order of magnitude, the diffuser already moves near sonic speed renders the moving diffuser approach impractical for high-speed incoherent light generation.

3.5 Modulation by Angular Incidence

In order to overcome temporal averaging limitations due to the physical motion of the diffuser, an angled incidence approach (sec. 3.1.3) is suitable as in this case only the beam itself has to be modulated.

The deflection scheme is thus required to provide fast modulation of a large angular deflection bandwidth. For this an AOD is tested with which the beam deflection can be realized much faster than with mechanical means like micro-electro-mechanical systems (MEMS).

One-Dimensional Angular Scan

To verify the picture that the angular decorrelation of speckle patterns in a Fraunhofer plane mainly originates from pattern translation (sec. 3.1.3), a cross-correlation analysis with one-dimensional (1D) varying angles of incidence is performed, confirming the model (similar to fig. 3.8).

For a residual coherence measurement, the AOD is linearly frequency modulated at $f_{\mathrm{FM}} = 10\,\mathrm{kHz}$. Since for fast modulation the camera exposure time is too long to observe coherence reduction on different time scales, the fact that the modulation is periodic is used to instead vary the scanning frequency range while keeping the exposure time at its multiple $t_{\mathrm{exp}} = 10/f_{\mathrm{FM}}$.

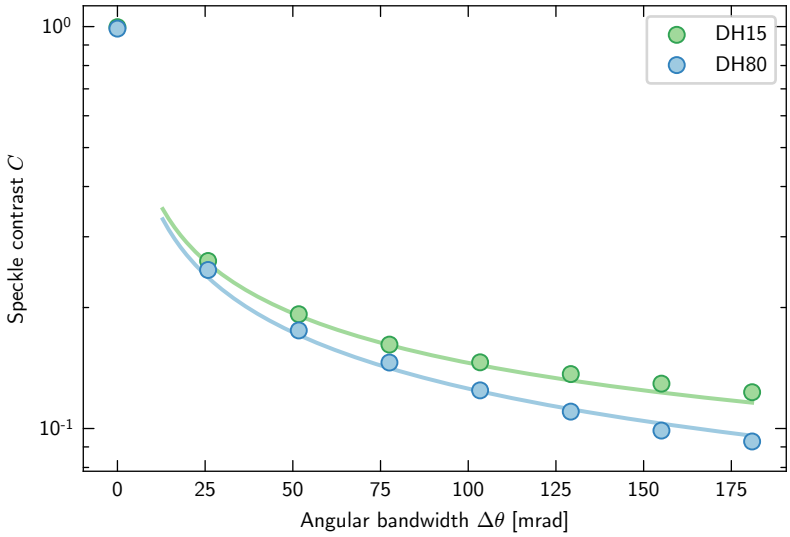

Figure 3.11: **Residual coherence convergence due to angular diversity.** The logarithmic plot shows the speckle contrast due to AOD-based angular incidence modulation at $f_{\mathrm{FM}} = 10\,\mathrm{kHz}$ for holographic diffusers with 15° (DH15) and 80° (DH80) FWHM divergence. Since a larger angular modulation bandwidth comes with averaging over more uncorrelated speckle patterns, the contrast decreases, in accordance with the translational pattern shifting model obtained for a speckle size of $x_c = 40\,\mu\mathrm{m}$ in the Fourier plane of a $f = 75\,\mathrm{mm}$ lens (solid lines).

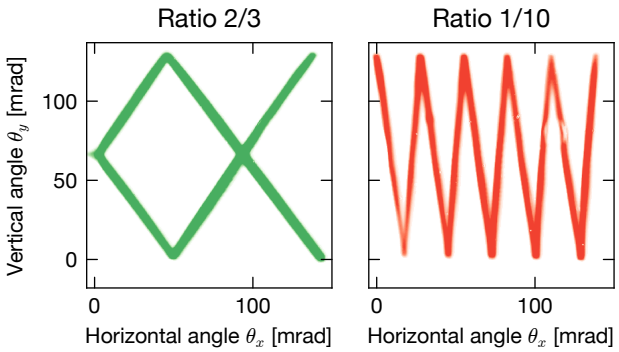

Figure 3.12: **Image of the two-dimensional angular scanning pattern.** The plots show beam images recorded without the diffuser (thus the incidence angle is mapped to the spatial position of the camera sensor) with sufficiently long exposure times to trace the scan pattern with a ratio r_x/r_y between horizontal and vertical FM frequency. Variations in intensity result from inhomogeneous AOD diffraction efficiencies at different input angles and variations in the angular bandwidth are a consequence of astigmatism due to relative positioning errors of AODs and diffuser.

Fig. 3.11 is obtained for a static speckle size of $x_c = 40\,\mu\text{m}$ in the Fourier plane of a $f = 75\,\text{mm}$ lens for two holographic diffusers. The number of mutually uncorrelated modes (2.20) for the DH15 (DH80) diffuser is thus $M \sim 48^2$ ($M \sim 308^2$). Again the decorrelation with modulation bandwidth follows the predicted reduction rate, where the discrepancy between the diffusers results from the coherent transmission part and is fitted to $C_0 = 0.01$ ($C_0 = 0.03$). The achievable minimal speckle contrasts at $C \sim 0.1$ show that the small deflection ranges of AODs (compared to mechanical deflectors) severely limit the number of averaged uncorrelated speckle patterns.

Two-Dimensional Angular Scan

An effectively larger angular bandwidth $\Delta\theta$ is obtained using a second, perpendicularly deflecting AOD allowing incidence from a solid angle, i.e. the number of decorrelated patterns determining the residual coherence becomes $1/C^2 \propto \theta_c/\Delta\theta \to (\theta_c/\Delta\theta)^2$ with the linear decorrelation angle θ_c (sec. 3.1.3). However, since the solid angle has to be rasterised the required linear modulation speed would also have to increase by the same factor.

Therefore instead a Lissajous curve is modulated where the AOD signal of each dimension i is linearly swept up and down with frequency $f_{i,\text{FM}} = r_i f_{\text{FM}}$ (fig. 3.12)

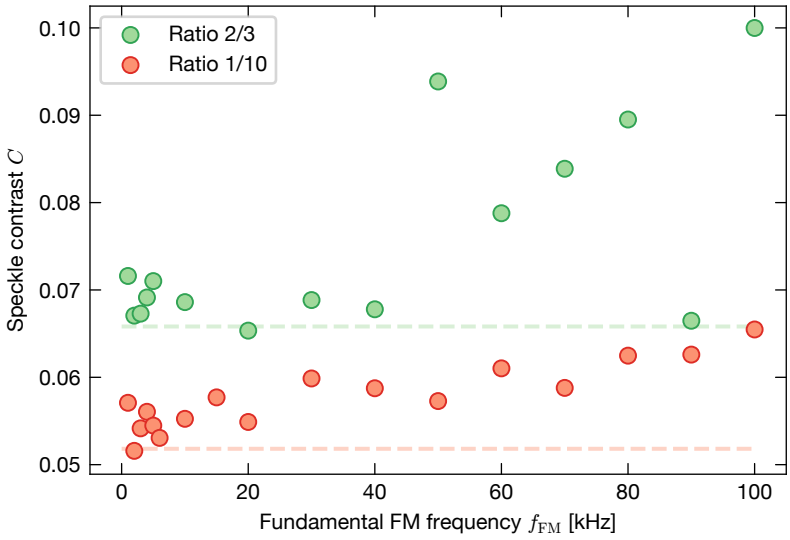

Figure 3.13: **Residual coherence dependence on modulation speed.** The speckle contrast (i.e. the residual coherence) increases when the FM frequency approaches the AOD response time of $1/\tau \sim 450\,\mathrm{kHz}$ in either deflection direction (modulation speed ratio r_x/r_y). The solid line shows the expected contrast for the DH15 diffuser without taking into account modulation speeds, measured for a speckle size of $x_c = 40\,\mu\mathrm{m}$ in the Fourier plane of a $f = 75\,\mathrm{mm}$ lens.

where f_{FM} is the fundamental (2D) modulation frequency and r_i is the corresponding multiple. In the linearised version of eq. (3.12) the 2D incidence angle is given by $\theta = \sqrt{\theta_x^2 + \theta_y^2}$, thus a geometric consideration yields an effective AOD FM bandwidth of $f_{\mathrm{FM,\,eff}} = 2 f_{\mathrm{FM}} \sqrt{r_x^2 + r_y^2}$. The factor of two is introduced to include the up- and down-ramp when there is a finite phase between the horizontal and vertical modulation.

Fig. 3.13 shows how the speckle contrast evolves when the FM speed is increased, measured with the DH15 and the same illumination conditions as in fig. 3.11. The camera exposure time is chosen to match the fundamental frequency. In the lower kHz regime the contrast behaves as expected, where the model takes into account the previously estimated offset correlation $C_0 = 0.03$ and the reduced vertical scan range (fig. 3.12). For the scan frequency ratio 2/3 the contrast strongly increases from $f_{\mathrm{FM}} \gtrsim 50\,\mathrm{kHz}$, whereas in the 1/10 case a slower increase is visible starting already around $f_{\mathrm{FM}} \sim 10\,\mathrm{kHz}$.

The increase can be attributed to the finite response time of the AOD determined by the finite travelling time of the acoustic wave crossing the beam $\tau = w/v_a \sim 2.2\,\mu\mathrm{s}$.

At these time scales the beam is not continuously deflected but rather simultaneously deflected resulting in simultaneous illumination of the diffuser from a range of angles reducing the speckle suppression capabilities. For the same fundamental frequency the vertical modulation of the ratio 1/10 case reaches this regime earlier than in the 2/3 case, thus its increase begins first. As the horizontal scan is slower in the 1/10 case, the contrast increases more slowly.

Intensity Noise and Efficiency

An intensity noise estimation in analogy to the rotating diffuser approach (sec. 3.4) gives a theoretical intensity noise value of $S_\epsilon \sim -90\,\mathrm{dBc/Hz}$ in the low-frequency limit for an effective modulation speed of $f_{\mathrm{FM,\,eff}} = 100\,\mathrm{kHz}$.

While using the AOD in one dimension resulted in diffraction efficiencies of $\eta_{\mathrm{AOD}} \sim 65\,\%$ across the deflection bandwidth (specification: $\eta_{\mathrm{AOD}} \gtrsim 75\,\%$), tilted incidence into the second, orthogonal AOD strongly reduced diffraction efficiency, giving a combined power efficiency below $\eta \sim 20\,\%$. Accounting for feed-forward stabilization losses and the finite NA of the collection lens after the diffuser resulted in an overall light utilization of only $\eta \sim 10\,\%$. Note that a light collection cutoff at the intensity FWHM of a Gaussian results in a collection efficiency of $\eta_{\mathrm{FWHM}} = 50\,\%$, such that the theoretical maximum is $\eta \sim \eta_{\mathrm{AOD}}^2 \eta_{\mathrm{FWHM}} \sim 28\,\%$.

Conclusion

As a diffuser-based coherence reduction approach, the light generated by AOD-scanned angular diffuser incidence has similar properties as the one from the rotating diffuser approach.

In comparison, significantly higher modulation speeds in the $10^5\,\mathrm{Hz}$ regime can be achieved. This comes at the expense that less independent speckle patterns can be averaged (i.e. higher residual coherence) since the deflection ranges of AODs are limited, and that light utilization is reduced.

If power efficiency and low temporal intensity noise is not the main concern and quasi-monochromatic light is required, this approach can be used for spatial coherence reduction. However, for tight optical confinement of atoms, trapping frequencies easily reach the achievable modulation frequency, requiring yet another coherence reduction approach.

4 Fibre-Controlled Decoherence

Active modulation techniques reducing spatial coherence in a light field rely on deterministically shaping the wavefront of a possibly coherent beam in such a way that spatial correlations are minimized. Despite having in principle full control over the decoherence properties, this approach is limited by the speed of the available modulation techniques. Since the characteristic times for spatial decoherence are determined by the coherence time (2.19), an opposite approach is to start from an intrinsically fast fluctuating light field. Applying dispersive spatiotemporal coupling allows the conversion of incoherence in the time domain into incoherence in the spatial domain. If an application does not require quasi-monochromaticity, broadband light sources enable essentially arbitrarily fast decoherence.

In sec. 4.1 the coherence properties of optical fibres are derived in scalar wave theory, particularly taking into account the effects of different core geometries. The experimental setup is shown in sec. 4.2, which includes a description of the studied light sources and the interferometric coherence measurement approach. In the subsequent sections the results for temporal coherence (sec. 4.3), spatial coherence (sec. 4.4) and intensity noise (sec. 4.5) can be found.

Coherence Conversion in Multimode Fibres

The idea behind temporal coherence conversion is to induce a spatially dependent propagation time delay. If the relative delay between two such propagation modes exceeds the coherence time of the light source, they mutually dephase which leads to coherence reduction. Since the modes correspond to distinct positions in transverse space, the modal decoherence also translates into spatial decoherence.

Multimode fibres are optical fibres with large core sizes with respect to the transmitted wavelength, such that they can carry many distinct spatial modes with varying propagation speeds. This phenomenon of modal dispersion can be intuitively understood by applying a ray optics picture drawn in fig. 4.1. If the light beam incident on the fibre is divergent, it consists of rays propagating at various angles. As rays with higher incidence angle travel a longer optical path, their propagation time is longer which leads

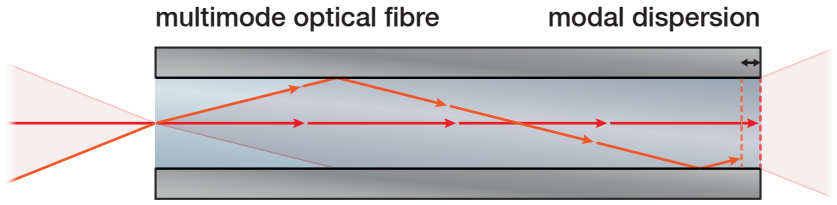

Figure 4.1: **Coherence conversion in multimode fibres.**
Light rays travelling with larger angles of incidence cover a longer optical path, therefore their longitudinal propagation speed is reduced. If their differential time delay after transmission through the fibre exceeds the temporal coherence time of the incoupled light, the field becomes decorrelated and the output face of the fibre behaves as a spatially incoherent light source.

to the desired differential time delay. When using broadband light sources, additionally chromatic dispersion effects arise. Its main contribution is material dispersion due to the fibre core material and has a waveguide dispersion correction due to evanescent waves travelling in the optically thinner fibre cladding. As typical multimode fibres use silica as material (which has low dispersion) and large cores confine the light within the core, modal dispersion is by far the dominant effect in step-index fibres.

4.1 Theory

In this section the influence of multimode optical fibres on the temporal and spatial coherence properties of an incoupled broadband light beam is derived, showing coherence reduction.

Fibre Propagation

Neglecting bendings and imperfections, optical fibres can be regarded as longitudinally invariant waveguides with refraction index $n(\boldsymbol{\rho}, \omega)$ where $\boldsymbol{\rho} = (x, y)$ is the transversal, z is the longitudinal position, and ω is the angular frequency of the light field. Applying a separation of variables ansatz of the light field $\tilde{A}(\mathbf{r}, \omega) = A(\boldsymbol{\rho})A_z(z)\mathcal{A}(\omega)$ on the Helmholtz equation (2.2) decouples the longitudinal term into a harmonic oscillator with longitudinal propagation constant β and a transversal Helmholtz equation [67]

$$\nabla_\rho^2 A(\boldsymbol{\rho}) + (k^2(\boldsymbol{\rho}, \omega) - \beta^2(\omega))A(\boldsymbol{\rho}) = 0, \tag{4.1}$$

with local wavenumber $k(\boldsymbol{\rho},\omega) = n(\boldsymbol{\rho},\omega)k_0(\omega)$ and vacuum wavenumber $k_0(\omega) = \omega/c$. This eigenvalue equation describes the propagation of transversal fields, which has a finite number of solutions ("propagation modes" $|m\rangle$ with eigenvalue k_m and field profiles $\psi_m(\boldsymbol{\rho}) = \langle\boldsymbol{\rho}|m\rangle$) since only guided (i.e. totally internally reflected) modes are considered.

Because the longitudinal propagation speeds are of main interest, the propagation wavenumber

$$\beta_m^2(\omega) = k^2(\omega) - k_m^2(\omega) \tag{4.2}$$

is considered as a dependent variable and yields the dispersion relation. The explicit dependence on m describes modal dispersion, and chromatic dispersion is identified as material dispersion $n(\omega)$ and waveguide dispersion $k_m(\omega)$.

The propagation function h_L (2.4), relating an incident field $a(\boldsymbol{\rho})$ at $z = 0$ with the propagated field $A(\boldsymbol{\rho})$ at the fibre output $z = L$, can thus be expanded in terms of the propagation modes as

$$A(\boldsymbol{\rho},\omega) = \sum_m \langle m|a\rangle\, \psi_m(\boldsymbol{\rho}) e^{-i\beta_m(\omega)L}, \tag{4.3}$$

where $\langle m|a\rangle = \int \psi_m^*(\boldsymbol{\rho})a(\boldsymbol{\rho})d^2\rho$ denotes the input field overlap integral.

Assuming the field to be initially spatially coherent, one can factorize its spatial and temporal part as $a(\boldsymbol{\rho},t) = a(\boldsymbol{\rho})a_t(t)$ such that the space-time correlation function (2.10) becomes $\Gamma_a(\boldsymbol{\rho}_1,\boldsymbol{\rho}_2,\tau) = \langle a^*(\boldsymbol{\rho}_1)a(\boldsymbol{\rho}_2)\rangle \langle a_t^*(t)a_t(t+\tau)\rangle$. Inserting the mode expansion yields the output correlation function

$$\Gamma_A(\boldsymbol{\rho}_1,\boldsymbol{\rho}_2,\tau) = \int \frac{d\omega}{2\pi} e^{i\omega\tau} s_a(\omega) \sum_{m,n} \langle a|m\rangle \langle n|a\rangle\, \psi_m^*(\boldsymbol{\rho}_1,\omega)\psi_n(\boldsymbol{\rho}_2,\omega) e^{i(\beta_m(\omega)-\beta_n(\omega))L}, \tag{4.4}$$

where $s_a(\omega)$ is the normalized (statistical) optical power spectral density (2.13).

If the relative spectral bandwidth (2.14) is small, $\Delta\nu \ll \nu$, and the fibre is highly multimode (as studied here), one can approximate the mode profiles as spectrally independent $\psi_m(\boldsymbol{\rho},\omega) \approx \psi_m(\boldsymbol{\rho})$. Note that a similar derivation can be found in [70].

Spatial Coherence Function

In order to determine spatial coherence, consider the equal-time correlation function at the fibre output, $\Gamma_A(\boldsymbol{\rho}_1,\boldsymbol{\rho}_2) = \Gamma_A(\boldsymbol{\rho}_1,\boldsymbol{\rho}_2,\tau = 0)$, with which the intuitive picture of decorrelating propagating light rays can be formalized.

In the limit of vanishing modal dispersion, $k_m = k_n$, the phase evolution in eq. (4.4)

cancels and the frequency integral evaluates to unity, indicating no coherence reduction, $\gamma_A(\boldsymbol{\rho}_1, \boldsymbol{\rho}_2) = 1$. This corresponds to common cases like free propagation in homogeneous media or single-mode fibres.

In the opposite case of vanishing chromatic dispersion, modal dispersion remains the only effect. For a spectrum centred at frequency ω_0 the dispersion relation (4.2) can be expanded as $\beta_m(\omega) \approx \beta_m(\omega_0) + (\omega - \omega_0)/v_m(\omega_0)$, where the group velocity

$$v_m(\omega_0) = \frac{c}{n}\frac{\beta_m(\omega_0)}{k(\omega_0)} = \frac{c}{n}\sqrt{1 - \frac{k_m^2}{k^2(\omega_0)}} \tag{4.5}$$

is identified. The frequency dependent part of the exponent in the correlation function (4.4) thus reduces to $\omega\Delta t_{mn}$, with relative modal time delays $\Delta t_{mn} = L/v_m - L/v_n$. Then the frequency integral Fourier transforms the optical spectral density into the initial temporal coherence function γ_a (2.13), such that the spatial correlation function becomes [70]

$$\Gamma_A(\boldsymbol{\rho_1}, \boldsymbol{\rho_2}) = \sum_{m,n} \psi_m^*(\boldsymbol{\rho}_1)\psi_n(\boldsymbol{\rho}_2)\,\langle a|m\rangle\,\langle n|a\rangle\,\gamma_a(\Delta t_{mn})e^{i(\Delta\beta_{mn}(\omega_0)L - \omega_0\Delta t_{mn})}, \tag{4.6}$$

with propagation constant difference $\Delta\beta_{mn}(\omega) = \beta_m(\omega) - \beta_n(\omega)$.

This equation can be understood by first considering one position on the fibre output face, $\boldsymbol{\rho}_1$, illuminated by only a single mode. Let a second point $\boldsymbol{\rho}_2$ be equally illuminated by a multitude of modes, $\psi_n(\boldsymbol{\rho}_2) = 1/\sqrt{M}$, where the weight of each mode is given by its occupation, i.e. the overlap $\langle n|a\rangle$. The total mutual coherence between the two points is then given by the mutual coherence of each mode, weighted by its occupation. Since each mode is a time-delayed copy of each other, the coherence in question is the original temporal coherence. In order to allow the field at $\boldsymbol{\rho}_2$ to have a non-equal mode composition, the overlap $\psi_n(\boldsymbol{\rho}_2)$ is introduced, which weights the effect of each mode. By also allowing arbitrary mode compositions for $\boldsymbol{\rho}_1$, one finally obtains eq. (4.6).

Residual Spatial Coherence

In order to estimate the degree of coherence without knowledge of the mode structure, the average over all pairs of points in the output plane is considered. Since no specific correlations at the output plane are assumed, the overlaps $\psi_m(\boldsymbol{\rho})$ can be seen as independent identically distributed random variables (i.e. they have common statistics and are uncorrelated with respect to mode m and position $\boldsymbol{\rho}$), such that their cross-correlation factorizes $\langle\psi_m^*(\boldsymbol{\rho}_1)\psi_{n\neq m}(\boldsymbol{\rho}_2)\rangle = \langle\psi_m^*(\boldsymbol{\rho}_1)\rangle\,\langle\psi_{n\neq m}(\boldsymbol{\rho}_2)\rangle$.

Furthermore note that the mode decompositions ψ_m are normalized by definition, thus the average mode occupation is $\left\langle |\psi_m|^2 \right\rangle = 1/M$, where M is the number of fibre modes. As expectation values of phase-uniformly distributed complex numbers vanish, $\langle \psi \rangle = 0$, the complex spatial correlation function also vanishes, $\langle \Gamma_A(\boldsymbol{\rho}_1, \boldsymbol{\rho}_2) \rangle = 0$. Its modulus however is finite but not linear in the cross-correlation terms. Instead its upper bound given by Jensen's inequality [71] $\langle |\Gamma_A| \rangle \leq \sqrt{\langle |\Gamma_A|^2 \rangle}$ is evaluated, which involves calculating a four-point expectation value. Assuming Gaussian statistics, Reed's theorem [65] can be applied to obtain $\langle \psi_m^* \psi_n \psi_k^* \psi_l \rangle = \left\langle |\psi_m|^2 \right\rangle \left\langle |\psi_n|^2 \right\rangle \delta_{mk} \delta_{nl}$, such that the residual correlation (2.19) becomes

$$|\Gamma_{A,\mathrm{res}}|^2 \equiv \left\langle |\Gamma_A(\boldsymbol{\rho}_1, \boldsymbol{\rho}_2)|^2 \right\rangle = \frac{1}{M^2} \sum_{m,n=1}^{M} |\langle m|a \rangle|^2 |\langle n|a \rangle|^2 |\gamma_a(\Delta t_{mn})|^2, \tag{4.7}$$

where $|\langle m|a \rangle|^2$ describes the occupation of mode m. With the expected value of the intensity $\langle I_A(\boldsymbol{\rho}) \rangle = \sum_{m=1}^{M} |\langle m|a \rangle|^2 / M$, one can define the residual spatial degree of coherence $|\gamma_{A,\mathrm{res}}| = |\Gamma_{A,\mathrm{res}}| / \langle I_A \rangle$.

Eq. (4.7) reproduces the idea (sec. 4) that mutually time-delayed modes Δt_{mn} dephase according to the decaying temporal coherence function $|\gamma_a|$. As the whole occupation correlation matrix is summed in the formula, best coherence reduction is achieved by exciting modes which maximize the mean differential mode delays. Under the requirement of a large number of excited modes, homogeneous fibre launch conditions (exciting modes of different group velocities equally) are therefore favoured.

Instead of summing the discrete modes, it is often convenient to express them in terms of their time delays Δt_m. Transforming into a time-delay distribution $p(\Delta t)$ thus yields

$$|\gamma_{A,\mathrm{res}}|^2 = \iint p(\Delta t_1) p(\Delta t_2) |\gamma_a(\Delta t_1 - \Delta t_2)|^2 d\Delta t_1 d\Delta t_2. \tag{4.8}$$

Note that p has the properties of a probability density function to ensure normalization.

Spatial Coherence Function in Incoherent Limit

As in the previous section the output positions are averaged, no statement can be made about the shape of the spatial coherence function. If again no assumptions on the mode structures are made, one can provide a simple estimate due to [72] in the fully incoherent limit.

Consider the central point in the plane of interest and let it be incoherently and uniformly illuminated with light incident up to an angle α. In free space propagation,

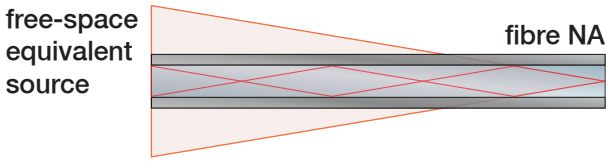

Figure 4.2: **Fibre equivalent of the van Cittert-Zernike theorem.** The guiding condition of the optical fibre, i.e. its numerical aperture (NA), limits the angular spread of light illuminating a point at the fibre end face (on the right hand side). By extrapolating this angle, one can identify an equivalent free-space source, to which the van Cittert-Zernike theorem (2.22) can be applied to obtain the spatial coherence function.

one can identify the incoming light with an incoherent source filling the corresponding solid angle (fig. 4.2), such that the van Cittert-Zernike theorem (2.22) gives the spatial coherence function. Since in the case of a fibre the angle is limited by the guiding condition, one can replace $\tan\alpha \approx \mathrm{NA}$ to obtain

$$\gamma_A(\Delta\rho) \approx 2\frac{J_1(k_0\Delta\rho\mathrm{NA})}{k_0\Delta\rho\mathrm{NA}} \tag{4.9}$$

for a circular light source with vacuum wavenumber k_0, the NA of the fibre and a radial displacement $\Delta\rho$. Integration of eq. (2.12) yields a coherence length of $s_c = 32/3\pi k_0\mathrm{NA}$.

Temporal Coherence

For determining temporal coherence, consider the equal-space correlation function at the fibre output, $\Gamma_A(\tau) = \Gamma_A(\boldsymbol{\rho}, \boldsymbol{\rho}, \tau)$.

Consider again the two cases discussed before. For vanishing modal dispersion the spatial terms lose frequency dependence, thus the temporal coherence function remains invariant $\gamma_A(\tau) = \gamma_a(\tau)$. For vanishing chromatic dispersion and linear modal dispersion, the correlation function yields

$$\Gamma_A(\tau) = \sum_{m,n} \langle a|m\rangle \langle n|a\rangle \psi_m^*(\boldsymbol{\rho})\psi_n(\boldsymbol{\rho})\gamma_a(\tau + \Delta t_{mn})e^{i(\Delta\beta_{mn}(\omega_0)L - \omega_0\Delta t_{mn})}, \tag{4.10}$$

with symbols as defined for eq. (4.6).

Using the same statistical assumptions as the ones used to derive the residual coherence, especially $\langle\psi_m^*\psi_n\rangle = \delta_{mn}/M$, the averaged temporal coherence function also reduces to the input function $\langle\gamma_A(\tau)\rangle = \gamma_a(\tau)$, so on average the temporal characteristics of the light source do not change.

4.1.1 Step-Index Fibres

Step-index optical fibres consist of a light-guiding core with homogeneous refractive index n_1 and size a, surrounded by a cladding with homogeneous but optically less dense refractive index n_2, which allows for total internal refraction. The cladding is chosen thick enough to fully confine the evanescent waves of the guided modes. From the condition for total internal reflection, the fibre numerical aperture is defined as $\mathrm{NA} = \sqrt{n_1^2 - n_2^2}$.

For the typically small values $\mathrm{NA} \ll 1$, the fibre is in the weak guiding regime, i.e. it obeys the paraxial approximation and the treatment in sec. 4.1 is applicable. The polarization-degenerate solutions of the transversal Helmholtz equation (4.1) are accordingly called linear polarized (LP) modes.

Round Core

For round-core step-index fibres with core radius a, cylindrical symmetry suggests a separation ansatz decoupling the azimuthal dimension φ from the radial one ρ. The propagation solutions are thus given by $A(\mathbf{r}) = A_\rho(\rho)e^{-il\varphi}e^{-i\beta z}$ with azimuthal mode number (and eigenvalue) l. The radial mode profile is given by [67]

$$A_\rho(\rho) \propto \begin{cases} J_l(k_{lm}\rho) & \rho \leq a \\ K_l(\kappa_{lm}\rho) & \rho > a \end{cases} \tag{4.11}$$

with the core-cladding relation $\mathrm{NA}^2 k_0^2 = k_{lm}^2 + \kappa_{lm}^2$, the lth Bessel function of the first kind J_l, the lth modified Bessel function of the second kind K_l and the radial mode number m with transversal eigenvalue k_{lm}. The boundary conditions lead to the characteristic equation

$$k_{lm}\frac{J_{l\pm1}(k_{lm}a)}{J_l(k_{lm}a)} = \pm\kappa_{lm}\frac{K_{l\pm1}(\kappa_{lm}a)}{K_l(\kappa_{lm}a)} \tag{4.12}$$

whose discrete solutions give rise to the propagation modes. Approximating the solutions by the roots of the Bessel functions yields $k_{lm} = (|l| + 2m)\pi/2a$. As the field has to fulfil the guiding condition $k_{lm} < \mathrm{NA}k_0$, i.e. free in the core but decaying in the cladding, the equation has a limited number of solutions, determining the total (polarization-degenerate) number of modes $M = 2(k_0 a \mathrm{NA}/\pi)^2$ [67].

Fig. 4.3 shows some LP_{lm} propagation eigenmodes, where the real part of the complex mode profiles are shown. Higher order modes exhibit oscillations, which indicate a tilted wavefront. Thus one can identify growing mode numbers m as increasingly angled

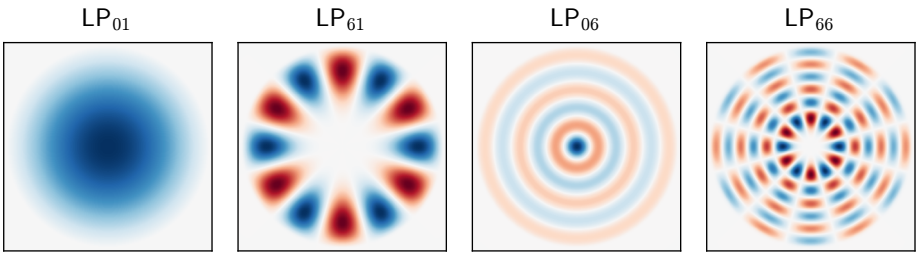

Figure 4.3: **LP modes of round-core step-index fibres.**
The plots show the real part of the polarization-degenerate linear polarized LP_{lm} modes with azimuthal mode number l and radial mode number m. Angled light rays correspond to oscillating fields whose frequencies grow with mode number. Its absence in LP_{01} identifies it as the straightly propagating fundamental mode, whereas e.g. the ring-shaped LP_{61} mode corresponds to skewed beams.

propagating light rays, $l = 0$ as meridional rays and growing $|l|$ as increasingly skewed rays. Particularly note that high $|l|$ modes tend to depopulate the fibre centre. As the group velocity reduces with increasing mode number, this results in a spatially inhomogeneous velocity distribution, affecting the fibre induced decorrelation (as it relies on variety of differential modal delays, i.e. differences of the inverse group velocities).

Square Core

For square-core step-index fibres with core side length $2a$, no separation of variables is possible since the refractive index profile does not factorize. Instead the separable problem with $n_1 \gg n_2$ (neglecting the evanescent part of the mode in the cladding, analogously to the infinite quantum well) is solved under the guiding condition $k_m^2 + k_n^2 < \mathrm{NA}^2 k_0^2$. Here the transversal profile is written as $A(\boldsymbol{\rho}) = A_x(x)A_y(y)$, which leads to decoupled harmonic oscillators with modes $|m\rangle$ and $|n\rangle$. The mode profile in the x dimension is thus given by

$$A_x(x) \propto \begin{cases} \sin(k_m x) & m \in 2\mathbb{Z} \\ \cos(k_m x) & m \in 2\mathbb{Z}+1 \end{cases} \tag{4.13}$$

with discrete solutions $k_m = \frac{\pi}{2a} m$. As the y dimension behaves analogously the combined, transversal eigenvalue is $k_{mn}^2 = k_m^2 + k_n^2$ and the total (polarization-degenerate) number of modes $M = (k_0 a \mathrm{NA})^2/\pi$.

In contrast to the modes of the round-core fibres, the square-core LP_{mn} modes, some

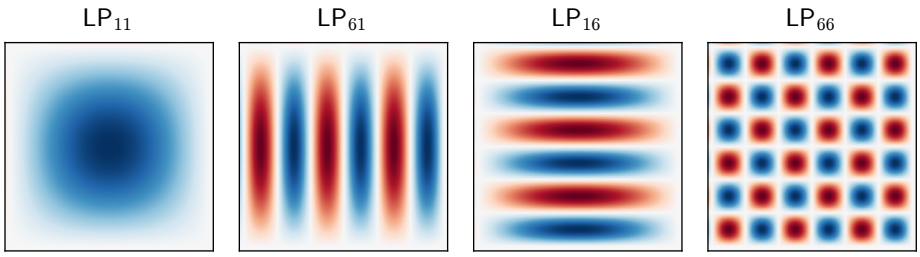

Figure 4.4: **LP modes of square-core step-index fibres.**
The plots show the real part of the LP_{mn} modes with mode numbers m and n corresponding to the x and y dimensions. LP_{11} represents the fundamental mode and higher order modes correspond to light ray propagation with steeper angles. In contrast to the round-core modes, the square-core modes are evenly distributed across the fibre core.

shown in fig. 4.3, do not have a pronounced area with propagation speed separation and light power is more evenly distributed.

Differential Mode Delay and Residual Coherence

In telecommunication applications it is common to describe modal dispersion in terms of the differential mode delay $\tau_f = \Delta t_{\max} - \Delta t_{\min}$, i.e. the delay difference between fastest and slowest mode. In order to assess the fibre decoherence properties, a histogram of the time delay per unit length $\Delta t_m/L = 1/v_m$ with the modes as ensemble is evaluated (fig. 4.5). The parameters are chosen to reflect the experimentally studied round-core (square-core) fibres with core radius $a = 62.5\,\mu\mathrm{m}$ ($a = 75\,\mu\mathrm{m}$) and numerical aperture $\mathrm{NA} = 0.22$ ($\mathrm{NA} = 0.39$) at the central wavelength $\lambda = 780\,\mathrm{nm}$. The differential mode delays are $\tau_f/L = 38\,\mathrm{ps/m}$ ($\tau_f/L = 118\,\mathrm{ps/m}$).

Fig. 4.5 also shows that the modal delay distribution is well-approximated by a uniform distribution $p(0 \leq \Delta t \leq \tau_f) = 1/\tau_f$. Evaluating eq. (4.8) thus gives a simple relation for the residual coherence

$$|\gamma_{A,\mathrm{res}}|^2 = \frac{1}{\tau_f} \int_{-\tau_f}^{\tau_f} \left(1 - \frac{|\Delta t|}{\tau_f}\right) |\gamma_a(\Delta t)|^2 d\Delta t \to \frac{\tau_c}{\tau_f} \tag{4.14}$$

by identifying the temporal coherence length $\tau_c = \int |\gamma_a(\tau)|^2 d\tau$ and where the limit (which is also an upper bound) is valid if $|\gamma_a(\tau)|^2$ has substantially decayed on the scale of τ_f.

Additionally, this continuum approximation does not take into account the finite mode

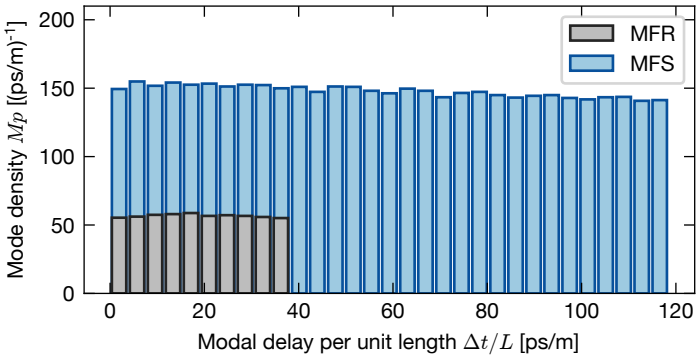

Figure 4.5: **Distribution of modal delays.**
The graphs show the numerically calculated (4.12, 4.13) modal histogram of the differential modal delay per unit length for a round-core step-index fibre (MFR) with core radius $a = 80\lambda$, numerical aperture NA $= 0.22$, and a square-core step-index fibre (MFS) with core half-side length $a = 96\lambda$, NA $= 0.39$. The total number of modes are given by $M \sim 2150$ and $M \sim 17500$, respectively, and p denotes the normalized distribution. The larger NA of the MFS allows for larger propagation angles (and thus larger differential mode delays) than the MFR, and additionally its larger core size contributes to a larger number of propagation modes.

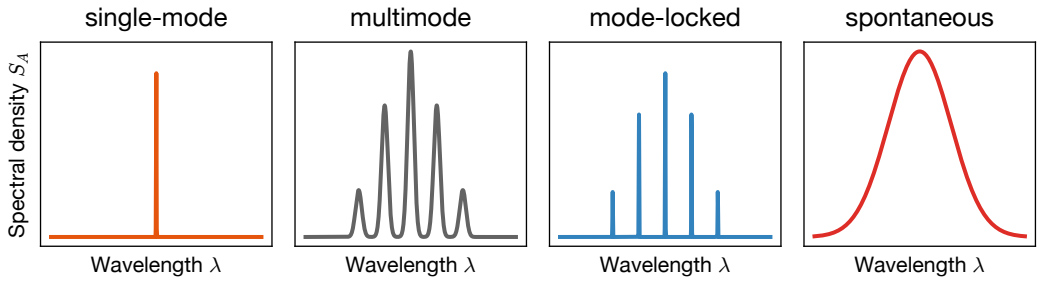

Figure 4.6: **Spectral properties of light sources.**
The graphs depict typical optical spectra of single-mode, multimode, femtosecond (mode-locked) lasers and amplified spontaneous emission sources. Single-mode and mode-locked lasers can produce very narrow linewidths, while multimode laser linewidths are broader since individual modes can fluctuate independently. Spontaneous emission sources show continuous random spectra without discrete mode structures.

number. Since coherence reduction results from statistical averaging of uncorrelated fields, it is limited by the inverse number of degrees of freedom (the non-degenerate mode number $\tilde{M}$), such that $|\gamma_{A,\mathrm{res}}|^2 > 1/\tilde{M}$. From the ideal fibre calculations above one would expect $\tilde{M} \sim \sqrt{M}$, but real fibres are always subject to mode coupling lifting the degeneracy, such that one can expect a scaling $\tilde{M} \propto M$ [73].

4.1.2 Broadband Light Sources

Since the fibre-based spatial coherence reduction relies on temporal incoherence, the properties of the illuminating light source (fig. 4.6) are of major importance not only to temporal intensity noise but also to coherence reduction performance.

Incoherent Sources

Temporally incoherent light sources have random emission characteristics and are naturally widely available (e.g. thermal sources, spontaneous emission sources). The challenge is to achieve high intensities and is accomplished using ASE, where spontaneously emitted radiation reaches a gain medium and is coherently amplified.

A compact and affordable class of light sources are semiconductor-based sources, which consist of electrically driven, optically active, edge-emitting pn-junctions, and produce a spontaneous emission spectrum when driven at low currents. If the emitted light is fed back, a lasing threshold current exists over which selective modes are exponentially

amplified, leading to a narrowband spectrum. However, if due to low light feedback spontaneously emitted light is predominant in the active region, ASE arises and the whole spontaneous, incoherent spectrum experiences significant gain. Superluminescent diodes (SLDs) enforce this behaviour [74] by tilting the end facets, resulting in minimized backreflections. If a single-mode waveguide structure is used as active region, only a single transversal mode is excited while an unrestricted number of longitudinal modes are allowed, resulting in broadband but spatially coherent output.

Producing random emission, the Siegert relation (2.16) for chaotic light sources can be used to estimate the intensity noise, which in the low-frequency limit yields a RIN of $s_I(\omega \to 0) = 2/\Delta\nu$ where $\Delta\nu$ is the optical bandwidth (2.14).

Coherent Sources

Broadband light can also be coherently generated, which has the advantage that second-order temporal correlations (intensity) are independent of first-order correlations (spectrum), and is achieved by mode-locking [75].

Consider a laser with a broadband gain spectrum $S_A^{(\mathrm{sp})}(\omega)$ and a resonator with linearly spaced longitudinal modes $e^{i\omega_n t+\varphi_n}$ centred at frequencies ω_n. If running freely above threshold, lasing can occur on multiple modes simultaneously and independently, i.e. the phase φ_n of each mode fluctuates independently (equivalently stated, the instantaneous resonance frequencies can drift relative to each other). Temporal mode-locking refers to periodically modulating the gain with frequency ω_{rep} such that only one phase value $\varphi_n = \varphi$ is amplified and others are suppressed. Then one obtains a fully deterministic field with a comb-like spectrum

$$S_A^{(\mathrm{fc})}(\omega) = S_A(\omega) \sum_n \delta(\omega - (\omega_{\mathrm{ceo}} + n\omega_{\mathrm{rep}})), \tag{4.15}$$

where ω_{rep} is the pulse repetition rate, ω_{ceo} is the carrier-envelope offset (CEO) which accounts for the difference of carrier and envelope frequency, and the spectral envelope $S_A(\omega)$ is determined by $S_A^{(\mathrm{sp})}$. If all phases are aligned, (in analogy to the Fraunhofer diffraction pattern of a grating in space) interference leads to sharp pulses in the time domain. As the modes are mutually coherent, noise affecting one mode is distributed to all modes, leading to narrow linewidths of the individual modes. The RIN thus behaves like a narrowband laser, but is peaked at the repetition rate frequencies $s_I(\omega) \sim \delta(\omega - n\omega_{\mathrm{rep}})$.

If a spectrum with a nanometre-wide bandwidth needs to be mode-locked, the gain

modulation is passively achieved, for fibre lasers often nonlinear optical loop mirrors are used [76]. Phase-aligned fields thus emit femtosecond pulses which can be dispersively elongated.

4.2 Setup

In this section the experimental setup for fibre-based generation of incoherent light is described, as well as the measurement principles to evaluate the coherence properties.

Light Sources

In order to compare the effects of different optical spectra, multiple light sources with fundamentally varying light generation processes are studied in this chapter. All light sources are transmitted through a single-mode fibre before the light is modified to reduce coherence.

One of the tested temporally incoherent light sources is the single-mode fibre pigtailed Superlum SLD-261 (SLD670) (Superlum DBUT), which is driven by its associated driver at a current of $I_{\mathrm{SLD670}} = 127.5\,\mathrm{mA}$. The other incoherent broadband light is generated by the laser diode Eagleyard EYP-RWE-0780 (LD780) (in a home-built linear laser casing whose feedback mirror is removed), and is powered by a Toptica DC110 driver at a current of $I_{\mathrm{LD780}} = 120\,\mathrm{mA}$. In order to stay below the lasing threshold and retain the broad diode spectrum, reflective feedback is avoided by placing a Faraday isolator after the output.

As a coherent light source, the 780 nm Menlo M-Comb/M-VIS (FC780) mode-locked femtosecond laser [75] (as part of the Menlo FC1500 frequency comb) is tested. The FC780 oscillator is an 1560 nm Erbium-doped fibre ring-laser (M-Comb module) operating at a repetition rate of $f_{\mathrm{rep}} = 250\,\mathrm{MHz}$ and is passively mode-locked using a nonlinear optical loop mirror [76]. Its output is amplified in another Erbium-doped fibre and frequency doubled to 780 nm (M-VIS module) at 200 mW average power. For practical reasons the light is coupled into an 80 m single-mode fibre, which in turn is coupled via a fibre-coupler into another 20 m single-mode fibre leading to the optical table.

In order to have a comparison value for the generated incoherent light, the NBL780, a grating-based ECDL, serves as a coherent reference light source.

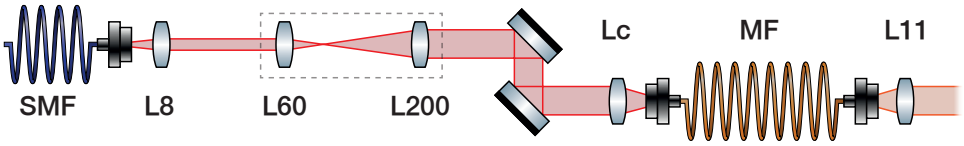

Figure 4.7: **Setup for multimode fibre-controlled spatial decoherence.** The single-mode fibre (SMF) coupled light is collimated with an $f = 8\,\text{mm}$ lens (L8), is widened by a $M = 3.5$ telescope to a Gaussian beam waist of $w = 4\,\text{mm}$ at the fibre plane (long propagation distances lead to diverging beams) and is coupled into different multimode fibres (MF) with varying lenses (Lc). The incoherent output light field is collimated with a $f = 11\,\text{mm}$ lens (L11).

Optical Fibres

The multimode optical fibres studied in this chapter are multimode silica fibres. Tab. 4.1 gives an overview over the tested fibre model, length L, core diameter $2a$, numerical aperture NA and the theoretically expected differential mode delay τ_f (4.14) at a wavelength of $\lambda = 780\,\text{nm}$.

Fibre model (abbreviation)	Length L	Core size $2a$	NA	Delay τ_f
Thorlabs FG105LCA (MFR5)	5 m	105 µm	0.22	190 ps
Thorlabs FG105LCA (MFR20)	20 m	105 µm	0.22	760 ps
Thorlabs FP150QMT (MFS5)	5 m	150 µm	0.39	590 ps
Thorlabs FP150QMT (MFS25)	25 m	150 µm	0.39	3000 ps
Thorlabs GIF625 (MFG5)	5 m	62.5 µm	0.275	1 ps [77]

Table 4.1: Overview over optical fibre properties.

The graded-index fibre Thorlabs GIF625 (MFG5) provides a reference as a multimode fibre with low modal dispersion.

4.2.1 Implementation of Fibre Approach

The setup used to generate spatially incoherent light with a multimode fibre is shown in fig. 4.7. Since decorrelation is fully passively achieved in the fibre and the incoupled light is spatially single mode, the collimated beam only has to be expanded with a telescope to a beam size which produces the desired convergence when coupling into the fibre. Here a Gaussian beam waist of $w = 4\,\text{mm}$ is chosen, which for the coupling lens focal lengths $f = 11, 4\,\text{mm}$ amounts to converging angles corresponding to numerical apertures of $\text{NA} = 0.18, 0.5$. The actual experimental implementation uses flip mirrors

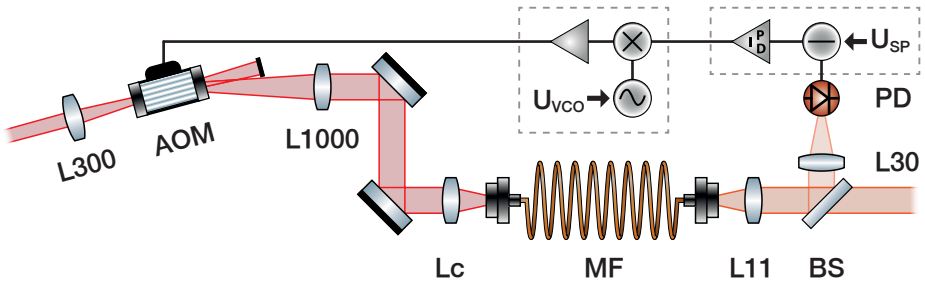

Figure 4.8: **Intensity stabilization setup.**
A given spatially coherent input beam passes the first diffraction order of an AOM placed within the focus of a large focal length telescope for beam expansion, and is coupled into the multimode fibre (MF). A beam sampler (BS) splits a small fraction of the light to a photodiode (PD) whose signal feedbacks a proportional-integral (PI) control loop with setpoint SP. A voltage-controlled oscillator (VCO) generated RF signal is mixed with the PI control signal to modulate the AOM driving power.

to direct incoming light onto a common path, and further flip mirrors to switch between coupling lenses.

Intensity Noise

Light intensity power spectral densities are measured by illuminating a sufficiently fast photodiode which outputs a linear voltage signal, such that a spectrum analyser can measure light power fluctuations. Low frequency (up to 100 kHz) spectra are obtained using the Stanford Research Systems SR760 which records voltage traces in the time domain and uses fast Fourier transform (FFT) to calculate the spectrum. For higher frequencies the Agilent N9320 RF spectrum analyser is used. Calculation of normalized spectra also requires the mean power which is measured using a time-averaging voltmeter.

Note that clipping the light beam might influence the result: Whereas under- or overfilling the photodiode active area is insignificant for single spatial mode illumination, simultaneous incidence of different numbers of coherence areas of a spatially multimode beam can in principle lead to varying noise spectra since the locally independent fluctuations are averaged. Assuming spatially invariant temporal noise statistics, homogeneous illumination with M mutually incoherent areas leads to a noise suppression factor $1/\sqrt{M}$. Thus selectively blocking a part of the beam using a pinhole before the photodiode allows the recording of spatially dependent intensity noise properties.

In order to correct fluctuations in light power, the intensity stabilization setup shown

in fig. 4.8 is used. Hereby, intensity control is realized using the first-order diffracted output of an AOM driven in a regime where the diffraction efficiency is linear in RF power. The error signal is generated by comparing a setpoint voltage from a low noise voltage source with the output of a photodiode measuring the light intensity. Using this signal a PI controller outputs a control signal setting the RF signal power driving the AOM. As a stable intensity is required after propagation through the multimode fibre but acousto-optic Bragg diffraction efficiency is wavevector selective (focusing an incoherent beam to typical AOM aperture sizes leads to significant divergence, i.e. a large wavevector distribution), the control AOM is placed before the multimode fibre whereas the feedback photodiode is placed thereafter.

4.2.2 Lateral Shift Interferometer

In order to characterize the coherence after propagation through the multimode fibre, a laterally shifting Michelson interferometer is used, which is able to measure the full spatiotemporal coherence function (fig. 4.9, [78]).

Principle

The interferometer is based on a Michelson interferometer whose planar mirrors are replaced by retroreflectors ("cat's eyes"). When a light beam is incident on the non-polarizing beam splitter, each of the beams is reflected from a horizontally oriented retroreflecting mirror. This introduces a double-reversal of the wavefront of the beam and a horizontal displacement when off-centrally incident. After recombination at the beam splitter, the measurable intensity profile at one output is given by

$$I_{lt}(\boldsymbol{\rho}) = |A_l(\boldsymbol{\rho}) + A_t(\boldsymbol{\rho})|^2 = I_l(\boldsymbol{\rho}) + I_t(\boldsymbol{\rho}) + 2\,\mathrm{Re}\,\Gamma_{A,lt}(\boldsymbol{\rho}), \tag{4.16}$$

where l, t denote the interferometer paths, I_{lt} the intensity of the coherent superposition of fields A_l, A_t and $\Gamma_{A,lt}$ the cross-correlation thereof. As there is free space access to the individual paths, the coherence function can be obtained by recording single-path images (blocking either beam) and performing the normalization $\gamma_{A,lt} = (I_{lt} - I_l - I_t)/2\sqrt{I_l I_t}$. If the beams on both paths have the same path lengths and are identically displaced, the recombination produces identical, perfectly superposed beams $A_l = A_t$.

Longitudinally translating a retroreflector by $z/2$ does not alter the transversal displacement, so for perfect spatial overlap one has $A_l(\boldsymbol{\rho}, t) = A_t(\boldsymbol{\rho}, t + z/c)$. Therefore the perfect overlap configuration reduces to a Michelson interferometer with which the

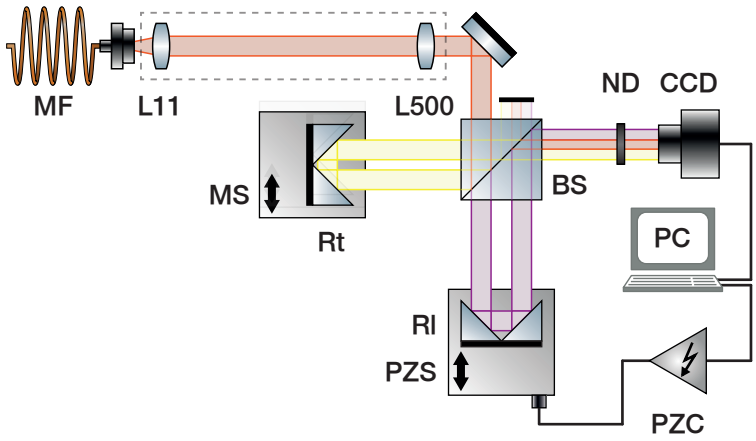

Figure 4.9: **Implementation of the lateral shift Michelson interferometer.** The interferogram generating part starts with a 50/50 non-polarizing beam splitter (BS) splitting the incoming beam (red). The transmitted part (purple) is backreflected by the retroreflector Rl whose position can be longitudinally scanned by a piezo actuated translation stage (PZS). The reflected part (yellow) also returns from a retroreflector (Rt) which can be laterally shifted by a manual translation stage (MS). At the BS the beams are recombined (red) but have an offset due to the shifted Rt (purple and yellow). The interferogram is recorded by a CCD camera after passing a neutral density filter (ND). The process is automatized using a computer (PC) which receives the camera images and sets the piezo actuator voltage via a piezo controller (PZC). The lenses (L11, L500) before the BS are used to image the light field at the output of the optical fibre (MF) onto the camera.

temporal correlation function can be measured. In the opposite case, transversally translating a retroreflector by $s/2$ does not alter the longitudinal displacement and introduces an equal-time lateral shear of the output beam $A_t(\boldsymbol{\rho}, t) = A_l(\boldsymbol{\rho} + s\mathbf{e}_s, t)$.

As one is interested in the degree of coherence $|\gamma_A|$ and the camera records the interference fringes $\operatorname{Re}\Gamma_A$, one can sweep the relative longitudinal displacement across the extremal equal-time position. The extrema of the spatially resolved envelope then give the spatial correlation function.

Implementation

Since longitudinal interference fringes have a periodicity of an optical wavelength, the displacement of the longitudinal retroreflector is realized with a translation stage comprising a linear piezo actuator, theoretically allowing positioning with nanometre precision. Being an open-loop transducer, the piezo hysteresis [79] is accounted for by performing a calibration measurement with the NBL780 laser. The transversal retroreflector is mounted on a manual micrometre stage since the precision requirements are less stringent.

This is ensured by a 4f-imaging system installed before the interferometer, with which the fibre output face is magnified by $M = 45$. As the interferometer only linearly shears the beam, image formation is not altered and aberrations (minimized by long focal lengths) are equally introduced in both interferometer paths. The images are recorded with an AlliedVision Manta G-145B NIR CCD camera, where saturating intensities are attenuated with absorptive neutral density filters.

Measurement

The coherence function is measured by sequentially, manually adjusting the transversal displacement and measuring the temporal coherence function for each displacement position. For this the piezo voltage is set to the minimal value, where the normalization images are recorded. Then the piezo actuator voltages are discretely stepped, thus obtaining the spatially resolved temporal correlation functions. For most measurements the relative longitudinal displacement of $2 \cdot 20\,\mu\text{m}$ is scanned in 500 steps ensuring each fringe to be sampled about 10 times.

The equal-time degree of coherence for a given transversal displacement is approximately given by the extrema of the temporal degree of coherence function of each pixel. Regarding this quantity as a function of transversal displacement yields the spatial degree of coherence $|\gamma_A(s)|$. The coherence length is deducted by integrating the measured

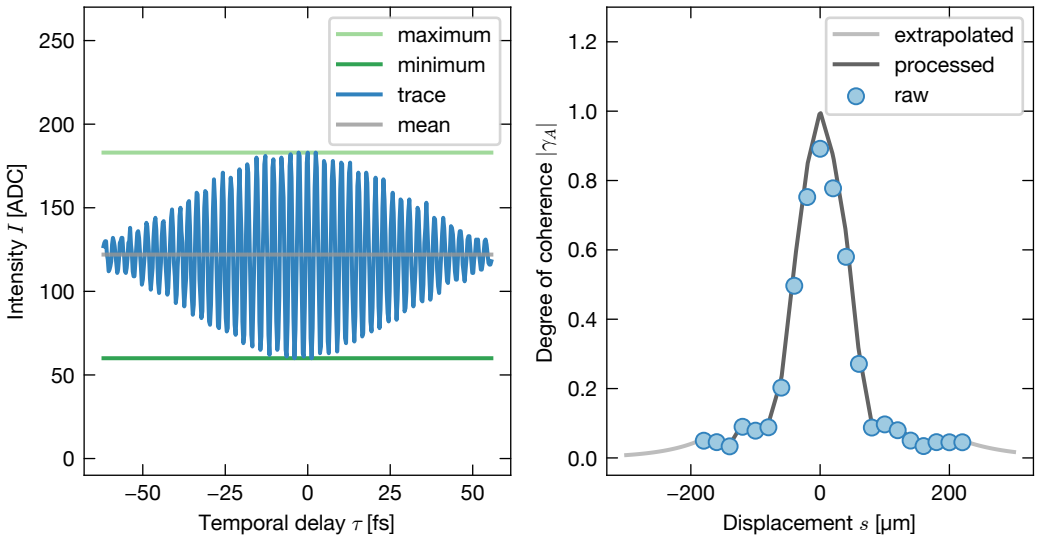

Figure 4.10: **Interferometer measurement data processing.**
For a given transversal displacement s of the retroreflector, a longitudinal (i.e. temporal) interferogram is taken pixelwise. The left plot shows an exemplary measurement for one pixel (here $s = -40\,\mu\text{m}$). First, images of the individual interferometer paths are recorded whose incoherent sum is plotted as "mean". Then the longitudinal trace is recorded and its extrema are registered. Normalization according to eq. (4.16) yields a spatial coherence data point.
Repeating this procedure for all transversal displacement steps gives a spatial coherence function $|\gamma_A(s)|$ for each pixel (right plot, raw). These functions are linearly transformed to ensure that their maximum is unity and located at zero displacement (processed). In order to obtain the spatial coherence length s_c (2.12), an exponential decay (extrapolated) is assumed for the tail contribution.
For measuring the residual coherence $|\gamma_{A,\text{res}}|$, a single large transversal displacement is chosen. Then a pixelwise histogram of coherence values is taken, from which the mean and the standard deviation is obtained.

(finite-extent) spatial coherence function (2.12). The missing tail mass is estimated by assuming an exponential decay from the boundary values $|\gamma_A(s_{\min,\,\max})|$ (fig. 4.10).

The residual degree of coherence $|\gamma_{A,\mathrm{res}}|$ is measured by transversally displacing the beam far away from the main coherence function peak, typically $s = 1\,\mathrm{mm}$ is chosen. Then the mean and the standard deviation of the coherence value of each pixel is taken, where the standard deviation includes both the actual spread of the distribution and measurement uncertainties (this quantity will be plotted as error bars). Note that pixelwise averaging (of coherence length or residual coherence) implicitly assumes a Schell model source (2.18).

The main measurement error originates from the imperfectly mounted retroreflector (with an estimated relative angular misalignment of $\sim 0.9°$ between the retroreflectors), resulting in a mutually rotated beam profile. The consequence is that for a fixed transversal stage displacement the actual beam displacement becomes image-position-dependent. To correct (reduce) this effect, the point of zero lateral displacement is shifted pixelwise to the maximum of the measured (raw) spatial coherence function. The function is also normalized such that the maximum is unity.

Additionally, the finite dynamic range of the camera (8 bit) sets a limit to coherence measurement uncertainty. Let the images from the two interferometer arms have analogue-digital converter (ADC) values of $N_{l,t}$, then eq. (4.16) implies that the deduced coherence value cannot fall below $\delta = 1/2\sqrt{N_l N_t}$, leading to an uncertainty of $\Delta|\gamma_A| = \delta/2$. In order to avoid an excessive uncertainty, values below a cutoff (here $\Delta|\gamma_A| = 0.01$ is chosen) are masked pixelwise and not taken into account in further analyses.

4.3 Temporal Coherence

As short coherence times are not only desirable to be able to illuminate quickly responding atomic systems, but are a central requirement for spatial decorrelation after propagation through the multimode fibre, the temporal coherence properties of the studied primary and decorrelated light sources are discussed in this section. Additionally, the temporal coherence functions deduced from the optical spectra are verified by direct interferometric measurements.

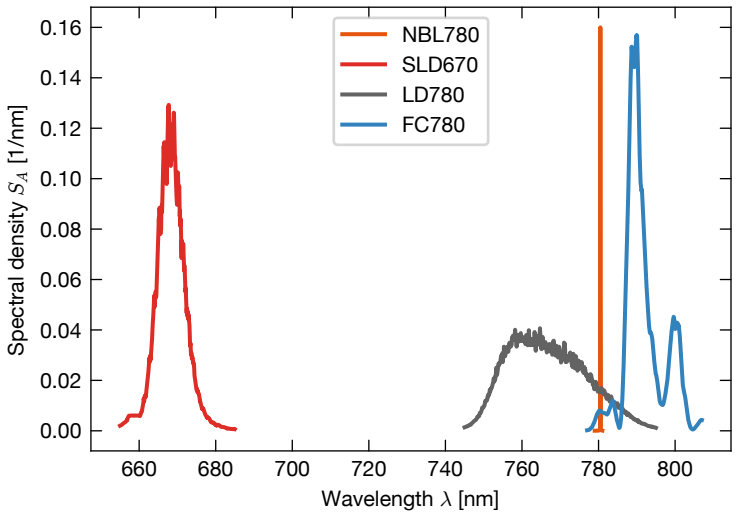

Figure 4.11: **Optical spectra of the studied light sources.**
The light sources include a narrowband laser (NBL), a superluminescent diode (SLD), a laser diode (LD) and the frequency comb (FC), where the numbers denote the specified centre wavelength. Note that the NBL780 has been scaled down to fit the canvas.

Optical Spectra of Light Sources

The optical spectra of the light sources are measured by coupling the light into a short optical fibre connected to the Yokogawa AQ6315A grating-based optical spectrum analyser. The results are depicted in fig. 4.11, normalized to their total power.

The LD780 emits a broad, noisy spectrum centred at 770 nm indicating a spontaneous emission spectrum and operation below lasing threshold. The spectral fluctuations are introduced by substantial uncontrolled feedback, leading to random multimode noise. The lack of any large peaks suggests that external reflective feedback is negligible, such that the diode can be treated as a spatially single-mode broadband light source. The SLD670 behaves similarly and emits a symmetric spectrum around 670 nm. Instead of the strong spectral noise it features a more homogeneous, continuous spectrum, as expected from specifically designed ASE sources. The remaining spectral ripple is also indicative of residual feedback towards the gain area and typical for SLDs.

The femtosecond laser from the FC780 operates at around 790 nm and consists of a two-peak profile roughly following the (frequency-doubled) Erbium gain profile [80]. The narrowband reference laser NBL780 has a linewidth much smaller than the optical

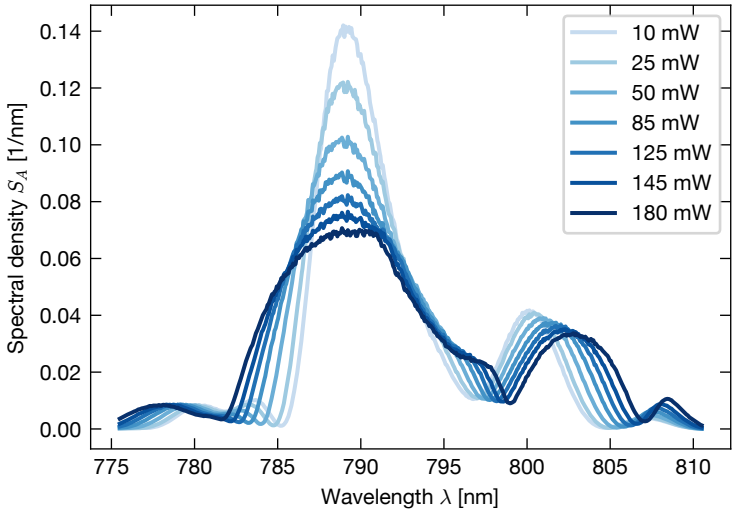

Figure 4.12: **Spectral broadening of femtosecond laser.**
The spectra of the FC780 are measured after 100 m of single-mode fibre propagation, where the nonlinear effect of self-phase modulation (SPM) broadens the spectrum depending on the transmitted light power.

spectrum analyser resolution and is centred at 780 nm.

Variation of Spectra

For high (peak) power light sources like the femtosecond laser, spectral broadening can be achieved by self-phase modulation (SPM) in the long ($L = 100\,\mathrm{m}$) single-mode fibre leading to the optical table (sec. 4.2). This nonlinear effect becomes significant when the intensity reaches $I \sim \lambda/n^{(2)}L$ [81]. With wavelength $\lambda \sim 790\,\mathrm{nm}$, the silica Kerr nonlinearity $n^{(2)} \sim 2.7 \times 10^{-9}\,\mu\mathrm{m}^2/\mathrm{kW}$ and mean output power $P \sim 100\,\mathrm{mW}$, this regime is reached, as seen in fig. 4.12, granting a possibility to tune the desired spectrum.

To estimate unexpected spectral changes due to the subsequent multimode fibre propagation, the spectrum after the single-mode fibre is compared to the spectrum after both fibres, for which no significant difference is found. This can be attributed to the larger core size and dispersion in the single-mode fibre, stretching the pulse duration and decreasing the peak power [82]. If higher peak intensity femtosecond lasers are used, unwanted spectral broadening can thus be always avoided by dispersing the ultrashort pulses before incoupling, e.g. using positively chirped mirrors [83].

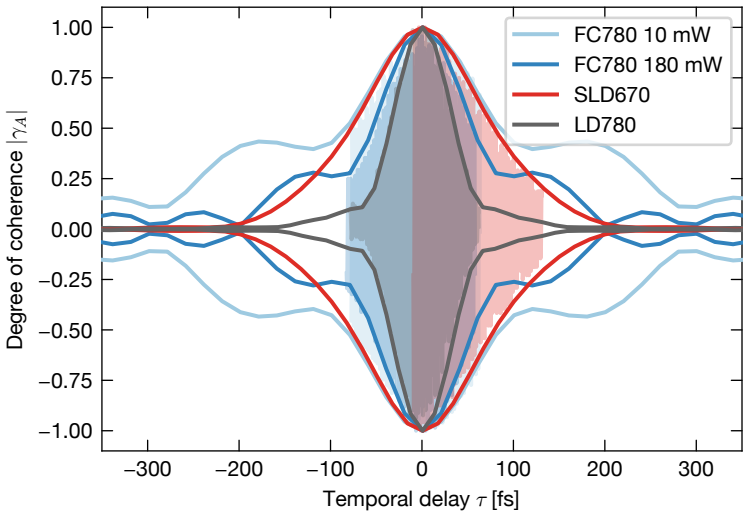

Figure 4.13: **Temporal coherence functions after multimode fibre.** The opaque lines show the spectrally expected degree of temporal coherence $|\gamma_A|$, and the semi-transparent lines (background colour) show the oscillating coherence functions $\mathrm{Re}\,\gamma_A$ directly measured with the interferometer. While the coherence functions of the superluminescent diode (SLD) and laser diode (LD) monotonically decay, the double peaked spectrum of the femtosecond laser (FC) leads to an oscillating behaviour. Increasing the FC780 power decreases its coherence time below the SLD670.

Coherence Function

As the temporal coherence function of a spatially coherent light field is fully determined by its optical spectrum (2.13), the previously measured spectra can be used to calculate the input temporal coherence functions. Using the interferometer (sec. 4.2.2) in the Michelson configuration allows for the spatially resolved measurement of the temporal coherence function, detecting potential propagation induced spectral changes.

Fig. 4.13 shows the directly measured temporal coherence functions in comparison to the spectrally expected ones. Plotting the spatially resolved coherence function, one cannot distinguish any significant differences, such that one can assume that the spectral features in the regime relevant for induced coherence reduction ($\mathcal{O}(\mathrm{nm})$) remain unchanged. This agreement with the theoretical estimation (4.10) indicates that there is no significant spatiotemporally coupled losses.

Tab. 4.2 gives an overview over the coherence times τ_c (2.12) associated with the light sources.

Light source (abbreviation)	Remark	Coherence time τ_c
Superlum SLD-261 (SLD670)		118 fs
Eagleyard EYP-RWE-0780 (LD780)		55 fs
780 nm Menlo M-Comb/M-VIS (FC780)	10 mW	170 fs
780 nm Menlo M-Comb/M-VIS (FC780)	180 mW	95 fs

Table 4.2: Overview over light sources.

Since the differential mode delays τ_f of the step-index fibres (4.14) all by far exceed the coherence times $\tau_c \ll \tau_f$ (4.14), the spatial decoherence is expected to be mode-excitation limited.

Note that since the FC780 is a coherent light source, its temporal coherence function has periodic revivals set by the repetition rate f_{rep}. Thus if the modal dispersion of the fibre used for coherence reduction exceeds the pulse spacing, no more decorrelation is possible. The critical length can be estimated from the differential mode delay (sec. 4.1.1) as $L_{\mathrm{rep}} \sim 2cn/f_{\mathrm{rep}}\mathrm{NA}^2 \sim 25\,\mathrm{m}$, which is not exceeded by the studied fibres.

4.4 Spatial Coherence

In this section the spatial coherence properties of broadband light fields after transmission through a multimode fibre are studied and the influence of fibre type, incoupling conditions and spectral properties is discussed.

4.4.1 Coherence Function

The short range behaviour of the spatial coherence function is of interest since it determines how fine imaged structures can be to still remain mutually incoherent. If a statistically large number of mutually incoherent modes are excited and each point in the output plane is composed of many modes, one expects that the spatial coherence function (by definition peaked at value 1) quickly decays on a characteristic coherence length scale s_c (4.9).

Fig. 4.14 shows the beam-averaged spatial coherence function $|\gamma_A(s)|$ at the output of the fibres Thorlabs FG105LCA (MFR20) and Thorlabs FP150QMT (MFS25), measured for the LD780 with a $f = 4\,\mathrm{mm}$ incoupling lens. These step-index fibres are compared to the MFG5 graded-index fibre where decorrelation is not yet achieved (4.14) and a single-mode fibre (SMF) which is spatially coherent. Both are illuminated with the SLD670.

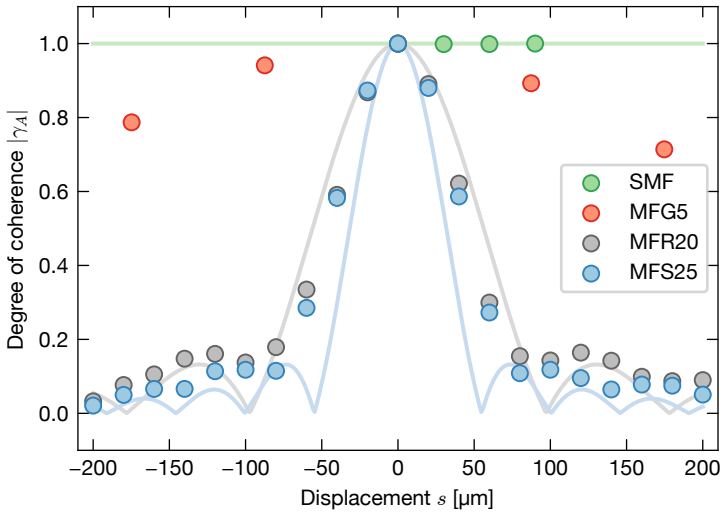

Figure 4.14: **Profile of spatial degree of coherence.**
The beam-averaged spatial coherence function is measured for central incoupling by a $f = 4\,\text{mm}$ lens and has a similar main peak for both the round-core (MFR) and square-core (MFS) step-index fibre. Insufficient differential mode delay leads to large coherence lengths in the case of graded-index fibres (MFG), bounded by the fully coherent single-mode fibre (SMF).
The light coloured lines show the coherence functions expected for fully incoherent light (4.9). Due to peak position variations across the beam, averaging flattens the side peaks. The discrepancy at the sides between the fibres indicates slower decay of the MFR, leading to a larger coherence length. Accounting for the 45x imaging magnification, the main peak FWHM of the step-index fibre outputs is on the order of 2 µm.

For the step-index fibres the spatial correlations exhibit a main peak which quickly decays on a similar length scale for both fibres. The coherence function has a dip after the main peak, in accordance with the oscillating Bessel function from the estimation in eq. (4.9) (where averaging has flattened the dip in the figure). The mutual discrepancy visible at larger displacements is an indication of the larger NA of the square-core step-index multimode fibre (MFS) as on the same cross sectional area more angular spread is possible. The respective integrated coherence lengths (2.12) are given by $s_{c,\mathrm{MFR20}} = 139\,\mu\mathrm{m}$ ($s_{c,\mathrm{MFS25}} = 88\,\mu\mathrm{m}$). Accounting for the 45x imaging magnification (sec. 4.2.2), the number of mutually incoherent modes (2.20) is given by $M_{\mathrm{MFR20}} \sim 20^2$ ($M_{\mathrm{MFS25}} \sim 43^2$) at 780 nm, which is also an estimate for the number of fully incoherent sites usable for optical potential generation. Note that the coherence length definition also takes into account the function tail, such that few slowly decaying functions lead to a large discrepancy in s_c despite the good overlap of the averaged main peaks.

These properties are in stark contrast to the other fibres. While the single-mode fibre is unsurprisingly fully coherent, the graded-index fibre also exhibits high correlations due to the reduced modal dispersion (three orders of magnitude lower than the step-index fibres).

4.4.2 Residual Coherence

Apart from the numbers of coherence areas (the short range behaviour of the coherence function) discussed in the previous section, the residual coherence (4.14) is of importance since it determines the overall minimal achievable degree of coherence. Fig. 4.15 summarizes the residual coherence measurements obtained for different light sources (tab. 4.2) and step-index fibres (tab. 4.1).

To isolate the effects of the coherence time, a measurement series with the combination FC780/MFS25 is taken where the spectral changes are introduced only by the nonlinear spectral broadening (sec. 4.3). Particularly, the optical path after the single-mode fibre output remains untouched, so the fibre launch conditions are identical. The results show barely any change in residual coherence. This agrees with the estimation (sec. 4.3) that the decorrelation is limited by mode degeneracy and initial mode excitation. Note that the slight increase in residual coherence with coherence time is below the measurement uncertainty, but indicates that larger spectral widths can lead to smaller residual coherence also in the mode-limited regime.

The second graph in the figure shows the fibre geometry and fibre length dependence of the residual coherence, and is measured with the SLD670 and the LD780. Since the

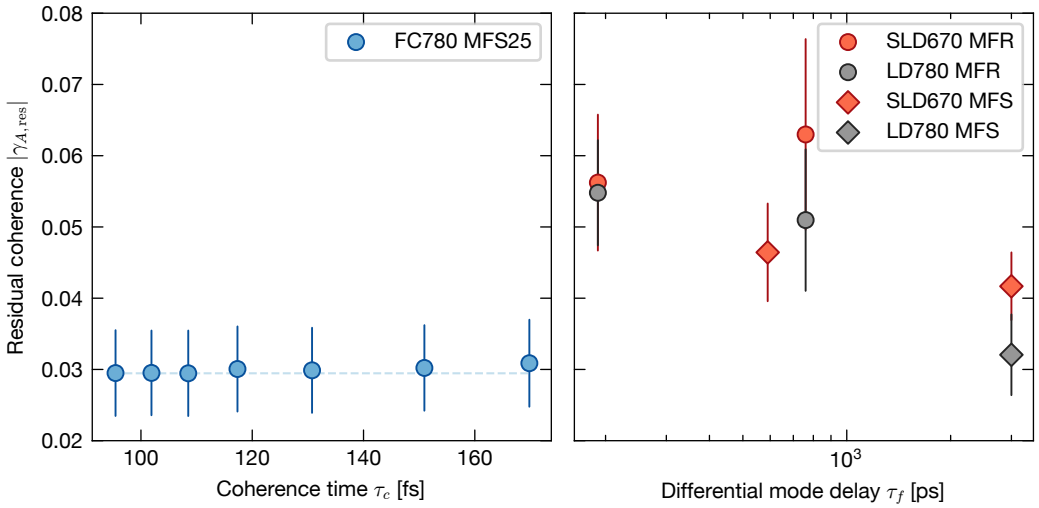

Figure 4.15: **Spectral and fibre dependence of residual coherence.**
The left plot shows the spectral dependence (fig. 4.12) of the residual coherence $|\gamma_{A,\mathrm{res}}|$ measured for the femtosecond laser (FC780) and the square-core fibre (MFS25). The minor increase of residual coherence with coherence time indicates operation in the mode excitation-limited, fully decorrelated regime. The dashed line indicates the minimal achieved value. Note that the vertical bars indicate the standard deviation of the residual coherence ensemble measured across the beam and the estimation of the mean is more precise (sec. 4.2.2).
The fibre dependence of the residual coherence is shown on the right, where measurements are taken with the superluminescent diode (SLD670) and the laser diode (LD780) for the round-core (MFR, 5 m and 20 m) and the square-core fibres (MFS, 5 m and 25 m), which are plotted in terms of their differential mode delay τ_f (tab. 4.1). The results indicate overall smaller residual coherences for the MFS, and a reduction with increasing fibre length and spectral bandwidth. However, note that these values can vary significantly due to the high mode excitation sensitivity (sec. 4.4.3).

fibre launch conditions are not perfectly fixed, leading to varying coherence reduction performance, a conclusive statement cannot be stated. However, a general tendency that longer and higher NA fibres reduce residual coherence can be observed. Furthermore, the overall lower coherence values for the LD780 again suggest better decorrelation properties for broader spectra.

Similar as in sec. 4.4.1, the measurement results can be compared to graded-index multimode and single-mode fibres. The combination SLD670/MFG5 results in $(\tau_c, |\gamma_{A,\mathrm{res}}|) = (118\,\mathrm{fs}, 0.39)$, revealing the reduced modal dispersion in graded-index fibres, and the combination LD780/SMF verifies full spatial coherence $(\tau_c, |\gamma_{A,\mathrm{res}}|) = (55\,\mathrm{fs}, 1.01)$.

4.4.3 Fibre Launch Conditions

As the incoupling conditions of the light beam define the distribution of excited fibre modes which in turn determine the intermodal propagation delays, the resulting output beam profile and spatial coherence function can vary strongly as seen in fig. 4.15. Therefore in this section the coherence reduction dependence on the incoupling conditions is studied.

To maximize the spread of propagation constants of the excited modes, a tightly focused launch of the LD780 is chosen, but is limited to ensure high light power efficiency inherent to this method. Different launch divergences are realized using different coupling lenses with focal length f, and different input angles and positions by misaligning the far coupling mirror (fig. 4.7) at a distance of $z = 200\,\mathrm{mm}$. By linearly stepping the mirror angle from the (misaligned) transmission minimum $\theta = -\theta_c$ via the maximum $\theta = 0$ to the minimum on the other side $\theta = \theta_c$ allows tracing of the correlation properties as a function of input. Since from geometric optics the coupling mirror angle θ is linearly related to both the incidence angle $\theta_{\mathrm{in}} = \theta\,(1 - z/f)$ and the incidence position $\rho_{\mathrm{in}} = f\theta/(z/f - 1)$, the critical angle θ_c is determined by either the maximal angle obeying the guiding condition of the fibre, $\theta_{\mathrm{in}} \leq \theta_{\mathrm{fibre}} \sim \mathrm{NA}/n$, or (in this case) the position given by the fibre radius $\rho_{\mathrm{in}} \leq a$.

Beam Profiles

Fig. 4.16 shows the beam profile at the end face of the multimode fibres and is the most striking difference between the fibres. At central, vertical, focused incidence (with respect to the fibre end face) only low-order modes are excited in the round-core fibre (fig. 4.3). These meridional rays (passing the optical axis) make up only a small fraction of available modes and have a high mode density in the fibre centre. When misaligning the

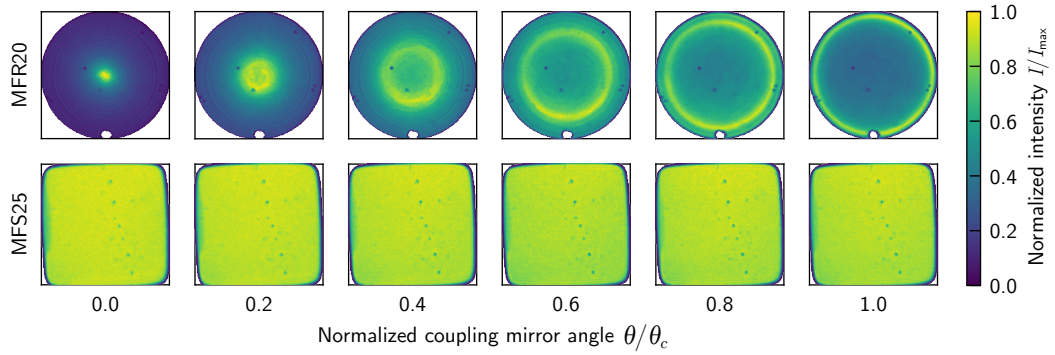

Figure 4.16: **Fibre output beam profiles for different incoupling conditions.** The images are resized to the respective fibre core diameters and the colours are normalized to the maximum intensity of each image. The top row shows the 20 m round-core fibre, the bottom row shows the 25 m square-core fibre, both illuminated with the LD780. The coupling mirror angle θ is stepped from vertical incidence on the left to the maximal angle with significant power transmission on the right. The fibre mode overlap with the Gaussian beam input is significantly better for the round-core fibre, indicating only selective mode group excitation. The intensity distribution of the square-core fibre is highly homogeneous despite the Gaussian input and very robust against input conditions.

input beam, the off-axis incidence induces a ring-shaped intensity distribution. Circular symmetry reflects the mode symmetries and the finite radial extent shows that mainly skew rays (not passing the optical axis) are excited. The radial broadening of the rings suggests a more homogeneous mode excitation due to the fact that the diverging parts of the input beam can couple into more non-degenerate mode groups. In the critical, barely guided case, most energy is lost into radiative cladding modes, which also reduces mode diversity. The intensity dip in the fibre centre again indicates a spatial separation of propagation mode groups. The white spot at the bottom of the beam profile originates from a damaged fibre end face. The same measurement with the square-core fibre reveals its fundamentally different mode structure (fig. 4.4). As the propagation modes have much more homogeneous profiles, any incoupling position leads to a spatially well-distributed intensity.

Residual Coherence and Coherence Area

Fig. 4.17 shows the dependence of the beam-averaged residual coherence on incoupling position, angle and divergence, measured for a lateral displacement of $s = 1\,\mathrm{mm}$ (i.e. $s = 0.11\,a_{\mathrm{MFR}} = 0.075\,a_{\mathrm{MFS}}$ relative to the fibre core size). Again the square-core fibre is insensitive to the fibre coupling angle and maintains a low residual coherence of $|\gamma_{A,\mathrm{res}}| \sim 0.03$. The round-core fibre on the other hand has an overall higher residual coherence of $|\gamma_{A,\mathrm{res}}| \sim 0.05$ with a peak at normal incidence. This can be explained by the low mode diversity as skewed rays are only accessible for misaligned conditions. The graph also shows the results for varying incoupling lens focal lengths, i.e. beam divergence, and hints at better performance for larger divergence due to more excited mode groups.

This picture can be verified when looking at the spatial structure of the coherence lengths, which allows for observation of mode structure dependences. Fig. 4.18 shows measurements performed for an off-axis incoupling condition matching the minimum residual coherence depicted in fig. 4.17. Similar to the beam profile, the spatial coherence length is also highly homogeneous for the MFS25, where only the edges show slightly increased coherence lengths. The MFR20 reveals its modal structure as the ring-shaped intensity profile separates an inner and an outer part. While the inner part is rather homogeneous, the outer part varies in coherence, where the area of short coherence length likely corresponds to the input position. As the skew modes are restricted from the centre and the input beam is angled towards the centre, only few skew modes are excited, resulting in the long coherence lengths in the outer part.

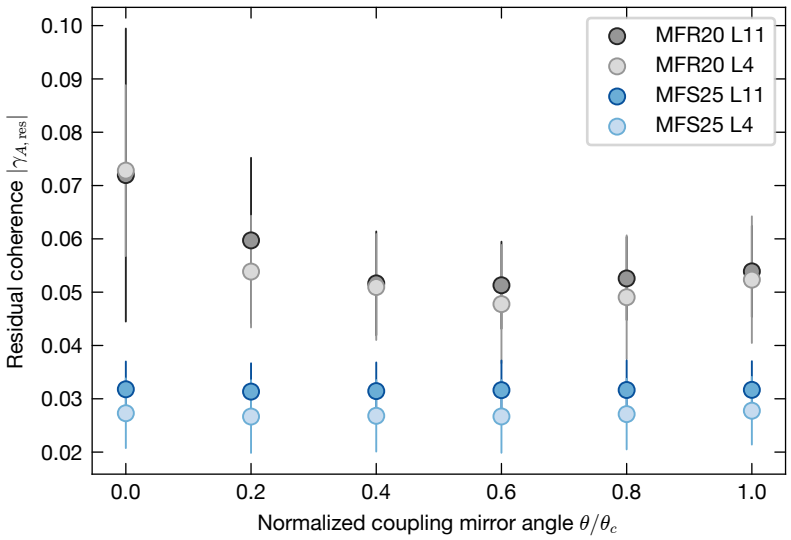

Figure 4.17: **Residual coherence for different incoupling conditions.**
The graph shows results for the round-core (MFR) and square-core (MFS) fibres with incoupling lens focal lengths of $f = 11\,\mathrm{mm}$ (4 mm) denoted as L11 (L4). The MFS reduces coherence significantly better regardless of fibre launch conditions, indicating spatially homogeneous modal delay distributions. Central launch into the MFR on the other hand only excites low order modes resulting in an increased coherence. Note that the difference in fibre length is comparatively insignificant (fig. 4.15).
Since decoherence in the MFS is insensitive to coupling position and angle, the dependence on input beam divergence can be analysed. Comparing the blue graphs, larger divergence is likely to further reduce residual coherence at the expense of decreased efficiency. Note again that the vertical bars denote the standard deviation of the residual coherence ensemble measured across the beam and is larger than the measurement uncertainty.

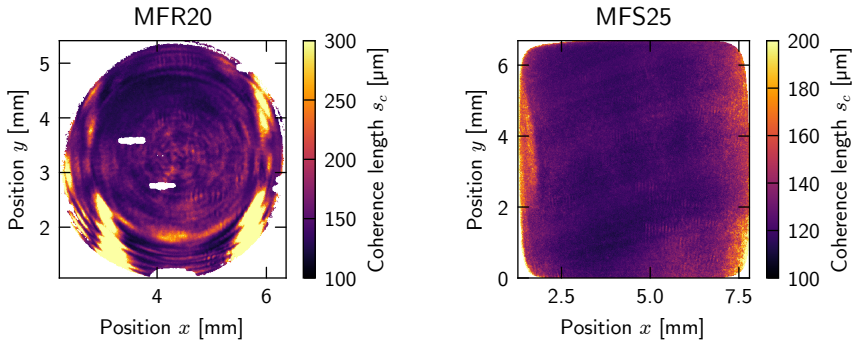

Figure 4.18: **Spatial structure of coherence length.**
For each position in the beam the spatial coherence length is calculated and plotted in a colour map for both a round-core (MFR) and a square-core (MFS) fibre (note the different colour scales). In both cases the LD780 is off-axis coupled into the fibre through a $f = 4\,\mathrm{mm}$ lens. The homogeneous mode excitation of the MFS leads to a homogeneous coherence length, while the selective mode excitation of the MFR results in spatially strongly varying properties. The white spots are a consequence of dirt blocking light propagation.

4.5 Intensity Noise

In this section the Fourier-domain correlation properties, i.e. the intensity noise, after propagation through the multimode fibre are studied for the different light sources. As spatial incoherence inherently requires a finite spectral bandwidth (2.19), Fourier-domain correlations are inevitable and in turn lead to a non-vanishing intensity power spectral density. As such global temporal fluctuations directly drive heating transitions (2.34), it is important to characterize the noise levels in the relevant frequency regime.

Noise Origin

Intensity noise can be generally separated into intrinsic noise determined by the physics of the light generation process itself and technical noise that emerges from the actual experimental implementation [84].

The intrinsic noise consists of the following statistically independent terms. First, electromagnetic field quantization leads to frequency-independent shot noise, which increases the RIN (2.15) by $s_I^{(\mathrm{sh})}(\omega) = \hbar\omega/P_0$, with light power $P_0 = \int I_0(\boldsymbol{\rho})d^2\rho$, and is thus negligible for RIN spectra at typical off-resonant dipole trap powers. Second, spontaneous emission gives rise to an incoherent continuous spectrum leading to an excess

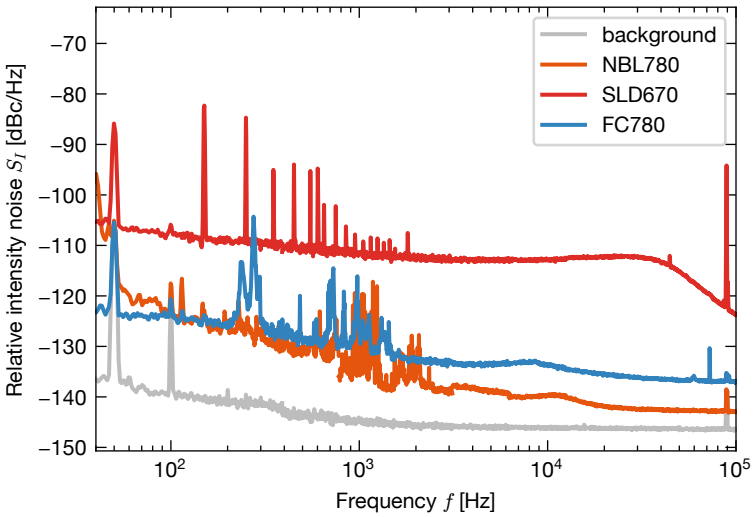

Figure 4.19: **Relative intensity noise of light sources.**
The RIN comparison between the free-running single-mode fibre coupled light sources shows that the coherent light sources (NBL780 and FC780) have significantly lower noise levels than the incoherent SLD670. The noise in the 1 kHz regime originates from fibre coupling noise. As the illuminating light power exceeds $P > 1\,\mathrm{mW}$ for all cases, the photon shot noise limit $s_I^{(\mathrm{sh})} < -155\,\mathrm{dBc/Hz}$ is negligible.

noise term (sec. 4.1.2) $s_I^{(\mathrm{sp})} = 2\beta^2/M\Delta\nu$, where $\Delta\nu$ is the spectral bandwidth (2.14) of the spontaneous emission, $\beta = P_{\mathrm{sp}}/P_0$ is the empirically obtained fraction of spontaneous emission contributing to the total power [85] and M is the spatial and polarization mode degeneracy [86].

Technical noise sources include thermal noise (scaling with temperature) which describes the fluctuations generated by the measurement electronics, electronic modulation noise (up to MHz) if the light properties are actively controlled, and mechanical noise (up to kHz) of the passed optical elements. Typically, the main technical noise of semiconductor sources is induced by fluctuating diode driving currents as it is directly carried over to the light intensity.

Relative Intensity Noise of Light Sources

Fig. 4.19 shows a comparison of the RIN of a narrowband laser (NBL), a SLD and a femtosecond laser (frequency comb (FC)). The power spectral densities of the coherent

(incoherent) sources are measured with a Thorlabs PDA10A-EC (Thorlabs PDA100A-EC at 20dB gain) photodiode at mean voltage $U_{\mathrm{dc}} = 1.2\,\mathrm{V}$ ($U_{\mathrm{dc}} = 1.05\,\mathrm{V}$) and the FFT spectrum analyser with exponentially increasing resolution bandwidths, chosen to fit the frequency range. The noise around 1 kHz present for the coherent sources can be identified as mechanical single-mode fibre coupling noise, since the noise vanishes when performing a reference free-space RIN measurement (before coupling into the fibre). The NBL RIN shows a spectrum typical for an ECDL, having a similar level as the FC. This is enabled by the fact that mode locking coherently couples the individual longitudinal modes such that excess noise is distributed among all modes, resulting in a similar noise generation process (sec. 4.1.2, [87]).

Longitudinal mode beating noise is not relevant as the NBL has a comparatively short cavity length (with free spectral ranges $\Delta\nu_{\mathrm{FSR}} \sim \mathcal{O}(\mathrm{GHz})$)) and the FC repetition rate is locked at $f_{\mathrm{rep}} = 250\,\mathrm{MHz}$. Purely random light sources do not produce such noise as quasi-continuous spectra imply fast decoherence of interfering frequencies. For the SLD670 with its coherence time of $\tau_c \sim 118\,\mathrm{fs}$, the expected spontaneous emission excess noise floor is $s_I^{(\mathrm{sp})} \sim -126\mathrm{dBc/Hz}$. Note that it has been reported [84] that SLD light amplification using gain-saturated semiconductor optical amplifiers can reduce this noise floor. Since the SLD shows a significantly higher white noise at kHz frequencies, it is most likely limited by driving current noise.

Due to low intensity, a spatially resolved RIN measurement involving only one spatial coherence area could not be performed. A pinhole-filtered measurement (2 % of total light power) for the FC780 passing the MFS25 does not show significant differences to fig. 4.19. Furthermore, since the output properties of the MFS25 are insensitive to fluctuations in the incoupling conditions, the noise within a single coherence area is not expected to be considerably larger.

Intensity Stabilization

As long-term (compared to measurement times) intensity drifts lead to varying mean intensities, low frequency noise has to be actively corrected and is achieved using a negative feedback system (sec. 4.2.1). The main difference to typical stabilization setups lies in the incoherent illumination on the feedback photodiode, which is not expected to be an issue when choosing a sufficiently large diode area. The maximum stabilization bandwidth is determined by both the differential mode delay $\tau_f \sim 1/300\,\mathrm{MHz}$ and the propagation time through the long fibre $T \sim 1/8\,\mathrm{MHz}$. The bandwidth is thus only limited by the electrical response of the PI box.

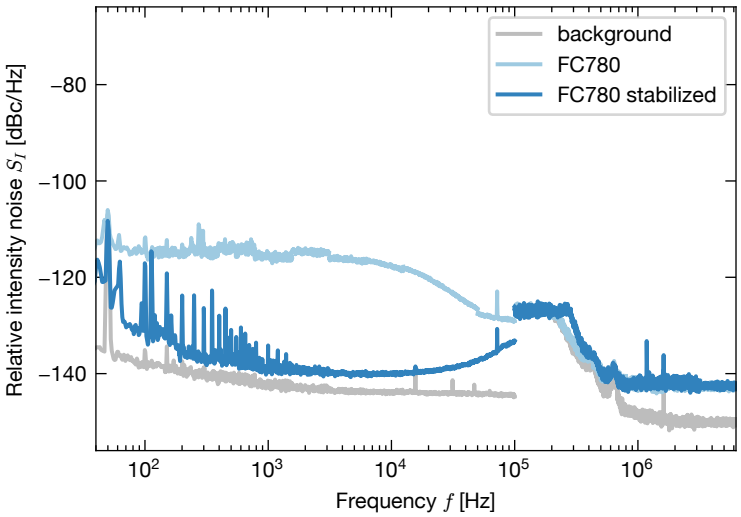

Figure 4.20: **Relative intensity noise after multimode fibre with stabilization.** The intensity fluctuations of a free-running and an AOM-controlled, PI stabilized femtosecond laser is compared. The low frequency noise floor is significantly reduced, apart from power line noise introduced by the AOM driver and the PI controller servo bump around 250 kHz. The background noise bump above 100 kHz results from changing the measurement device from a FFT to a RF spectrum analyser which has a high noise floor at low frequencies.

Fig. 4.20 shows that active stabilization significantly reduces the global intensity noise from the femtosecond laser. In order to measure a large spectral range, the large bandwidth (150 MHz) fixed gain silicon photodiode Thorlabs PDA10A-EC is used, which is independent of the slower feedback photodiode used for intensity stabilization. The increased noise of the stabilized light, peaked at 250 kHz, results from the finite stabilization bandwidth as the PI controller fails to follow faster fluctuations. Tuning the gain parameters allows for flattening of the bump, resulting in a reduced peak at the cost of a higher low frequency noise floor.

5 Conclusion

In this thesis three methods for the generation of spatially incoherent light for suppression of coherent noise in arbitrary optical dipole traps have been demonstrated.

In the first approach, an optical ground-glass diffuser was coherently illuminated and rotated, which produced an intensity-averaged speckle pattern. Second, the incidence angle of a coherent laser on a holographic diffuser was modulated by two orthogonal AODs, which resulted in a similar speckle-averaging effect. Third, a broadband light source was passed through a square-core step-index optical multimode fibre whose modal dispersion lead to dephasing and thus incoherence.

In an imaging scheme, the number of mutually incoherent modes M (2.20) of the generated light field determines how many independently illuminated image pixels can be obtained. For the diffuser approaches, this number could be well-controlled by tuning the incident beam size. In the particular data shown, the number of modes (defined with a cutoff at the FWHM) was given by $M_{\mathrm{rot}} \sim 84^2$ for the rotating diffuser and $M_{\mathrm{AOD}} \sim 48^2$ for the AOD approach. In the multimode fibre case, the core size of the multimode fibre determined the number of its mutually incoherent modes, yielding $M_{\mathrm{MFS}} \sim 43^2$. If larger numbers are required, a larger fibre core or a shorter wavelength can be used.

The residual coherences $|\gamma|$ determine the fraction of the remaining relative speckle noise and depend on the observing integration time $T \ll 1/f$ (3.5), where f is the fastest relevant transition frequency in the atomic system. For the diffusers these were measured to be $|\gamma_{\mathrm{rot}}| \sim 3.5\,\%$ at $T_{\mathrm{rot}} \sim 1/240\,\mathrm{Hz}$ and $|\gamma_{\mathrm{AOD}}| \sim 6\,\%$ at $T_{\mathrm{AOD}} \sim 1/50\,\mathrm{kHz}$. Using a femtosecond laser, the residual coherence of the multimode fibre could be suppressed to $|\gamma_{\mathrm{MFS}}| \sim 3\,\%$ where the integration time has to average out the pulses, thus $T \sim 1/250\,\mathrm{MHz}$. For tight traps, e.g. optical lattices, with atomic trapping frequencies in the kHz regime, the diffuser approaches are clearly too slow, whereas the short coherence times of the broadband sources make the fibre approach viable.

Since this thesis serves as a proof of concept, next steps include imaging and efficiency tests with parameters exactly reflecting an ultracold atoms experiment, as well as an actual implementation with higher powered light sources in the atomic system. Potential

improvements to the fibre approach can be achieved by specifically designing waveguides which maximize modal dispersion or scrambling the incoupled wavefront to achieve larger mode excitation diversity.

Bibliography

[1] Georgescu, I. M., Ashhab, S. & Nori, F. Quantum simulation. *Reviews of Modern Physics* **86**, 153–185 (2014).

[2] Feynman, R. P. Simulating physics with computers. *International Journal of Theoretical Physics* **21**, 467–488 (1982).

[3] Anderson, M. H., Ensher, J. R., Matthews, M. R., Wieman, C. E. & Cornell, E. A. Observation of bose-einstein condensation in a dilute atomic vapor. *Science (New York, N.Y.)* **269**, 198–201 (1995).

[4] Davis *et al.* Bose-einstein condensation in a gas of sodium atoms. *Physical review letters* **75**, 3969–3973 (1995).

[5] Bloch, I., Dalibard, J. & Zwerger, W. Many-body physics with ultracold gases. *Reviews of Modern Physics* **80**, 885–964 (2008).

[6] Gross, C. & Bloch, I. Quantum simulations with ultracold atoms in optical lattices. *Science (New York, N.Y.)* **357**, 995–1001 (2017).

[7] Greiner, M., Mandel, O., Esslinger, T., Hänsch, T. W. & Bloch, I. Quantum phase transition from a superfluid to a mott insulator in a gas of ultracold atoms. *Nature* **415**, 39 (2002).

[8] Polkovnikov, A., Sengupta, K., Silva, A. & Vengalattore, M. Colloquium : Nonequilibrium dynamics of closed interacting quantum systems. *Reviews of Modern Physics* **83**, 863–883 (2011).

[9] Goldman, N., Budich, J. C. & Zoller, P. Topological quantum matter with ultracold gases in optical lattices. *Nature Physics* **12**, 639–645 (2016).

[10] Chin, C., Grimm, R., Julienne, P. & Tiesinga, E. Feshbach resonances in ultracold gases. *Reviews of Modern Physics* **82**, 1225–1286 (2010).

[11] Yan, B. *et al.* Observation of dipolar spin-exchange interactions with lattice-confined polar molecules. *Nature* **501**, 521 (2013).

[12] Schauß, P. *et al.* Observation of spatially ordered structures in a two-dimensional rydberg gas. *Nature* **491**, 87 (2012).

[13] Bakr, W. S., Gillen, J. I., Peng, A., Fölling, S. & Greiner, M. A quantum gas microscope for detecting single atoms in a hubbard-regime optical lattice. *Nature* **462**, 74 (2009).

[14] Sherson, J. F. *et al.* Single-atom-resolved fluorescence imaging of an atomic mott insulator. *Nature* **467**, 68 (2010).

[15] Parsons, M. F. *et al.* Site-resolved imaging of fermionic ˆ6li in an optical lattice. *Physical review letters* **114**, 213002 (2015).

[16] Haller, E. *et al.* Single-atom imaging of fermions in a quantum-gas microscope. *Nature Physics* **11**, 738 (2015).

[17] Cheuk, L. W. *et al.* Quantum-gas microscope for fermionic atoms. *Physical review letters* **114**, 193001 (2015).

[18] Omran, A. *et al.* Microscopic observation of pauli blocking in degenerate fermionic lattice gases. *Physical review letters* **115**, 263001 (2015).

[19] Weitenberg, C. *et al.* Single-spin addressing in an atomic mott insulator. *Nature* **471**, 319–324 (2011).

[20] Fukuhara, T. *et al.* Quantum dynamics of a mobile spin impurity. *Nature Physics* **9**, 235–241 (2013).

[21] Fukuhara, T. *et al.* Microscopic observation of magnon bound states and their dynamics. *Nature* **502**, 76 (2013).

[22] Choi, J.-y. *et al.* Exploring the many-body localization transition in two dimensions. *Science (New York, N.Y.)* **352**, 1547–1552 (2016).

[23] Kaufman, A. M. *et al.* Quantum thermalization through entanglement in an isolated many-body system. *Science (New York, N.Y.)* **353**, 794–800 (2016).

[24] Labuhn, H. *et al.* Tunable two-dimensional arrays of single rydberg atoms for realizing quantum ising models. *Nature* **534**, 667 (2016).

[25] Barredo, D., Lienhard, V., Léséleuc, S. d., Lahaye, T. & Browaeys, A. Synthetic three-dimensional atomic structures assembled atom by atom. *Nature* **561**, 79 (2018).

[26] Rigden, J. D. & Gordon, E. I. Granularity of scattered optical maser light. *Proceedings of the Institute of Radio Engineers* **50**, 2367 (1962).

[27] Bakr, W. S. *et al.* Probing the superfluid-to-mott insulator transition at the single-atom level. *Science (New York, N.Y.)* **329**, 547–550 (2010).

[28] Billy, J. *et al.* Direct observation of anderson localization of matter waves in a controlled disorder. *Nature* **453**, 891 (2008).

[29] Bloch, I. Ultracold quantum gases in optical lattices. *Nature Physics* **1**, 23 (2005).

[30] Ma, R. *Engineered potentials and dynamics of ultracold quantum gases under the microscope: Dissertation* (2014).

[31] Riechert, F. *Speckle Reduction in Projection Systems: Dissertation* (Universitätsverlag Karlsruhe, Karlsruhe, 2009).

[32] Bianco, V. *et al.* Strategies for reducing speckle noise in digital holography. *Light: Science & Applications* **7**, 48 (2018).

[33] Schmitt, J. M., Xiang, S. H. & Yung, K. M. Speckle in optical coherence tomography. *Journal of biomedical optics* **4**, 95–105 (1999).

[34] Burckhardt, C. B. Speckle in ultrasound b-mode scans. *IEEE Transactions on Sonics and Ultrasonics* **25**, 1–6 (1978).

[35] Lee, J.-S. Speckle analysis and smoothing of synthetic aperture radar images. *Computer Graphics and Image Processing* **17**, 24–32 (1981).

[36] Iwai, T. & Asakura, T. Speckle reduction in coherent information processing. *Proceedings of the IEEE* **84**, 765–781 (1996).

[37] Stangner, T., Zhang, H., Dahlberg, T., Wiklund, K. & Andersson, M. Step-by-step guide to reduce spatial coherence of laser light using a rotating ground glass diffuser. *Applied optics* **56**, 5427–5435 (2017).

[38] Kubota, S. & Goodman, J. W. Very efficient speckle contrast reduction realized by moving diffuser device. *Applied optics* **49**, 4385–4391 (2010).

[39] Farrokhi, H. *et al.* High-brightness laser imaging with tunable speckle reduction enabled by electroactive micro-optic diffusers. *Scientific reports* **7**, 15318 (2017).

[40] Trisnadi, J. I. Hadamard speckle contrast reduction. *Optics Letters* **29**, 11 (2004).

[41] Trisnadi, J. I. Speckle contrast reduction in laser projection displays. *Projection Displays VIII* 131–138 (2002).

[42] Akram, M. N., Tong, Z., Ouyang, G., Chen, X. & Kartashov, V. Laser speckle reduction due to spatial and angular diversity introduced by fast scanning micromirror. *Applied optics* **49**, 3297–3304 (2010).

[43] Epworth, R. E. (ed.). *The phenomenon of modal noise in analogue and digital optical fibre systems* (1978).

[44] Mehta, D. S., Naik, D. N., Singh, R. K. & Takeda, M. Laser speckle reduction by multimode optical fiber bundle with combined temporal, spatial, and angular diversity. *Applied optics* **51**, 1894–1904 (2012).

[45] Donini, L. *A Spatially Incoherent Laser Source* (2018).

[46] Lehmberg, R. H., Schmitt, A. J. & Bodner, S. E. Theory of induced spatial incoherence. *Journal of Applied Physics* **62**, 2680–2701 (1987).

[47] Karpol, A., Reinhorn, S., Elysaf, E., Yalov, S. & Kenan, B. Method and apparatus for article inspection including speckle reduction (2005).

[48] Nakano, H. *et al.* Partially coherent light generated by using single and multimode optical fibers in a high–power nd:glass laser system. *Applied Physics Letters* **63**, 580–582 (1993).

[49] Redding, B. *et al.* Low spatial coherence electrically pumped semiconductor laser for speckle-free full-field imaging. *Proceedings of the National Academy of Sciences of the United States of America* **112**, 1304–1309 (2015).

[50] Cao, H., Chriki, R., Bittner, S., Friesem, A. A. & Davidson, N. Complex lasers with controllable coherence. *Nature Reviews Physics* **1**, 156–168 (2019).

[51] Redding, B., Bromberg, Y., Choma, M. A. & Cao, H. Full-field interferometric confocal microscopy using a vcsel array. *Optics letters* **39**, 4446–4449 (2014).

[52] Chriki, R. *et al.* Manipulating the spatial coherence of a laser source. *Optics express* **23**, 12989–12997 (2015).

[53] Redding, B., Choma, M. A. & Cao, H. Speckle-free laser imaging using random laser illumination. *Nature photonics* **6**, 355–359 (2012).

[54] Goodman, J. W. *Introduction to fourier optics* (W.H. Freeman Macmillan learning, New York, 2017), 4th edn.

[55] Mandel, L. & Wolf, E. *Optical coherence and quantum optics* (2008), reprint. with corr edn.

[56] Cohen, L. Generalization of the wiener-khinchin theorem. *IEEE Signal Processing Letters* **5**, 292–294 (1998).

[57] Friberg, A. T. & Turunen, J. Imaging of gaussian schell-model sources. *Journal of the Optical Society of America A* **5**, 713 (1988).

[58] Goodman, J. W. *Speckle phenomena in optics: theory and applications* (Roberts and Company Publishers, 2007).

[59] Zardecki, A., Delisle, C. & Bures, J. Generalized notion of the coherence area. *Optics Communications* **5**, 298–300 (1972).

[60] Upatnieks, J. & Lewis, R. W. Noise suppression in coherent imaging. *Applied optics* **12**, 2161–2166 (1973).

[61] Grimm, R., Weidemüller, M. & Ovchinnikov, Y. B. Optical dipole traps for neutral atoms. In Bederson, B. & Walther, H. (eds.) *Advances in Atomic, Molecular, and Optical Physics*, vol. 42 of *Advances In Atomic, Molecular, and Optical Physics*, 95–170 (Elsevier textbooks, s.l., 1999).

[62] Steck, D. A. *Quantum and Atomic Optics* (2018), 0.12.3 edn.

[63] Savard, T. A., O'Hara, K. M. & Thomas, J. E. Laser-noise-induced heating in far-off resonance optical traps. *Physical Review A* **56**, R1095–R1098 (1997).

[64] Jaksch, D., Bruder, C., Cirac, J. I., Gardiner, C. W. & Zoller, P. Cold bosonic atoms in optical lattices. *Physical Review Letters* **81**, 3108–3111 (1998).

[65] Reed, I. On a moment theorem for complex gaussian processes. *IEEE Transactions on Information Theory* **8**, 194–195 (1962).

[66] Takai, N. Statistics of dynamic speckles produced by a moving diffuser under the gaussian beam laser illumination. *Japanese Journal of Applied Physics* **13**, 2025 (1974).

[67] Saleh, B. E. A. & Teich, M. C. *Fundamentals of Photonics*. Wiley Series in Pure and Applied Optics (John Wiley & Sons, Chicester, 2013), 2nd edn.

[68] Chang, I. C. I. acoustooptic devices and applications. *IEEE Transactions on Sonics and Ultrasonics* **23**, 2–21 (1976).

[69] Analog Devices. A technical tutorial on digital signal synthesis. *Analog Devices Application Note* 1–122 (1999).

[70] Hlubina, P. Spatial and temporal coherence of light in a fibre waveguide. *Journal of modern optics* **40**, 1893–1907 (1993).

[71] Jensen, J. L. W. V. Sur les fonctions convexes et les inégalités entre les valeurs moyennes. *Acta Mathematica* **30**, 175–193 (1906).

[72] Pask, C. & Snyder, A. W. The van cittert-zernike theorem for optical fibres. *Optics Communications* **9**, 95–97 (1973).

[73] Efimov, A. Spatial coherence at the output of multimode optical fibers. *Optics express* **22**, 15577–15588 (2014).

[74] Rossetti, M. *et al.* Superluminescent light emitting diodes: the best out of two worlds. In Schenk, H., Piyawattanametha, W. & Noell, W. (eds.) *MOEMS and Miniaturized Systems XI*, SPIE Proceedings, 825208 (SPIE, 2012).

[75] Haus, H. A. Mode-locking of lasers. *IEEE Journal of Selected Topics in Quantum Electronics* **6**, 1173–1185 (2000).

[76] Doran, N. J. & Wood, D. Nonlinear-optical loop mirror. *Optics Letters* **13**, 56 (1988).

[77] Gloge, D. & Marcatili, E. A. J. Multimode theory of graded-core fibers. *Bell System Technical Journal* **52**, 1563–1578 (1973).

[78] Efimov, A. Lateral-shearing, delay-dithering mach-zehnder interferometer for spatial coherence measurement. *Optics letters* **38**, 4522–4525 (2013).

[79] Gross, R. & Marx, A. *Festkörperphysik*. De Gruyter Studium (De Gruyter, Berlin and Boston, 2018), 3rd edn.

[80] Mears, R. J., Reekie, L., Im Jauncey & Payne, D. N. Low-noise erbium-doped fibre amplifier operating at 1.54 μm. *Electronics Letters* **23**, 1026–1028 (1987).

[81] Stolen, R. H. & Lin, C. Self-phase-modulation in silica optical fibers. *Physical Review A* **17**, 1448–1453 (1978).

[82] Walmsley, I., Waxer, L. & Dorrer, C. The role of dispersion in ultrafast optics. *Review of Scientific Instruments* **72**, 1–29 (2001).

[83] Szipöcs, R., Spielmann, C., Krausz, F. & Ferencz, K. Chirped multilayer coatings for broadband dispersion control in femtosecond lasers. *Optics Letters* **19**, 201 (1994).

[84] Shin, S., Sharma, U., Tu, H., Jung, W. & Boppart, S. A. Characterization and analysis of relative intensity noise in broadband optical sources for optical coherence tomography. *IEEE photonics technology letters : a publication of the IEEE Laser and Electro-optics Society* **22**, 1057–1059 (2010).

[85] Blazek, M., Hartmann, S., Molitor, A. & Elsaesser, W. Unifying intensity noise and second-order coherence properties of amplified spontaneous emission sources. *Optics letters* **36**, 3455–3457 (2011).

[86] Hodara, H. Statistics of thermal and laser radiation. *Proceedings of the IEEE* **53**, 696–704 (1965).

[87] Ho, P.-T. Phase and amplitude fluctuations in a mode-locked laser. *IEEE Journal of Quantum Electronics* **21**, 1806–1813 (1985).

Abbreviations

1D one-dimensional. 12, 41
2D two-dimensional. 20, 35, 44
3D three-dimensional. 35

ADC analogue-digital converter. 66
AM amplitude modulation. 32, 33
AOD acousto-optic deflector. 2, 32, 33, 35, 41, 43–45, 83
AOM acousto-optic modulator. 33, 61, 62, 81
ASE amplified spontaneous emission. 3, 57, 58, 67

CCD charge-coupled device. 33, 63, 64
CEO carrier-envelope offset. 58
CLT central limit theorem. 24, 26

DDS direct digital synthesis. 32, 33
DG ground-glass diffuser. 31
DG220 Thorlabs N-BK7 220 grit. 31, 36, 37, 39
DG600 Thorlabs N-BK7 600 grit. 36
DH holographic diffuser. 31
DH15 Edmund Optics 15° FWHM divergence. 32, 36, 42–44
DH80 Edmund Optics 80° FWHM divergence. 32, 37, 38, 42, 43

ECDL external cavity diode laser. 31, 59, 80

FC frequency comb. 67, 69, 79, 80
FC780 780 nm Menlo M-Comb/M-VIS. 59, 67–70, 72, 73, 79, 80
FFT fast Fourier transform. 61, 80, 81
FM frequency modulation. 32, 33, 43, 44

FWHM full width at half maximum. 11, 12, 29, 31, 36–38, 42, 45, 71, 83

LD laser diode. 67, 69
LD780 Eagleyard EYP-RWE-0780. 59, 67, 70, 72–75, 78
LED light-emitting diode. 40, 41
LP linear polarized. 53–55, 97

MEMS micro-electro-mechanical systems. 41
MFG graded-index multimode fibre. 71
MFG5 Thorlabs GIF625. 60, 70, 74
MFR round-core step-index multimode fibre. 56, 71, 73, 77, 78
MFR20 Thorlabs FG105LCA. 60, 70, 76
MFR5 Thorlabs FG105LCA. 60
MFS square-core step-index multimode fibre. 56, 71–73, 77, 78
MFS25 Thorlabs FP150QMT. 60, 70, 72, 73, 76, 80
MFS5 Thorlabs FP150QMT. 60

NA numerical aperture. 13, 14, 45, 52, 56, 72, 74
NBL narrowband laser. 67, 79, 80
NBL420 420 nm Toptica TA-SHG. 32
NBL780 780 nm Toptica DL pro. 31, 59, 64, 67, 79

PI proportional-integral. 61, 62, 80–82

RF radio frequency. 33, 35, 61, 62, 81
RIN relative intensity noise. 10, 40, 58, 78–80
RMS root mean square. 25

SLD superluminescent diode. 58, 67, 69, 79, 80
SLD670 Superlum SLD-261. 59, 67, 69, 70, 72–74, 79, 80
SMF single-mode fibre. 60, 70, 71, 74
SPM self-phase modulation. 68

VCO voltage-controlled oscillator. 61

VCSEL vertical-cavity surface-emitting laser. 3

w.l.o.g. without loss of generality. 14

List of Figures

Acknowledgements

First of all, I would like to thank my supervisor Christian Groß for the possibility to work on this interesting project. His advice and support were of major importance for the realization of the thesis.

I would also like to thank Immanuel Bloch for formally supervising the thesis and providing me the opportunity to join his group.

Furthermore, I am grateful to Michael Knap for again supervising my thesis and giving great lectures which left a lasting impression.

I am particularly thankful to Antonio Rubio Abadal for always helping me with any issues, regardless of physical, organizational or presentational origin. I am also fortunate to have had help by Simon Hollerith, especially when solving problems in the laboratory.

Additionally, I would like to express my appreciation to Johannes Zeiher for the discussions and feedback advancing the project. I am also thankful to Jun Rui for sharing his knowledge on cold atoms with me.

For realizing the technical aspects of the project, I would also like to thank Anton Mayer, Olivia Mödl and Karsten Förster.

Finally, I am deeply grateful to my parents for constantly supporting me, especially during my studies.